UNIVERSITÀ
DEGLI STUDI
FIRENZE

INTERNATIONAL DOCTORATE IN ATOMIC AND MOLECULAR PHOTONICS

CICLO XXXI

COORDINATORE Prof. Francesco Saverio Cataliotti

Single nitrogen-vacancy centers in diamond for spin quantum control

Settore Scientifico Disciplinare Fis / 03 Fisica della materia

Tutore
Dott.ssa Nicole Fabbri

Dottorando
Dott. Francesco Poggiali

Co-tutore
Prof.ssa Paola Cappellaro

Coordinatore
Prof. Francesco Saverio Cataliotti

Anni 2015 / 2018

Single nitrogen-vacancy centers in diamond for spin quantum control

by

Francesco Poggiali

Submitted to the European Laboratory for Non-linear Spectroscopy
on October, 2018, in partial fulfillment of the requirements
for the degree of Doctor of Philosophy in
International Doctorate in Atomic and Molecular Photonics

Abstract

The properties of quantum mechanics promise to overcome the limitations of classical physics in novel quantum technologies. The potential of important applications such as quantum computations and quantum sensing motivates and provides a context to the present dissertation.

The thesis focuses on one of the most promising experimental platforms: Single nitrogen-vacancy (NV) centers in diamond. This quantum system is composed by the spins of the valence electrons of the crystalline point defects and their nearby nuclei. Quite generally, a fundamental requirement to exploit the potentialities of the quantum nature of a system is its precise control. However, this always involves new challenges, related to the need to protect the quantum system from the environment (i.e. preserving the quantum nature of the system itself) and the desire to develop measurement protocols that can enhance its performance for quantum applications. Therefore, I focused my Ph.D. work to find novel solutions to these challenges.

The dissertation, developed in the context of a research project taking place at University of Florence-European Laboratory for Non-linear Spectroscopy (UNIFI-LENS), is focused on two complementary goals: an improved characterization and control of the NV center and its environment, which enables superior performance in quantum sensing, and novel sensing methods with NV centers, that can be applied to better characterize the environment itself.

As a first project, we addressed the manipulation and control of the spin associated with a nearby nucleus. In particular, we explored the dynamic nuclear polarization mechanism of the ^{14}N nucleus intrinsic to the NV defect itself, to produce a high-polarized nuclear spin state. The dynamics of this phenomenon depends strongly on the interaction between electronic and nuclear NV spins in the orbital excited state. Characterizing the process as a function of alignment and strength of an external magnetic field, we obtained

the first precise direct evaluation of the transverse hyperfine coupling in the excited-state of the NV center.

Then, we devised and implemented an optimal control method for magnetic field quantum sensing. The purpose was the measurement of weak variable fields via dynamical decoupling techniques with the NV electronic spin. Our technique is distinct from previous ones for the introduction in our numerical optimization of an innovative metric: The sensor sensitivity. Using this metric enables finding the best compromise between decoupling the NV spin from the environment and enhancing the effects of the target field. We tested our algorithm on different exemplary scenarios and verified it for some experimental cases. In all the considered cases, our method leads to an improvement of the sensitivity up to a factor of 2 with respect to traditional dynamical decoupling techniques. Moreover, our optimized sequences can guarantee a speed up of the sensing measurement without a deterioration of the sensitivity. This would be fundamental for the measurement of weak fields characterized by a short lifetime.

The knowledge of the environment is a prerequisite for preserving the NV spin from decoherence and enabling optimal control techniques. Therefore, the last part of the dissertation is dedicated to the study of the properties of the NV-environment interactions considering both the ^{13}C nuclear spin bath inside the diamond and the effects of strongly interacting nearby nuclei. We implemented a method that allows us to spectrally characterize such environment, valid even in the case of relatively short coherence times. For a weak coupling regime, i.e. high bias magnetic field, we verified the robustness of the model under control sequences different from the ones used to extract the environment characteristics. We found a considerable agreement between data and numerical simulations for the NV electronic spin evolution, without any fit parameter.

The suite of methods and results obtained in this thesis can be used to improve the performance of NV-based quantum sensors, that are finding widespread applications in fields ranging from biosensing, to geoscience, condensed matter physics and precision metrology. More broadly, while all the methods presented in this thesis are designed for applications with single NV centers in diamond, they are quite general. It would then be possible to apply them to different quantum experimental platform, such as defects in silicon carbide, ultracold atoms or trapped ions, and achieve similar improvement in other quantum devices.

Contents

List of Figures

Introduction

Nowadays, one of the most relevant research fields involves the study and development of quantum systems for practical applications (so-called quantum technologies). For example, the implementations of efficient computation (quantum computation) [1] and high-precision measurements (quantum metrology) [2] are important purposes both from the theoretical and experimental point of views. The basis of the reached progress are related to the peculiar properties associated to quantum mechanics, such as superposition principle and entanglement, that enable the possibility to overcome the limitations of classical physics [3, 4].

However, to really exploit these possibilities, the precise control of the quantum system is an indispensable requirement. "Control" means the capability to manipulate the system avoiding the drop of its quantum properties: To do it, a full knowledge of the system is in general necessary. This is also true since any realistic quantum platform is inevitably coupled to its (often classical) environment. Indeed, the coherent superposition of the system can be irrevocably destroyed (decoherence) due to the interaction with its surroundings. Reducing decoherence is one of the central problems in quantum control and it is the prominent argument of a wide research activity. Indeed, since addressing these arguments is the general purpose of my dissertation, the goal of this first part is to provide a brief introduction with the fundamental definitions and the concepts of both quantum computation and quantum sensing. Those two research fields have many characteristics in common and are the basis for the applications with nitrogen-vacancy (NV) centers in diamond, main subject of this thesis.

Principles of quantum computing

The necessary and sufficient requirements for any physical platform able to realize the universal quantum computing are univocally identified thanks to the Di Vincenzo criteria [5], that I report here. A quantum computer shall have the following characteristics:

I A scalable physical system with well-characterized qubits.

II The ability to initialize the state of the qubits to a simple fiducial state.

III Long decoherence times, much longer than the gate operation time

IV A universal set of quantum gates

V The capability to measure the state of specific qubits

The first criterium involves the definition of a qubit as a two level system (typically indicated with $|0\rangle$ and $|1\rangle$) encoding a bit of quantum information. The statement "well characterized" concerns several characteristics; first of all, its physical parameters should be completely known, including the internal Hamiltonian, as well as the coupling with additional levels of the qubit system. Then, a deep understanding of the interaction with its environment, e.g. other qubits, and couplings with external fields is necessary. About the scalability, it is not uniquely defined for all the possible different applications, but in general represents the capability of the system to improve its performances, proportionally to the size of the system (e.g. increasing the number of qubits). The II criterion is not simply related to the straightforward requirement to have a well known starting point for the quantum computation process, but also to the possibility to resort to this fiducial state for quantum error correction, improving the qubit performances. For the satisfaction of the third criterion, we can describe the decoherence as the loss of the quantum information stored by the qubit, i.e. the drop of the off-diagonal elements of the density matrix ρ or the presence of loss channels due to states of the qubit different from $|0\rangle$ and $|1\rangle$; if the decoherence dynamics is much slower of the capability to manipulate the qubit, it enables the implementation of multiple quantum gate operations with high fidelity of operation. To be considered "universal", as required from the IV point, a set of quantum gates has to include both one-qubit gates and two-qubits (e.g., controlled-NOT, cNOT) gates; the latter point can be considered the core of the entanglement creation between qubits. The final requirement points out that the result of the computation sequence must be read out; this is possible once each specific qubit can be measured independently.

In the last two decades an important part of modern physics concerns the development of physical systems for quantum computation, and there is a number of candidates [6] that could represent a feasible platform; we can easily recognize as potential qubits photons, trapped ions or neutral atoms, superconducting circuits, electrons in quantum dots and donors or defects in solid state systems. However, it remains unclear which technology, if any, will ultimately prove successful.

Quantum sensing requirements

The definition of "quantum sensing" can be expressed as the use of a quantum object to measure a physical, classical or quantum, quantity. One of the main properties of the quantum object is given by the presence of quantized energy levels, depending on the physical quantity that we aim to measure. Another possibility is related to the use of quantum coherence, as for temporal superposition state, to perform the measurement of the target field to be measured or, otherwise, the improvement of the sensitivity of a measurement, beyond the classical limit, with the aid of entanglement.

An extended discussion about quantum sensing can be found in [7], from which we also derive some specific characteristics for the definition of a quantum sensor. In analogy to the Di Vincenzo criteria for quantum computation, a quantum sensor should have first of all discrete, resolvable energy levels related to a two-level system; obviously, an ensemble of two-level systems would exhibit many advantages as well. On the other hand, in this case the scalability requirement, belonging to the first Di Vincenzo criterion, does not play the same crucial role as for quantum computation. The presence of a fiducial state easily to be initialized is still an essential feature for a quantum sensing protocol. Then, we need the possibility to coherently manipulate the qubits, even if the possibility to entangle two of them, that is, a two-qubit gate required for a universal set of gates, is not necessary. Nevertheless, it would be an important feature for the quantum sensing platform. Of course, the ability to read out the state of the system remains at the basis also for a sensing measurement.

Up to now, the depicted characteristics of a quantum sensor are in common with the qubit for a quantum computer; another specific requirement for quantum sensing applications is the capability to interact with a relevant physical quantity that is the target of the measurement (e.g. an electric or magnetic field). This interaction can be described by a coupling parameter able to relate the changes in the external target with the ones in the transition energy of the quantum sensor. So, the two main characteristics to discriminate different quantum sensors are: *i)* "to what" and *ii)* "how much" they are sensitive. Meanwhile the first, of course, defines for which possible application you can use a given sensor, the second is one of the most prominent features to determine the quality of the sensor itself and it is represented by the "intrinsic sensitivity". Indeed, the optimum sensor should provide the strongest response to the target signal, meanwhile minimizing the effects of unwanted perturbations. Obviously, these are in general two conflicting tasks that have to be reconciled. Therefore, even if we did not consider the III Di Vincenzo criterion, concerning the ratio between coherence

and operation time on the qubit, in the definition of a quantum sensor, it affects in a fundamental (still not exclusive) way the goodness of the sensing measurement.

We can identify a number of experimental candidates that can take on charge the quantum sensing task. A review of all possible quantum sensors goes beyond the purposes of this thesis and can be found in [7]. Here, we limit ourselves to mention the most prominent for the group related to magnetic field sensing, as it is the case of NV centers: The categories are basically the ones mentioned for the quantum computing case, ranging from vapor cells or cold clouds for neutral atoms [8, 9], to solid-state spins, like NMR sensors [10], and superconducting circuits, as superconducting quantum interference devices (SQUID, [11]) and flux qubits [12]. There is in this case also the addition of some elementary particles (muons [13]) and optomechanical systems [14].

In general, the sensing sequence can be described by a basic measurement protocol, the starting point of which consists, as discussed, in the preparation of the sensing state: It could also be not simply one of the two states of the qubit basis, but also any superposition state useful to sense the target. Then, the sensor evolves under an Hamiltonian, composed by the internal time-independent one, characterized by $|0\rangle$ and $|1\rangle$ as the eigenstates, the interaction with the target and the external control. At the end of the sensing procedure, the system is in a final sensing state; if necessary, the read out basis could be different from the initial one, and made by a combination of $|1\rangle$ and $|0\rangle$. Finally, the state of the sensor is read out with a measurement, typically a projective one [1]. Indicating with 1 (0) the eigenvalue associated to $|1\rangle$ ($|0\rangle$), the measurement would give a binary outcome of a physical quantity measurable with the experimental apparatus: Either 1 with probability x (proportional to the probability p for the qubit to change its state during the measurement) or 0 with probability $1-x$. Therefore, to obtain a precise evaluation of p, a repetition of the whole sequence has to be performed, by averaging over many realizations on the same qubit or averaging over many qubits. Although the described protocol is not universal, it can be used to describe most of the quantum sensing techniques.

Dissertation contest

In the depicted scenario for quantum sensing and computing, one of the most promising opportunities to transfer quantum mechanical properties in

[1] A projective measurement is described by a Hermitian operator on the state space of the system being observed [15].

everyday applications is represented by nitrogen-vacancy centers in diamond, subject of this thesis work. In this case, the quantum system is represented by the intrinsic angular momentum of the valence electrons of the crystalline point defects and their nearby nuclei. The ability to coherently control with very-high precision these degrees of freedom makes NV centers ideal candidates for a wide class of quantum applications,e.g. for magnetic field quantum sensing [16, 17], and for quantum computing applications [6].

About the latter, NVs have been demonstrated a good platform for the creation of quantum registers [18] and coherent feedback control of the qubit with the aid of an ancilla system [19]. They are also a suitable system to create entanglement, both between different nuclear spins by means of a single NV center [20] and between different NVs [21]. On the other hand, they are very flexible for magnetic field sensing, enabling measurements of weak variable magnetic fields with nanometric resolution [22, 23]. Therefore, it is possible to exploit these characteristics for devices that can scan different samples [24] or directly measure fields generated by molecules on the diamond surface in very small volumes [25]. Moreover, the biocompatibility of the diamond leads to important applications for biological purposes, like measurements of action potentials generated by neuron cells [26, 27].

Nevertheless, there are still some open challenges in order to push the performances of the NV quantum system to their ultimate limits: *i)* new measurement protocols, *ii)* protection from the environment and *iii)* quantum error correction are indispensable tools in this sense. This dissertation is therefore focused on addressing these points, with particular attention for *i)* and *ii)* by means the development and experimental realization of novel techniques for the quantum control of single NV centers. This Ph.D work has been realized as a part of an experiment running at University of Florence-European Laboratory for Non-Linear Spectroscopy (UNIFI-LENS).

The thesis is structured as following: A first part of Cap. 1 provides an introduction to NV centers, describing their physical properties. Then, after a short description of our experimental setup, I describe the measurement methods used to control the NV spin system. Chapter 2 discusses how to manipulate and control a second quantum degree of freedom: The spin associated to a nearby nucleus. In particular, we studied the possibility to polarize the nuclear spin associated to the NV color center by means of dynamic nuclear polarization mechanism. Studying the dynamics of this process, we provided a first precise experimental evaluation of the transverse hyperfine coupling between the nuclear spin of a ^{14}N, composing the NV defect itself, and the NV electron one in the orbital excited state. In Ch. 3 I present an innovative method for the numerical optimization of amplitude measurements of ultraweak variable magnetic fields with arbitrary (known) frequency spec-

trum. The novelty of the idea lies on the use of a new optimization metric, chosen instead of the usual fidelity of operation: The sensitivity itself. We characterized the method for various exemplary cases of magnetic fields and we also demonstrated a good agreement with experimental measurements performed on a single NV center in bulk diamond. Since the basic idea is general, this approach would be relevant also for different platforms to push sensitivity towards its limit. Chapter 4 addresses the problem of the knowledge of the environment surrounding a quantum system. In particular, we studied both the properties of the diamond nuclear spin bath and the effects of strongly interacting nearby nuclei. In the Conclusions, I summarize the main results obtained with my work and the challenges and perspectives to extend it.

Chapter 1

Nitrogen-vacancy platform: Background and applications

Negatively charged nitrogen-vacancy centers in diamond have emerged as promising platforms for quantum information processing and for a wide range of applications in quantum sensing. The NV electronic spin remarkable properties, such as optical initialization and readout of its spin state [28], and extremely long spin coherence [29], make it an excellent candidate for quantum technologies.

In this chapter I introduce what NVs are and their main properties, providing the knowledge tools that are needed to make familiar with the physics related to this quantum system. First, in Sec. 1.1, I present the physical structure of NV centers providing also a brief overview of the most used methods to create them inside the diamond structure. Second, in Sec. 1.2 and 1.3, I describe the NV quantum spin system and its relevant energy structure, that make NV centers reliable for a wide range of studies and applications. I introduce also the description of the interaction between the NV center and the local environment, made by neighboring ^{13}C nuclei.

Then, in Sec. 1.4 I discuss the setup, already present at the European Laboratory for Non-linear Spectroscopy (LENS) at the beginning of my Ph.D. course, used to carry on the experimental work concerning this dissertation. Finally I present the standard techniques for detecting and manipulating the NV spin state, starting in Sec. 1.5 with Electron Spin Resonance experiments, and proceeding in Sec. 1.6 introducing the methods used to decouple the NV center from its environment.

1.1 NV structure and production

There are more than 500 luminescent defects in diamond [1] and a significant fraction has been and it is also nowadays subject of research activities [30]. Nitrogen is the prominent impurity inside the crystal lattice and some defects related to this element show many important properties for a wide range of applications.

In this work I address specifically the topic related to nitrogen-vacancy centers, that is, stable point defects of the diamond lattice structure; they consist in a substitutional nitrogen that replaces a carbon atom in the diamond lattice with a vacancy center as a first neighbor. The center is characterized by C_{3v} symmetry and appears in one of three possible different charge states: Positive NV^+ [31], neutral NV^0 [32] or negative NV^- [33,34]. Even if NV^+ and NV^0 are subject of important research studies [35,36], our interest for this dissertation will be focused on the negatively charged variation, as it involves all the properties described in the previous section. For this reason, from now on in the remainder of the text with NV notation I will imply the negatively charged one, dropping the charge superscript.

For the production of diamond samples and the creation of NV defects, different techniques can be exploited. Even if the study related to the fabrication of samples is a critical point to determine also the possibilities for applications, it goes beyond the aim of this thesis and here I will give just a brief overview of the different methods; an extension of this discussion could be found in [37]. The main technique to grow the diamond itself consist in Chemical Vapor Deposition (CVD) synthesis, with which carbon atoms are deposited onto a substrate inside a growth chamber with controlled atmosphere. CVD allows us the possibility to use different substrates materials and to obtain diamonds with very wide surfaces (over 10 cm of diameter and 1 mm of thickness [38]); it enables also the possibility to control the density of chemical impurities and so engineering the properties of the diamond itself. Indeed, only a small fraction of the substitutional nitrogen introduced during the grow process forms NV centers [39], typically $< 0.5\%$.

It is possible to enhance the N-to-NV conversion through an additional irradiation with electrons on the sample and an annealing process; the first enhance the number of vacancies present inside the crystal. With the second, heating the sample at temperatures in the range $600 - 2000$ °C, it is possible for the vacancies to diffuse towards substitutional nitrogen defects and form

[1] A prefect diamond is a semiconductor with a wide band gap of 5.5 eV (225 nm, UV), so transparent in a wide range of frequencies. Therefore, it is common that a defect hosted inside the lattice presents an energy structure that allows deep radiative transitions within the diamond bandgap.

NV^0 centers. Usually the additional electron necessary to obtain the negatively charged species could be provided by a neighbor single nitrogen inside the lattice. In this way the relative abundance of NV centers with respect to nitrogen impurities could reach values close to 50 %, that would be the most favorable case.

In order to highly reduce the dispersion of the defects inside the diamond it is possible to exploit the δ-doping technique: An interruption of the grow of the matrix material during the CVD enables the deposition of dopant impurities, in this case nitrogen, on the exposed surface of a high-purity sample [40]. At this point, an annealing process could be performed; in this way, once restarted the growth, NVs are confined to the plane where nitrogen was deposited, resulting in a doping with a δ-function-like profile, reducing both the depth at which NVs are and confining them in a specific layer, up to ~ 2 nm and ~ 5 nm of thickness and depth, respectively [41].

A further important method to insert NVs in the lattice close to the surface is ion implantation of nitrogen, mainly N^+ and N^{++}, into high-purity diamonds. The energy of the ion atoms as well as the ion flux and the beam shape are fundamental parameters to engineer the efficiency of the method [42–44]. This technique enables the production of samples with a regular pattern of NV defects maintaining a very low abundance of nitrogen. The spacing within the horizontal pattern and the implantation precision could be enhanced up to some tens of nm and $\sim$ 10 nm, respectively, by masking off the diamond surface or focusing the ion beam. The main drawbacks related to implantation are the lower photo-stability and shorter spin coherence times with respect to NVs created with different techniques [45].

1.2 NV as quantum system

Once analysed the structural properties, now I address the description of the physical system that make NV centers reliable for a wide range of studies and applications. First of all, it is possible to describe the electron system of the diamond crystal as the sum of covalent-type interactions between the valence electrons of two nearest neighbor atoms [46]. Obviously the presence of a vacancy, i.e. the absence of an ion, breaks the bonds in the crystal, producing unpaired electrons that contribute to the properties of the center. In the case of our interest, the three carbon atoms contribute to NV valence band with one electron and the nitronen composing the NV itself gives in turn two electrons, behaving as a donor [32, 47]. This description would correspond to the neutral NV^0 configuration, to which it is possible to add a last additional electron exploiting the presence of a second nitrogen close

to the defect [48].

In this configuration, the description of the orbital wavefunctions representation of the six electrons it is totally equivalent to the one made by two holes (with the caveat to consider the different sign of the interactions); it is therefore convenient to choose the representation containing the smallest number of particles. The resulting spin system associated with the NV center consists in an electronic spin $S = 1$, generating an energy structure similar to a "two-electrons atom" case, ideally separated in triplet and singlet sates.

For an in depth discussion related to the energy levels and their symmetries it is possible to refer to [46]. The symmetry axis of the defect, the $[1, 1, 1]$ of the crystal, defines the favored direction of the spin and consequently the three spin projections $m_S = \{0, \pm 1\}$. The ground state (GS) is given by a spin triplet where the $m_S = 0$ and $m_S = \pm 1$ projections are separated by an electric quadrupole term. A second triplet forms an excited state (ES) connected with the ground state through an optical transition, with zero phonon lines (ZPLs) at wavelength 637 nm (1.945 eV), and associated vibronic bands that extend from their ZPLs to higher energy in absorption and lower energy in emission (see [49] for examples of the vibronic bands). The presence of two singlet states with energy in between the two triplet states has been demonstrated; they are connected by additional infrared optical transition, with ZPL at 1042 nm (1.190 eV) that is only observable during optical illumination (with energy > 1.945 eV) [50]. One of these two states is involved in an inter-system crossing (ISC) between singlet and triplet configurations via non-radiative transitions.

In first approximation, it is sufficient to consider an electronic system formed by a five-level scheme, depicted in [51] and shown in Fig. 1.1(a), defined by GS and ES triplets plus the singlet involved in the ISC; the dynamics of this transitions can be described through the decay rates towards the GS evaluated in [52] and reported in Tab. 1.1. In particular, we can note a difference of about one order of magnitude between the lifetime of the ES ($\sim$ 10 ns) and the singlet state ($\sim$ 300 ns), so that this last could be considered as a metastable state for the NV electronic spin. Moreover, we can note the presence of a faster decay towards the singlet state from the $m_S = \pm 1$ spin projections with respect to the $m_S = 0$ one, and vice versa for the decay from the metastable towards the GS; this combination results in an effective higher probability to have a spin-flip $|\pm 1\rangle_e \rightarrow |0\rangle_g$ with respect to the opposite $|0\rangle_e \rightarrow |\pm 1\rangle_g$, where the ket indicates the particular $|m_S\rangle$ quantum state and the subscript e/g the excited/ground manifold.

Exploiting this mechanism with many cycles of optical excitations with laser light it is possible to minimize the probability for the NV to be in the $|\pm 1\rangle_g$, that I will indicate with $p_{\pm 1}$, and maximize p_0 (probability to be in

Table 1.1: Transitions and decay rates Γ (from [52]). The labels correspond to the energy levels in Fig. 1.1(a) so that $\Gamma_{in,fin}$ indicates initial in and final fin levels with their spin projection $m_S = 0, \pm 1$ and manifold (the ES e, GS g or metastable m).

Transition		Rate [MHz]
Spontaneous Emission	$\Gamma_{0e,0g}$, $\Gamma_{-1e,-1g}$, $\Gamma_{+1e,+1g}$	63.48
Intersystem crossing	$\Gamma_{0e,0m}$	11.76
from ES to singlet	$\Gamma_{-1e,0m}$, $\Gamma_{+1e,0m}$	79.91
Intersystem crossing	$\Gamma_{0m,0g}$	3.25
from singlet to GS	$\Gamma_{0m,-1g}$, $\Gamma_{0m,+1g}$	2.37

$|0\rangle_g$). In this way a spin polarization is realized even if at room temperature the three different states of the GS are equiprobable because of thermal energy. In these experimental conditions, the relaxation time T_1 for each pure $|m_S\rangle$ state is usually > 1 ms. The polarization mechanism paves the way for all NV applications because it represents the usual technique for the initialization of the quantum system before all experimental sequences. Finally, the different probability to decay from the ES to the GS through the metastable state is responsible for a state-dependent photoluminescence (PL) that is exploited to discriminate between $m_S = 0$ and $m_S = \pm 1$ and so read out the spin; all these experimental routines will be discussed in Sections 1.5 and 1.6.

I underline that also other research works [51, 53, 54] report different decay rates for the internal dynamics between the electronic spin levels of NV centers. In general, their values depend on many peculiar experimental conditions, as temperature and intrinsic crystalline properties (e.g., lattice strain), leading to the possibility to have different rates for defects inside the same diamond sample; for these reasons, a complete univocal model able to predict the dynamics under different conditions has still to be developed. We are supported in our choice of the parameters reported in [52] because they are obtained with measurements on NV centers in bulk diamond at room temperature, as in our case.

1.3 Spin Hamiltonian

After describing the main characteristics of the NV energy level structure related to its electronic spin, in this section I analyze the different contributions

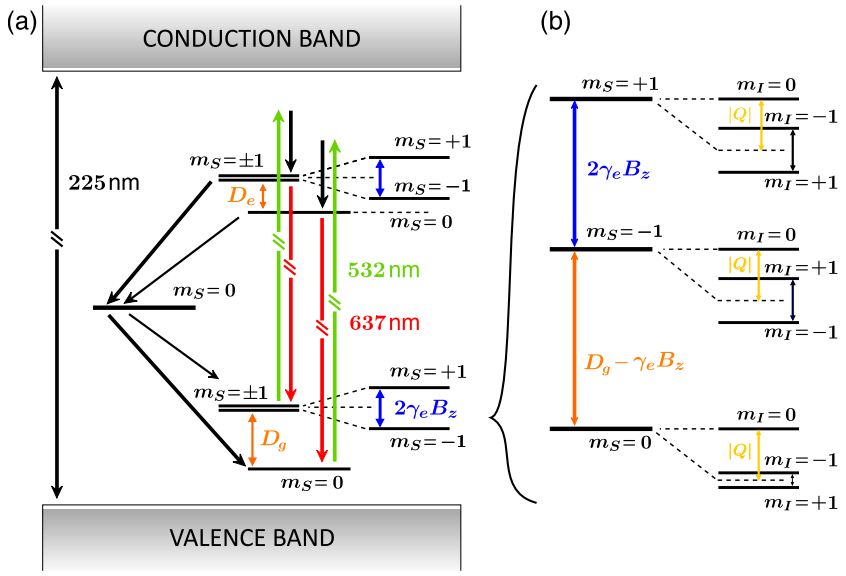

Figure 1.1: Level scheme of NV energy level structure. **(a)** Seven-level scheme of electronic structure, composed by the spin singlet $m_S = 0$ and the ground and excited state spin triplets. I show optical excitations at 532 nm (green arrows), radiative decay at 637 nm (red arrows) as well as non-radiative decay (black arrows) via the metastable level, responsible for spin polarization. The diamond valence and conduction bands, with their energy separation equal to 225 nm$\cdot h$, are schematically represented as well. **(b)** Hyperfine energy levels of the ground state considering the presence of a nuclear spin $I = 1$, as for the case of ^{14}N. For all the physical constants indicated in the figure, refer to Tab 1.2.

to the energy within each triplet manifold. I consider also the interaction with a second quantum degree of freedom that usually is intrinsically related to NV centers: The nuclear spin I associated to the nitrogen composing the defect itself.

The ground and excited triplet states of the system are governed by the same form of Hamiltonian. A detailed scheme of the level structure generated from these Hamiltonian operators is represented in Fig. 1.1 (a) and (b). The bare GS Hamiltonian for the electronic spin considered up to now, without any external interaction, would read

$$\mathcal{H}_g = D_g S_z^2, \tag{1.1}$$

where S_z is the spin operator along the NV quantization axis $\hat{z}$ and $D_g = 2.87$ GHz the electronic zero-field spitting of the GS.

In presence of an externally applied magnetic field $\boldsymbol{B}$ the Zeeman effect removes the degeneracy of $|\pm1\rangle_g$ states. Moreover, a strong coupling between

electronic and nuclear spins results in an hyperfine interaction, so that the only m_S quantum number is not sufficient anymore to uniquely describe the NV state and we resort to $|m_S, m_I\rangle$ to do it, where m_I indicates the nuclear spin projection along the quantization axis. Finally, nuclear quadrupole and Zeeman terms shift the states in energy. The final Hamiltonian results:

$$\mathcal{H}_g = D_g S_z^2 + \gamma_e \, \boldsymbol{S}\cdot\boldsymbol{B} + Q \; I_z^2 + \boldsymbol{S}\cdot\mathbf{A}\cdot\boldsymbol{I} + \gamma_n \; \boldsymbol{I}\cdot\boldsymbol{B}, \tag{1.2}$$

where $\boldsymbol{S}$ and $\boldsymbol{I}$ are the electronic and nuclear spin operators, Q represents the nuclear quadrupole interaction, γ_e and γ_n are the electronic and nuclear gyromagnetic ratios, respectively. It is evident how the fourth term of the right hand side, the hyperfine one, removes the degeneracy of the three nuclear spin projections splitting each $|m_S\rangle$ state in $2I + 1$ hyperfine levels.

The hyperfine interaction can be rewritten as:

$$\boldsymbol{S}\cdot\mathbf{A}\cdot\boldsymbol{I} = A_\parallel S_z I_z + A_\perp (S_x I_x + S_y I_y), \tag{1.3}$$

with $A_\parallel$ and $A_\perp$ amplitudes of the longitudinal and transverse coupling between the two spins. To serve as an example, in this section I consider a nuclear spin $I = 1$, as for the case of a substitutional ^{14}N.

At room temperature, the excited state (ES) Hamiltonian H_e has the same form, with a different zero field splitting D_e instead of D_g and hyperfine coupling tensor $\mathbf{C}$, so that $\boldsymbol{S}\cdot\mathbf{C}\cdot\boldsymbol{I} = C_\parallel S_z I_z + C_\perp (S_x I_x + S_y I_y)$. Indeed, in the excited state, the orbital contribution to the energy spin levels is quenched due to mixing of the excited state orbital doublet $\{E_x, E_y\}$, attributed to thermally-activated phonon excitations [55, 56]. Therefore, the excited state behaves as an effective orbital singlet like the ground state, where spin level energies are determined only by spin-spin and Zeeman interactions. This is no longer the case at cryogenic temperatures, where our model would not apply. All the quantities indicated for H_g and H_e are quantified in Tab. 1.2, considering the Planck constant $h = 1$ for sake of simplicity.

For sake of clarity, in the following treatment the states labeled with a single quantum number are always referring to the electronic spin projection m_S; every time it would not result sufficient anymore to describe the NV state, I will indicate the latter with the aid of the nuclear spin component m_I as a second quantum number.

Furthermore, in general is not uncommon to find more than one coupled nucleus, especially for diamond samples with natural abundance of ^{13}C, characterized by $I = 1/2$. This phenomenon enriches the energy level structure leading to a number of levels equal to $\prod_j (2I_j + 1)$, with I_j indicating the j-th nuclear spin.

Table 1.2: Summary of NV relevant parameters ($h = 1$). The evaluation of $C_\perp$ will be discussed in chapter 2.

	Constants	References
γ_e	2.803 MHz/G	
D_g	2.87 GHz	[57]
$A_\parallel$	-2.16 MHz	[58]
$A_\perp$	-2.62 MHz	[59]
D_e	1.42 GHz	[57]
$C_\parallel$	-40 MHz	[60]
$C_\perp$	-23 MHz	Ch. 2
Q	-4.945 MHz	[58]
γ_n	-0.308 kHz/G	

1.4 Experimental setup

In the experiments, I used single NV centers hosted in an electronic grade diamond sample, with natural 1.1% abundance of ^{13}C impurities and ^{14}N concentration < 5 ppb (Element Six). A complete scheme of the setup is reported in Fig. 1.2.

The optical part was already present at the beginning of this thesis and its first element is a laser source at 532 nm used to excite the phononic band of the GS $\rightarrow$ ES optical transition. A combination of a waveplate and a polarizing beam splitter is used to select the desired laser power and optimize the response of the following acousto optic modulator (AOM). The latter is used as a fast switch to send laser pulses sharp (rising and falling times of the AOM first order around 15-20 ns) and short (down to some tens of nanoseconds) in time. A polarization maintaining optical fiber helps to clean the spatial mode of the laser beam and decouple the optical setup in two separated parts. Then the beam is reflected from a dichroic filter that selectively pass light in the wavelength range 545-825 nm; in this way it separates the green excitation beam from the NV photoluminescence that outcomes from the diamond through the same path.

Indeed, after the dichroic the light goes through a home-build confocal microscope (with 10x of magnification), composed by two commercial objectives; the first one focuses the laser beam on the diamond collecting the PL emitted from the same focal volume; this excitation/emission volume is

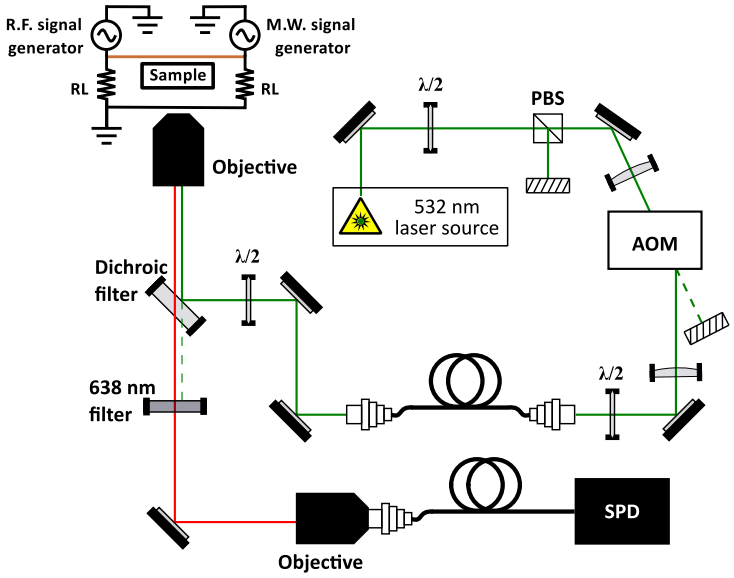

Figure 1.2: Scheme of the optical and electronic setup for the NV spins control.

around 350 nm^3, close to the diffraction limit for our laser. In order to focus the beam on top of a single NV center, we take advantage of micro and nano positioner stages driven by a control software developed with MATLAB®; we exploit the same software also to control all the instrumentation. After the emission, the 637 nm light collimated from the first objective passes through the dichroic and reaches the second objective. This last focuses on an optical fiber that works as spatial filter. Through the fiber, the collected light is sent to a single photon detector (SPD). The collecting efficiency of the system is limited by both the internal reflection of the emitted PL and the detection efficiency of the SPD itself. For this reason, an high statistics, averaging over $\sim 10^5$ repetitions for each measurement, is necessary; the error associated to the expected value is mainly given by the photon shot noise, that will be represented through the error bars in the experimental PL, shown in various graphs inside the dissertation.

In Fig. 1.2 there is also a sketch of the electronic setup to control and manipulate the NV spin state within the GS manifold. A microwave signal generator (SG), ranging from DC to 4.05 GHz, is used to induce transitions between the electronic spin projections. The wave is emitted from a copper wire with 60 μm diameter, that works as antenna, soldered to a printed circuit base (PCB). Using a second termination of the PCB to the same wire we deliver also the RF wave, useful both to induce transitions within the hyperfine manifold and generate variable magnetic fields. An arbitrary waveform

generator (AWG) is used to produce RF signals, with the possibility to create waveforms from DC to 250 MHz. The same instrument is exploited to send trigger signals to the AOM and the SG to produce the laser and MW pulses, respectively: In this way it is possible to synchronize all the possible elements of a certain measurement sequence.

Finally, to separate the $m_S = +1$ from the $m_S = -1$ components introducing static magnetic fields, the setup has a permanent NdFeB magnet, with position adjustable in all the directions with the aid of three different translation-stages and a rotation one. This allows us to completely control the orientation and alignment of the magnetic field with respect to the NV quantization axis.

1.5 Electron spin resonance

As already mentioned, usual experiments with NV centers are performed inducing transitions within the GS manifold with the aid of MW signals. The motivations of such choice rely on the fact that the energy levels, and so their energy differences, explicitly depend on the external magnetic field, that can be used as target for our quantum sensor or as a tool to engineer the energy levels themselves for quantum information purposes. Then, I point out that the easy initialization, control and manipulation of the GS spin, that I discuss in this section considering standard electron spin resonance (ESR) experiments, are the basis of the success of NV platforms for quantum technologies.

1.5.1 Continuous wave and pulsed ESR

To experimentally determine the NV ESR frequency, a first technique consists in a simultaneous laser excitation and MW radiation. The laser, as discussed, acts in order to polarize the electronic spin in the $|0\rangle$ level and, if the MW is out-of-resonance with respect to GS spin transitions, the read out of the state performed with the SPD would measure the PL related to the $m_S = 0$ component. Once the MW is on-resonance, e.g. with $|0\rangle \leftrightarrow |+1\rangle$, the spin cycles between the two states; because of a different (higher) probability to decay through the non-radiative branch, now the SPD measures a reduced fluorescence intensity. The ESR frequency is determined by monitoring the NV PL and sweeping the MW frequency; this particular ESR measurement technique is indicated with "continuous-wave ESR" (CW-ESR), where "continuous" takes its meaning from the fact that the duration of the MW is longer than the coherence time of the states involved in the transition.

Without any magnetic field the only resonance corresponds at the zero-field splitting at $D_g = 2.87$ GHz for the transitions $|0\rangle \leftrightarrow |\pm 1\rangle$. When a static field is applied with a component along the quantization axis, the degeneracy is removed via Zeeman effect and the ESR spectrum of a single NV shows two distinct resonances, as shown in Fig. 1.3(a); the amplitude of the $\hat{z}$ component of the field determines the splitting between the two dips. Certainly this is not true when collecting signal from NV ensembles, where multiple resonances would appear due to different possible NV orientations inside the lattice. This causes each NV to feel a differently oriented local field, and leads to different shifts of the energy levels among different NVs. The precision and accuracy of this technique is limited by the low contrast achievable on resonance and the microwave-power broadened linewidth, reducing the signal to noise ratio and consequently the final sensitivity (see discussion in Sec. 3.1.1).

To maximize the contrast is possible to resort to interactions between coherent GS states via short MW pulses. To achieve it the MW driving has to be on resonance with a given transition, leading to a coherent oscillation of the population p_{m_S} of the two spin sublevels. These oscillations are nothing else than Rabi nutations (see [61]). Considering for instance the $|0\rangle \leftrightarrow |+1\rangle$ transition, the measurement routine starts with the optical initialization in $|0\rangle$; then a MW pulse coherently transfer the spin population and the resultant NV state is finally read out by measuring the fluorescence intensity under a second laser pulse. The duration of the SPD acquisition (80-150 ns) and its relative delay with respect to the laser pulse (50-100 ns) are set in order to maximize the count rate but to conclude the acquisition before the polarization process given by the laser occurs (after ~ 300 ns).

The characteristic frequency of the coherent oscillation of the population between the states is the measured Rabi frequency Ω', defined by:

$$\Omega' = \sqrt{\delta^2 + \Omega^2}, \tag{1.4}$$

where δ is the detuning from the ESR and $\Omega = \gamma_e B_{MW}$ represents the bare Rabi frequency given by the orthogonal component of the MW magnetic field emitted by the antenna. Considering $\delta = 0$, the Rabi frequency $\Omega' = \Omega$ would depend only on MW field amplitude; so, the population transfer level depends on just pulse amplitude and length. Once fixed the first, it is possible to produce a different superposition of the two states (i.e. populations balance) simply changing the MW pulse duration. So, by acquiring the PL as a function of MW duration it is possible to reconstruct the Rabi nutation dynamics. An example of this measurement is shown Fig 1.3(b), where a maximum in fluorescence intensity corresponds to $p_0 = 1$ and a minimum to $p_{+1} = 1$. I would underline that Rabi nutations are subjected to a decay

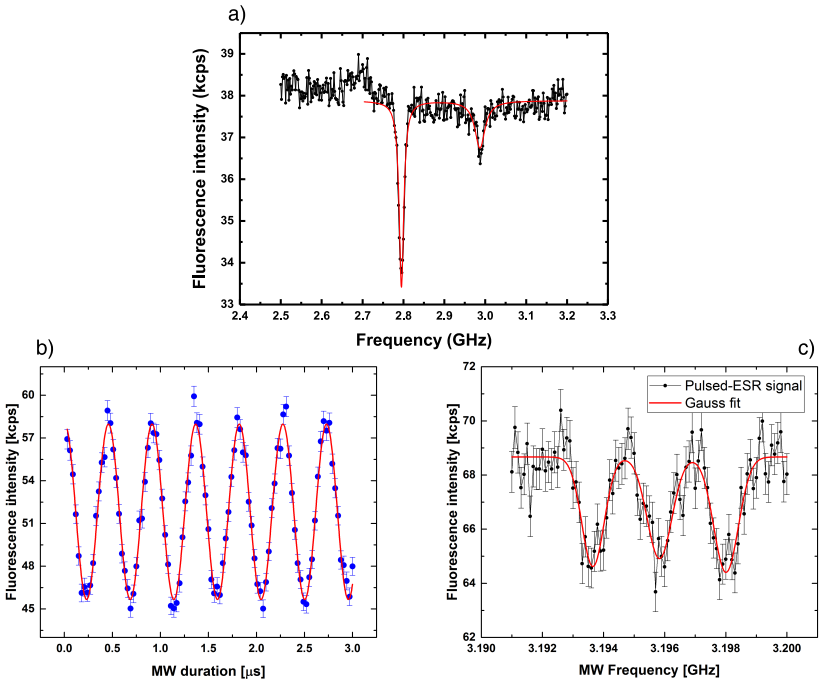

Figure 1.3: Electron spin manipulation. **(a)** Continuous-wave ESR: Measured fluorescence intensity as a function of the MW frequency (black scatter) where both $|0\rangle \leftrightarrow |-1\rangle$ and $|0\rangle \leftrightarrow |+1\rangle$ transitions are visible as dips in PL. From a Lorentzian fit (red line), the measured static magnetic field is 64 ± 0.6 G with an angle of $79° \pm 2°$ with respect to the quantization axis. The different depth of the two resonances is due to a different efficiency of the antenna emission depending on the MW frequency, that affects the effective MW power reaching the NV. **(b)** Rabi nutation measurement: Blue scatters correspond to experimental PL data acquired for different MW durations, where high/low fluorescence correspond to high probability to be in $|0\rangle/|+1\rangle$; red solid line is a cosine fit of data. **(c)** Pulsed-ESR measurement on $|0\rangle \leftrightarrow |+1\rangle$ electronic transition: PL as a function of MW frequency for a MW power equal to -14 dBm set on SG (black scatter). The three resonances correspondent to ^{14}N hyperfine states are resolved and clearly visible. Red solid line correspond to Gauss fit of experimental data.

in amplitude due to inhomogeneous broadening of the transition; moreover, some beatnotes are often present due to a detuned driving of different hyperfine transitions. The amplitude of these beatnotes depends on the probability of the NV to populate different hyperfine states.

Considering to apply MW pulses with a specific length t_{MW} in order to obtain a specific arbitrary superposition of the electronic levels, the most remarkable cases are certainly $\Omega t_{MW} = \pi/2,\pi$, the so called $\pi/2$ pulse and

π pulse, respectively; starting from a pure state like $|0\rangle$, the first creates a perfect superposition of the two levels involved in the transition ($p_0 = p_{+1} = 0.5$, in our example), meanwhile the second transfers all the population to the second level ($p_{+1} = 1$).

In particular, delivering a π pulse after initializing the spin in $|0\rangle$ and measuring the PL as a function of the MW frequency, it is possible to obtain an ESR spectrum that, comparing to CW-ESR measurements, exhibits an higher contrast (a factor of 2 at the same MW power) and much higher resolution (up to ≤ 1 MHz). In Fig. 1.3(c) I report an example of this kind of measurements that I will define "pulsed-ESR" in the text, to distinguish them from the CW version; we can note the presence of three distinct resonances, signature of the GS hyperfine structure.

In fact, as discussed before in Sec. 1.3, the possible transitions $m_S \to m'_S$ are $2I + 1$, since the nuclear spin I is conserved in the electronic transition. Considering to have ^{14}N, referring to Eq. (1.2) and the parameters shown in Tab. 1.2, the transition energies differ from each other by $hA_{\parallel}$, so that the three $|0, m_I\rangle \leftrightarrow |+1, m_I\rangle$ can be distinguished.

Finally is trivial to note that to obtain a precise measurement of the π-pulse length in order to be able to perform a pulsed-ESR a knowledge of the ESR frequency is necessary and vice versa; therefore, usually this issue is overcome by iterating the procedure starting to evaluate the ESR frequency from a CW measurement.

1.5.2 Ramsey spectroscopy

Once maximized the contrast by means of a pulsed sequence, it is possible also to enhance the spectral resolution with the aid of interferometric techniques, based on Ramsey spectroscopy. This measurement method rely on the different evolution of states after the interaction with a monochromatic field depending on the detuning between the excitation and the transition energies, the so called free induction decay [61, 62].

In particular, once initialized the system, if a MW pulse with a length t is applied in order to obtain a superposition with another electronic state, e.g. $|+1\rangle$, the state of the system is[2]

$$|\psi\rangle = a_0 |0\rangle + a_{+1} |+1\rangle , \tag{1.5}$$

with a_0, a_{+1} probability amplitudes related to the states $|0\rangle$,$|+1\rangle$, respectively. For the case of a two level system interacting with a monochromatic

[2]Unless otherwise specified, we consider to have a bias magnetic field directed along $\hat{z}$. In this way, $|m_S\rangle$ are the eigenstates of the system and the degeneracy between $m_S = \pm 1$ is removed.

MW field, leaving the spin to evolve for a time T and applying a second MW pulse with the same duration t, the probability amplitude for the $|+1\rangle$ case reads

$$a_{+1} = \frac{\Omega'}{\Omega}\left[\frac{1-e^{i\Omega' t}}{2} + e^{i\delta T}\frac{1-e^{i\Omega' t}}{2}\right]. \tag{1.6}$$

Here, the first term of the right hand side of the equation corresponds to the amplitude arising from the first pulse and the interaction with the second pulse produces a similar term, but multiplied by a phase factor dependent on δ and the free evolution time T. The probability to find the NV in the state $|+1\rangle$ after the second MW pulse becomes:

$$p_{+1} = \left(\frac{\Omega'}{\Omega}\right)^2 \sin^2\left(\frac{\Omega' t}{2}\right)\cos^2\left(\frac{\delta T}{2}\right). \tag{1.7}$$

This equation is similar to what we could obtain for the Rabi nutation case for a pulse that lasts t, but with an additional oscillating term.

By choosing $t = \pi/2\Omega'$, i.e. applying two $\pi/2$ pulses, we maximize the probability to transfer population from $|0\rangle$ to $|+1\rangle$. This is the so called Ramsey spectroscopy technique, represented by the experimental sequence shown in Fig. 1.4(a). From Eq. (1.7) we can note that for $\delta = 0$ (on-resonance pulses) p_{+1} reduces to 1 as for the simple π-pulse case without any free evolution ($T = 0$ case). By changing the detuning, the obtained p_{+1} modulations are the Ramsey fringes, characterized by a spectral linewidth $\Delta\nu = 1/2T$, that is, to the detuning corresponding to the first p_{+1} minimum. This means that with a typical free evolution time $T \sim 2$ μs the spectral resolution for an ESR transition would be 250 kHz, so below the best conditions with pulsed-ESR measurements.

As a consequence, in the presence of hyperfine structure, it is possible to exploit the free induction decay to easily resolve the various transitions. A typical measurement of free induction decay through Ramsey experiment is shown in Fig. 1.4(b); we can note the usual presence of many oscillation components, indicating the presence of detuned states evolving with $\cos^2(\delta T/2)$. The level structure of the defect becomes clear considering the Fourier transform (FT) of the signal, shown in Fig. 1.4(c) for a particular NV; it exhibits two distinct triplets, signature of the presence of not only the nitrogen composing the NV itself, but also of a second strong coupled nucleus, with spin $I = 1/2$ and an hyperfine parallel component $\omega_\parallel \simeq 12$ MHz, ascribable to a nearby ^{13}C nucleus. The peaks in general have different amplitude depending on the population of the m_I spin projection as a result of a dynamic nuclear polarization process, that we will discuss in depth in Ch. 2.

In solid-state systems, the achievable precision of the Ramsey scheme is affected by the strong limitation of fast dephasing of NV electronic spin

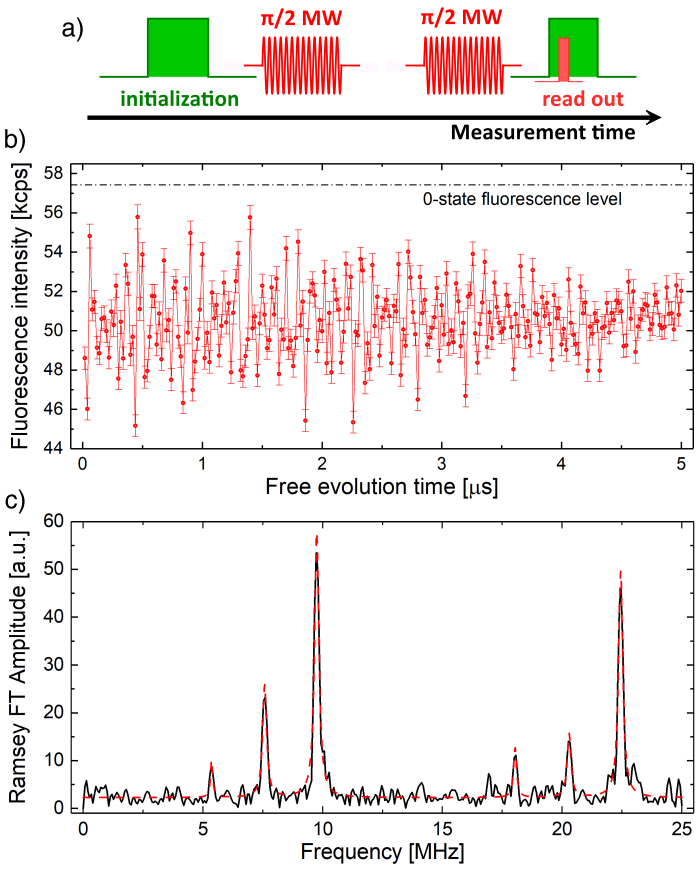

Figure 1.4: Measurement of ESR frequency via Ramsey spectroscopy. **(a)** Scheme of the experimental sequence. Green and pink square waves represent laser and SPD pulses used to initialize and read out the state, respectively. Red curves are the MW $\pi/2$ pulses separated by a free evolution time T. **(b)** Scatter of experimental PL acquired as a function of T. **(c)** Fourier transform of experimental data shown in (b) (black solid line) and Lorentzian fit of the peaks related to six different hyperfine transitions (see text). The two strong components around 10 MHz and 22.5 MHz explain the initial value of the time-dependent plot in b), where the first point correspond to $T = 40$ ns.

that limits the available interrogation time. The characteristic time scale of dephasing is defined T_2^*, determined by inhomogeneities in the environment. For a sample with natural abundance of ^{13}C, 1.1 %, dipolar hyperfine coupling with their nuclear spin bath is the main source of NV dephasing, giving temporal fluctuations in the local magnetic field due to dynamics in the bath: The nuclei precess around magnetic fields which are usually externally applied, producing random-phase time varying fields on NV spins. Then,

variations in the local spin environment (i.e. local impurities close to the defect) experienced by each NV center cause different (coherent) interactions that would also change the local field. The coherence W of NV spin goes with $W = e^{-T/T_2^*}$, where for similar kind of diamonds the usual T_2^* is on the order of 3-5 μs.

Since the typical time to drive and control the electronic spin, represented by the time t_π needed to perform a π pulse, is on the order of tens of nanoseconds or less, it is possible to perform a number of manipulations on the order of 10^2 before dephasing occurs. On one hand, for the main scientific purposes and applications this would not be enough. However, in general the sensitivity of a sensor also depends on the possibility to measure the target field for long times without losing information; it is therefore clear that enhance the coherence of the NV spin as much as possible is in general a first important step to make it competitive for quantum sensing purposes. Anyway, the Ramsey scheme remains a fundamental tool and it is included among the main measurements techniques that I will discuss because, together with the optical read out, it easily enables to measure the electronic spin state coherence.

1.6 Environment-spin decoupling

To enhance the coherence of the electronic spin in general it is possible to take advantage of many techniques, based on spin-echo [63], developed for nuclear magnetic resonance purposes in the last decades and more recently revisited in the context of quantum information processing. These techniques allow us to decouple the NV spin from the diamond environment. In this way, the coherence time T_2 is increased up to hundreds of microseconds for single NV centers at room temperature in bulk diamonds with natural abundance of ^{13}C nuclei, towards the ultimate limit of the relaxation time $T_1 \sim 1$ ms. In this section I briefly introduce a model for the environmental noise, some of the methods used to filter it and their applications to NV platform.

In the presence of a static magnetic field $\boldsymbol{B}$ directed along $\hat{z}$, the nuclear spins composing the ^{13}C bath start to precess around the field axis with the characteristic Larmor frequency $\omega_L = \gamma_C B$, with $\gamma_C = 2\pi \times 1.08$ kHz/G gyromagnetic ratio of the ^{13}C nucleus.

This spin bath, interacting with the NV electronic spin, represents the main noise source for centers hosted in diamond with natural abundance of ^{13}C nuclei, and its characterization is therefore fundamental to develop strategies to increase the coherence of the system for both quantum sensing and information applications. The study of the diamond environment will

be the subject of Chapter 4. For now, since the nuclear spins are randomly both oriented and spatially distributed, we can limit ourselves to consider the bath as a source of a stochastic variable magnetic field centered at frequency ω_L. Therefore, they induce an additional rotation of the NV electronic spin around the $\hat{z}$ axis with the Hamiltonian operator

$$H_{int} = \gamma_e \, \beta(t) S_z \tag{1.8}$$

representing the interaction between the electronic spin and the environment, where $\beta(t)$ is a stochastic variable with power spectral density $S(\omega)$ in the frequency domain.

Under the assumption of a Gaussian stationary noise, the noise-induced decoherence is described by a simple function $\chi(T)$ [64], called decoherence function, associated with the decay of the signal (i.e. the population) $p(t)$ during the sensing time t:

$$p(t) = \frac{1}{2}\left(1 + e^{-\chi(t)}\right). \tag{1.9}$$

The decoherence function can be identified with the root mean squared phase accumulated from the NV around the $\hat{z}$ axis during the evolution time:

$$\chi(t) = \frac{1}{2}\phi^2_{rms}. \tag{1.10}$$

Therefore, $\chi(t)$ will also depend on the particular control sequence applied to the spin, that influences this phase. Considering that the control is described by modulation function $y(t)$, the decay function is determined by the correlation integral:

$$\chi(T) = \int_0^\infty \frac{d\omega}{\pi} S(\omega) \left|\mathcal{Y}_T(\omega)\right|^2, \tag{1.11}$$

where T is the total time of the sequence and $\left|\mathcal{Y}_T(\omega)\right|^2$ is the so-called filter function of the control sequence, defined by the finite-time Fourier transform of $y(t)$:

$$\mathcal{Y}_T(\omega) = \int_0^T y(t) e^{i\omega t} \, dt. \tag{1.12}$$

$\mathcal{Y}_T(\omega)$ represents the transfer function of the noise spectral density related to the specific control sequence. For a detailed analysis of the filter function for the case of pulsed sequences see App. B; a further discussion can be also found in [7].

1.6.1 Spin refocusing

The first fundamental technique for the decoupling from the environment is the so called spin-echo (or Hahn-echo) [63], schematically represented in Fig. 1.5. The first steps are the initialization in $|0\rangle$ and the creation of a superposition between two m_S states with the aid of a $\pi/2$ pulse. Then, after a free evolution time τ, a resonant MW π pulse is applied in order to prevent the dephasing: Its effect is to imprint a π phase on the NV electronic spin (i.e. obtain the inversion of the temporal evolution). At this point, if we wait τ again, a complete refocusing of the spin is obtained and a second $\pi/2$ pulse would project in the final state, again $m_S = 0$, in principle with fidelity $\mathfrak{F} = 1$.

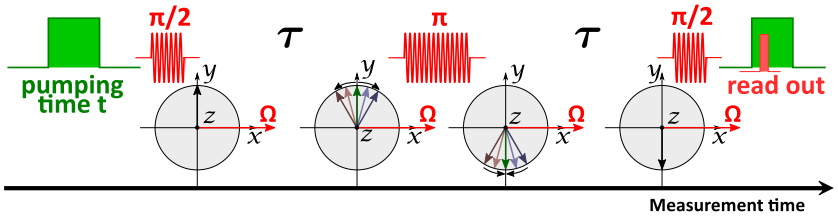

Figure 1.5: Spin-echo scheme for NV electronic spin refocusing. Top row: Commands time sequence of laser and MW pulses; bottom row: Top views of the Bloch sphere with spin evolution along the sequence: Thanks to a first $\pi/2$ pulse, the NV electronic spin (represented by the black arrow) rotates around the Rabi vector (red arrow) with a frequency Ω and reaches the equatorial plane of the Bloch sphere. During the evolution time τ, the spin vector is "spread" (colored arrows) due to inhomogeneities of the environment. The π pulse induces a rotation of all the components around Ω; consequently, "clockwise" and "anticlockwise" rotating components of the spin refocus themselves after waiting a second τ interval and the last $\pi/2$ pulse would complete an effective 2π pulse, re-projecting the spin in $m_S = 0$.

On the other hand, the presence of noise with a spectrum centered in ω_L, that influences $\chi(t)$, has to be taken into account. In a spin-echo sequence, the control function is represented by a sign switch in the evolution given by the π-pulse operation, and the Eq. (1.12) becomes:

$$\mathcal{Y}_{2\tau}(\omega) = \int_0^{\tau} e^{i\omega t}\, dt - \int_{\tau}^{2\tau} e^{i\omega t}\, dt = \frac{4e^{i\omega\tau}}{\omega} \sin^2\left(\frac{\omega\tau}{2}\right). \tag{1.13}$$

The filter function exhibits a periodicity in frequency, with maximum and minimum values correspondent to $\omega_m = m\pi/\tau$, with m odd and even integers, respectively. The periodic function is in turn multiplied by an amplitude scaling $1/\omega$, so that the filter results in a sinc-like function, with periodic

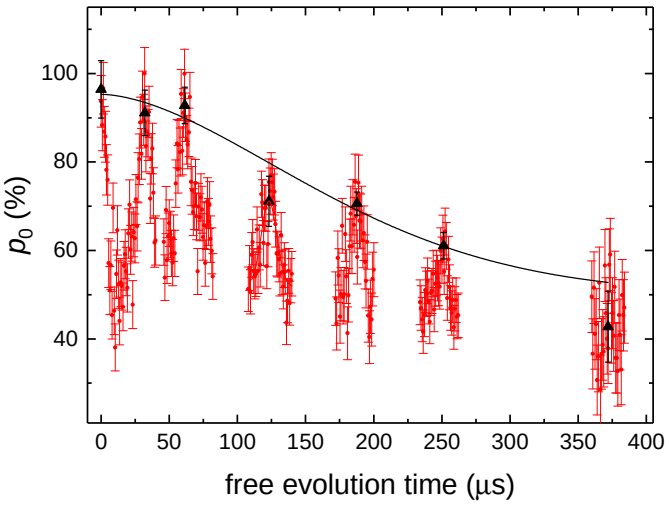

Figure 1.6: Example of spin-echo measurement. $|0\rangle$ state probability p_0 as a function of the free evolution time. Red dots are experimental data for the $|0\rangle \rightarrow |+1\rangle$ transition at $B_z \sim 64$ G; the collapses-revivals trend with period $2\pi/\omega_L$ is clearly visible. The black scatter represents the envelope of the spin-echo signal, given by the amplitude associated to Gaussian fit of each revival with its error; black solid line is a fit of $\exp[-(t/T_2)^k]$ to the overall signal decay, where the exponent k is a fit parameter [65] and the long term baseline is taken to be 0.5 (mixed-spin-state case). For the measurement shown, $T_2 = 205 \pm 22$ μs and $k = 1.7 \pm 0.7$.

revivals with decreasing amplitude. From these considerations, we can see how the spin-echo sequence makes the NV center insensitive to all the noise frequencies correspondent to $Y_{1,\tau} \cong 0$, and that the effect of $S(\omega)$ (that is peaked in $\omega = \omega_L$) becomes relevant (meaning χ different from 0) only for sensing times $\tau_j = 2j\pi/\omega_L$, j integer number. For all the other values of τ, the electronic spin is decoupled from the nuclear spins environment.

All these features lead to a modulation on the trend of the signal $p(t)$, characterized by collapses and revivals with periodicity given by the Larmor frequency of the bath. An example of this dynamics is shown in Fig. 1.6, where the experimental p_0 population (i.e. the probability to find the NV in the $|0\rangle$ state) is represented by normalizing the measured PL level to the $|0\rangle$ and $|+1\rangle$ references through:

$$p_0 = \frac{s(T) - s_{+1}}{s_0 - s_{+1}}, \tag{1.14}$$

where $s(T)$ is the fluorescence signal at the measurement time T, and s_0 and s_{+1} are the PL related to $|0\rangle$ and $|+1\rangle$ spin states, respectively. I will use this same notation, including also the definition $p_{\pm 1} = 1 - p_0$ for the populations of the $|\pm 1\rangle$ states, along the remained part of this dissertation. In Fig. 1.6 we can note how the finite width of both filter and noise spectrum results in a non-perfect noise filtering for long measurement times; this leads to decoherence of the NV spin, i.e. a decay of the signal with typical times $T_2 \geq 100$ μs, that is still two order of magnitude longer than the one of the free induction decay case.

1.6.2 Dynamical decoupling

Starting from the spin-echo sequence, it is possible to extend the environment decoupling by means the use of series of π pulses: This method is indicated as dynamical decoupling (DD) [66]. Even if DD has been initially devised in nuclear magnetic resonance research field in the last decades, it is widely used in many different platforms, including quantum sensors such as defects in diamond.

Defining n the total number of π pulses along the sequence, it is possible to redefine the decoherence function starting from Eq. (1.11):

$$\chi_n(T) = \int_0^\infty \frac{d\omega}{\pi} S(\omega) \left| \mathcal{Y}_{n,T}(\omega) \right|^2 , \tag{1.15}$$

where $|\mathcal{Y}_{n,T}(\omega)|^2$ represent the filter function given by n flips in the temporal evolution generated by the π pulses (see App. B).

The most relevant DD sequences include first of all the ones with equally spaced π pulse, like Carr-Purcell-Meiboom-Gill (CPMG) [67, 68] and periodic dynamical decoupling (PDD) [69]. These first examples rely on the approximation to have perfect pulses able to completely reverse the states populations; in particular, the finite duration, non-perfectly shape and the possible uncertainties on the phase of the pulses affect the process reducing the fidelity of each spin manipulation. To overcome these imperfections it is possible to take advantage of rotations of the spin around different directions of the Bloch sphere: The sequences are based on $\hat{x}$ and $\hat{y}$ phase alternation of the π pulses (performed with the same timing as for CPMG), compensating for cumulative pulse errors for all three components of magnetization; they are therefore named XY sequences [70, 71].

Nevertheless, DD sequences with equidistant pulses are still extremely fragile with respect to possible noise frequencies $\omega \sim 1/\tau$, where τ is the inter-pulses spacing, and their harmonics. To avoid this, it is possible to resort to

non-equidistant sequences, like Uhrig dynamical decoupling UDD [72], that is very efficient to cancel strong couplings to the environment. Finally, I would mention the case where the whole sequence is divided in groups with odd number of π pulses [73, 74]; there are now two different time (i.e. frequency) constants: One related the intra-group time interval, the other to the inter-group one. These sequences, to which I will refer as adaptive-DD ones, have been demonstrated to be very robust against experimental instabilities, like shifts of the transition energy (or, equivalently, pulses' detuning) or non-perfect π-pulse duration; moreover, they are still compatible with corrections routines via phase alternation. A scheme of all mentioned sequences can be found in Fig. 1.7.

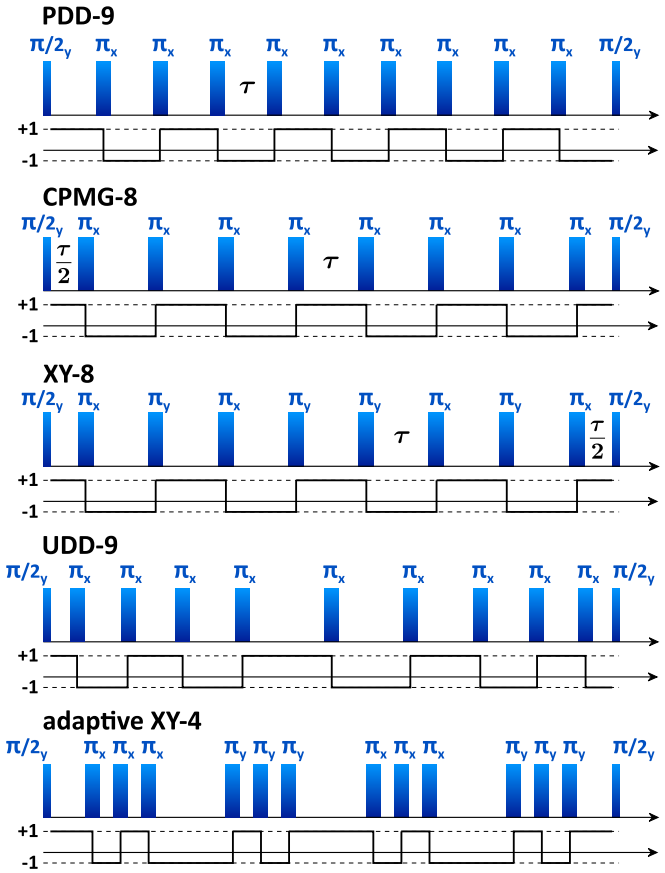

Figure 1.7: Schemes for different dynamical decoupling sequences. The π-pulses distribution as a function of the time is shown, from top to bottom, for PDD, CPMG, XY-8, Uhrig, and adaptive-XY-4. Below each pulses distribution, the correspondent control function $y_n(t)$ is represented as well.

Chapter 2

Control and initialization of the NV nuclear spin

The presence of other nuclear spins in the proximity of the NV defect can be exploited to enhance quantum computation or sensing tasks, for example to achieve better readout [75, 76], long-time memory [77], or to implement quantum error correction schemes [19, 78, 79]. A critical step in many of these schemes is to first initialize the nuclear spin in a highly polarized (pure) state [36, 57, 58, 80–82].

To do this, a precise knowledge of a quantum system's Hamiltonian is a critical pre-requisite. In this chapter, I report a method for the precise characterization of the non-secular part of the excited-state Hamiltonian of an electronic-nuclear spin system in diamond. The method relies on the investigation of the dynamic nuclear polarization (DNP) mediated by the electronic spin: Close to the excited state level anticrossing (ESLAC), occurring at magnetic field around 510 G, the transverse hyperfine coupling induces electron-nuclear flip-flops, and consequently polarization transfer from electron to nuclear spins [81]. The polarization transfer dynamics, and its ultimate achievable level, depends critically on the hyperfine spin structure of the ground and excited electronic levels. By studying the population of the GS hyperfine levels of a nitrogen-vacancy center, we obtain the first direct estimation of the excited-state transverse hyperfine coupling between its electronic and nitrogen nuclear spin [83]. Our method could also be applied to other electron-nuclear spin systems, such as those related to defects in silicon carbide.

DNP is currently exploited as a primary tool for initializing nuclear qubits and performing enhanced nuclear magnetic resonance. A deeper understanding of this mechanism would allow us enhanced control of this multi-spin system, from its initialization to more complex sensing and computational

tasks. Our strategy combines measuring the time-dependence of the polarization dynamics with *ab initio* calculations based on a master equation in the Lindblad operator formalism [84].

The chapter is organized as follows: In section 2.1 I introduce the techniques used to control the nuclear degree of freedom belonging to NV centers, discussing the opportunity and feasibility of production of single hyperfine spin states. In Sec. 2.2 and 2.3 I present the DNP mechanism and the method used to experimentally measure it. Sec. 2.4 is dedicated to the model used to describe the nuclear polarization phenomenon and perform *ab initio* calculations to predict its dynamics, introducing the Lindblad operator formalism; I also discuss possible limitations in our treatment, as effects of charge-state conversion dynamics of the NV center. Finally, I analyze the two main regimes of DNP: The stationary one, where DNP exhibits the same rate of the optical spin pumping (Sec. 2.5), and the dynamical one for small pumping time, which allows us to get a precise estimation of the excited-state transverse hyperfine coupling (Sec. 2.6).

2.1 Hyperfine states control

I consider again the two-spin system given by the electronic spin $S = 1$ associated with the NV center, in its orbital ground and excited states, and the nuclear spin $I = 1$ of the substitutional ^{14}N that constitutes the center.

In this section I briefly illustrate the methods used to manipulate and control the nuclear degree of freedom via nuclear magnetic resonance tools. As we discussed in Sec. 1.4, the setup presents also the possibility to deliver RF waves affecting the NV centers. This represents a fundamental tool to achieve a complete control of the NV center and engineer systems selecting the number of states, from 2 to $2(2I + 1)$.

The RF wave is created with the aid of the arbitrary waveform generator and sent to the copper antenna after passing through an amplifier. Since we are dealing with magnetic dipole transitions between nuclear states, I underline that their rate is much smaller than the one related to electronic transitions. In fact, considering to have just two nuclear spin levels involved in the hyperfine transition, i.e. a two-level system, the interaction strength is proportional to the nuclear magneton μ_N and the relative Rabi frequency Ω_n results:

$$\Omega_n = \gamma_n B_{RF} = g_n \mu_N B_{RF}, \tag{2.1}$$

where B_{RF} is the magnetic field associated to the RF wave, and g_n the g-factor of the specific nucleus, in general on the order of the unity. So, it is easy to note that the order of magnitude of Ω_n is around $\mu_B/\mu_N \sim 2000$ times

smaller than typical electronic Rabi frequencies, so tens of μs. In particular, for the ^{14}N nucleus the gyromagnetic ratio is $\gamma_n = 0.308$ kHz/G (about 9000 times smaller than γ_e).

These considerations imply first of all a linewidth associated to the transition much smaller than the one related to an electronic one, therefore requiring a precise knowledge of the transition energy, that is, frequency, that has to be associated to the RF wave. Restricting ourselves to the $m_S = 0$ hyperfine manifold, the Hamiltonian in Eq. (1.2) related to the N nucleus, defined H_N, reduces to:

$$H_N = QI_z^2 + \gamma_n \left(B_z I_z + B_x I_x\right) = QI_z^2 + \gamma_n B \left[\cos(\alpha) I_z + \sin(\alpha) I_x\right]. \quad (2.2)$$

The leading term is given by the nuclear quadrupole one, with $Q = 4.945$ MHz, even if the angle between the static magnetic field and the nuclear spin quantum axis, α, is in general much different from 0. Indeed, the corrections to the energy levels with respect to the case of a magnetic field aligned with I_z are very small, quantified through the solutions of the characteristic polynomial of Eq. (2.2):

$$\lambda^3 - 2Q\lambda^2 + (Q^2 - \gamma_n^2 B^2)\lambda + \frac{Q}{2}\gamma_n^2 B^2 (1 - \cos(2\alpha)) = 0. \quad (2.3)$$

Experimentally, we found corrections to the energy transitions on the order of 1 kHz, so much smaller than Q, at fields $B = 530$ G. This is also a signature that we can still consider $|m_I\rangle$ as nuclear spin states.

2.1.1 Measurement of ^{14}N nuclear magnetic resonance

Once discussed the typical energies involved in the nuclear magnetic resonance transitions, now I describe the experimental methods used to induce them and perform their measurement. To do it, I consider the two-level transition $|0, +1\rangle \rightarrow |0, 0\rangle$, considering to start in a pure state $|0, +1\rangle$. Even if this example is very specific for a spin system given by the NV energy structure, I consider it on purpose since it is the most common experimental condition for a two-level system within the NV hyperfine manifold, achievable via dynamic nuclear polarization, that is subject of the next parts of the chapter, or exploiting some initialization procedures that I will describe in Sec. 2.1.2.

So, the first problem that we need to consider is how to measure transitions between nuclear spin states, or equivalently what could be a good observable for them. In principle, is not always possible to distinguish different hyperfine states belonging to the same m_S manifold through the fluorescence

intensity. Fortunately, it is possible to map different nuclear spins onto different electronic states and exploit the different PL of the latter ones. A scheme of the procedure is shown in Fig. 2.1(a).

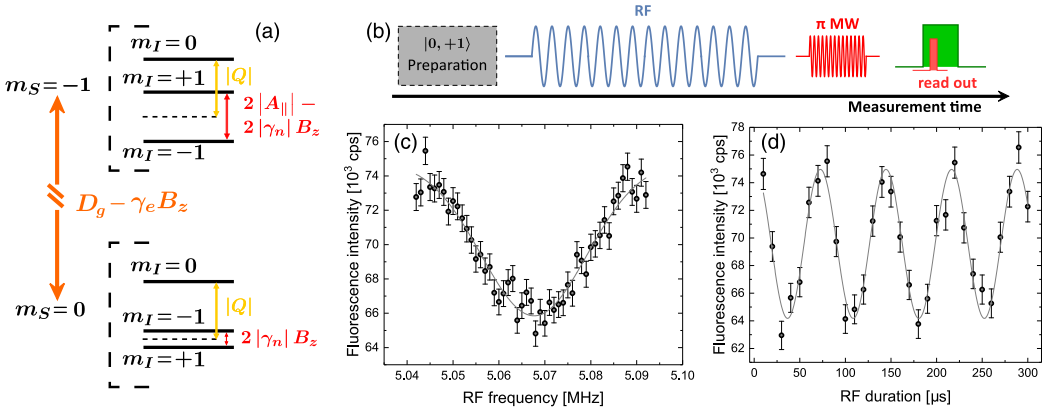

Figure 2.1: $|0,+1\rangle \rightarrow |0,0\rangle$ hyperfine spin resonance characterization. A static magnetic field $B \simeq 410$ G removes the degeneracy between $|0,\pm1\rangle$ states. **(a-b)** Schemes of $m_S = 0, -1$ hyperfine manifolds and used experimental sequences (see text). **(c)** $|0,+1\rangle \rightarrow |0,0\rangle$ nuclear magnetic resonance: Black dots are experimental PL as a function of RF frequency, gray solid line is a Gaussian fit of the data. **(d)** Rabi nutation measurement: Experimental PL as a function of RF duration (black dots) and cosine fit of data (gray solid line).

After the initialization in $|0,+1\rangle$, a RF pulse is delivered to the NV, typically with duration of 30-60 μs in order to induce the hyperfine transition; after that, a calibrated MW π pulse at low power and on resonance with the $|0,0\rangle \rightarrow |-1,0\rangle$ is used to selectively move only the population in $m_I = 0$. Finally, an SPD pulse, associated with green laser excitation light, reads out the system. The possible final states for this kind of sequence are two: If the RF is out of resonance, the NV remains in $|0,+1\rangle$, the MW is ineffective and the measured PL is the one related to $m_S = 0$; otherwise, with an RF on resonance with the $|0,+1\rangle \leftrightarrow |0,0\rangle$ energy difference, the MW induces the electronic transition and the read out pulse measures the fluorescence related to $m_S = -1$, that is, a lower photon count rate.

So, detecting the PL as a function of the RF frequency, it is possible to measure a nuclear magnetic resonance in a similar way to what we discussed for the ESR. An example of this kind of measurement is shown in Fig. 2.1(b). Since the two hyperfine spin states involved in the measurement are coherent[1] between each other on the timescales of the measurement, the contrast depends on the RF duration t_{RF} and in general oscillates in between the

[1] Coherence time of NV hyperfine states are in general above 1 ms.

best condition, correspondent to with $t_{RF}\Omega_n = \pi$ for $|0,+1\rangle \rightarrow |0,0\rangle$, and the worst case scenario with $t_{RF}\Omega_n = 2\pi$. Anyway, once obtained a first experimental evaluation of the hyperfine spin resonance, with the same experimental scheme it is possible to set that RF frequency and change t_{RF}, that is, perform a Rabi nutation measurement (see Fig. 2.1(c)).

2.1.2 Preparation of single hyperfine states

These same procedures can be exploited to characterize all the possible hyperfine states and transitions, once implemented an experimental routine that allows us to initialize in an arbitrary $|m_S, m_I\rangle$, and considered the selection rule related to the difference between initial and final nuclear spin projections $\Delta m_I = \pm 1$.

I underline that the preparation of a highly polarized state is a critical step for many important applications, ranging from long-time memory [77] to quantum error correction schemes [19]. Therefore, in this section I present a first simple example of possible experimental sequences used to obtain a specific single spin state.

In general, with small static magnetic fields ($B < 100$ G), at room temperature the probability to occupy a specific m_I state of the ^{14}N is the same for all the three nuclear spin projections. To initialize the NV state in a given hyperfine component (e.g. $|0,+1\rangle$) we can exploit one of the $m_S = \pm 1$ manifolds (I will consider for instance $m_S = -1$), and combine the possibility to selectively manipulate m_S or m_I without changing the other quantum number thanks to MW or RF pulses, respectively. A complete scheme of the experimental procedure is shown in Fig. 2.2.

However, for similar sequences, a preliminary characterization of the hyperfine transitions is necessary and would be performed with a finite probability for the NV to be in a spin state not-involved in the transition itself, limiting the contrast (i.e. the achievable precision) in NMR and Rabi measurements. Moreover, I underline that similar initialization techniques are inefficient because they requires many manipulations of the NV spin, highly increasing also the initialization time. Both these limitations, many manipulations with limited precision and long times (from some tens to more than 100 of microseconds) fighting against the spin decoherence, could affect the final fidelity of the whole procedure.

As I explain in the next section, at higher magnetic field, the peculiar energy structure of NV centers enables the possibility to have a nuclear spin pumping together with the electronic one. This dynamic nuclear polarization allows us to set up initialization routines much faster than the previous one and leads to high accuracy in the preparation of a single hyperfine spin state.

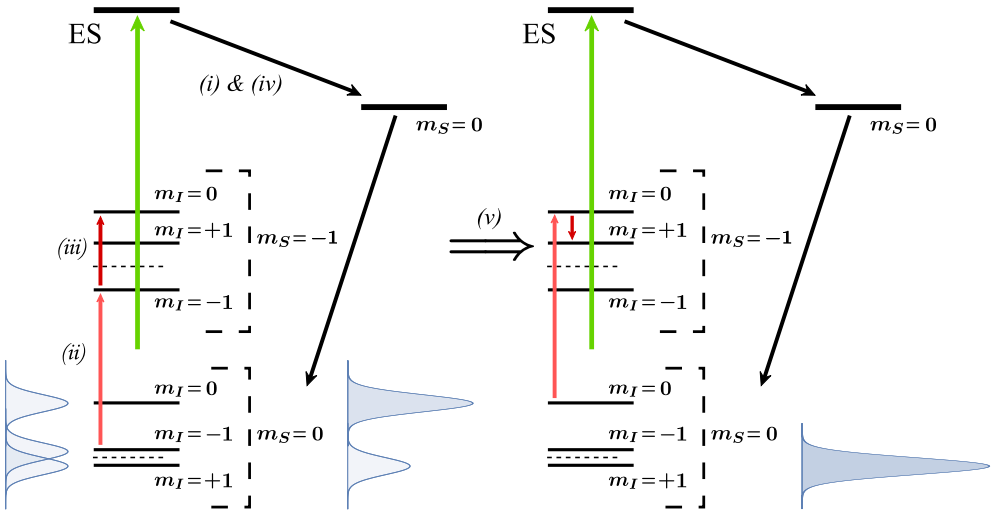

Figure 2.2: Scheme of an initialization sequence, supposing to require a pure $|0,+1\rangle$ state. It is composed by: ***(i)*** a laser pulse to polarize in $|0,m_I\rangle$ exploiting the ISC (green and black arrows), ***(ii)*** a low power MW π pulse on resonance with $|0,-1\rangle \rightarrow |-1,-1\rangle$ (light red arrow), ***(iii)*** a (previously calibrated) RF π pulse to induce $|-1,-1\rangle \rightarrow |-1,0\rangle$ (dark red arrow), ***(iv)*** a second laser pulse to polarize in $|0,(0,+1)\rangle$: Now the probability for the NV to be in $|0,-1\rangle$ is 0, ***(v)*** repeat an analogous procedure to polarize from $|0,0\rangle$ to $|0,+1\rangle$. In the figure are also schematically represented, from left to right, the probability amplitudes related to $|0,m_I\rangle$ states at the end of *(i)*, *(iv)* and *(v)*; the Gaussian line-shape is just a guide for the eye and representative of the transition one

.

At the same time, close to the excited state level anti-crossing, since the $|m_S\rangle$ spin states are not well defined anymore (see Sec. 2.2), the fluorescence of different hyperfine states belonging to the $m_S = 0$ manifold depends on the nuclear spin projection [85]; this enables the read out of the spin via laser excitation without need to map m_I onto m_S with the aid of MW pulses. Some examples of this effect are reported in Fig. 2.3. While for $B \simeq 200$ G we can note that all the three hyperfine levels of $m_S = 0$ manifold show the same fluorescence within the uncertainty, at $B \simeq 530$ G, i.e. close to the ESLAC, $|0,\pm1\rangle$ states exhibit a PL intensity much lower with respect to $|0,0\rangle$ and close to the level of $m_S = -1$ manifold.

2.2 Dynamic nuclear polarization mechanism

The scheme of the level structure generated from the Hamiltonian operators is represented in Fig. 1.1(a) and (b). In the presence of an externally applied

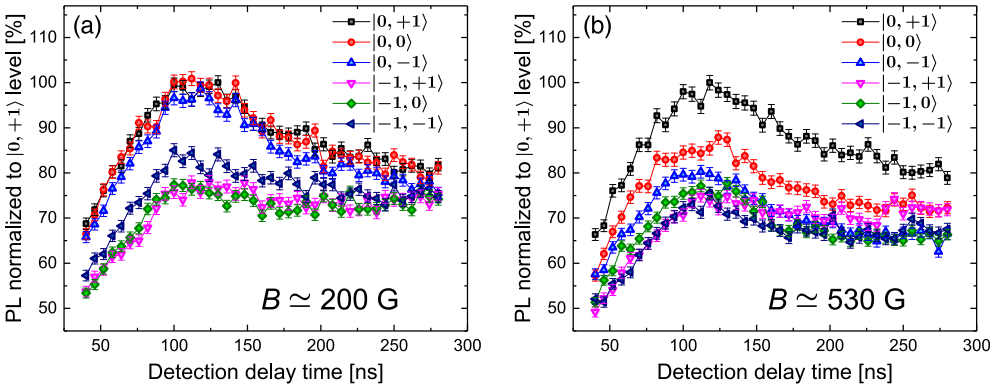

Figure 2.3: Fluorescence intensity of different hyperfine states in manifolds $m_S = 0, -1$. The PL is normalized to the $|0, +1\rangle$ maximum, as a function of detection delay time with respect to the laser pulse starting. The measurement is performed for two magnetic field $\boldsymbol{B}$, aligned with the NV symmetry axis with an angle $\leq 3°$. **(a)** Static magnetic field strength $B \simeq 200$ G. **(b)** $B \simeq 530$ G.

magnetic field $\boldsymbol{B}$, since the ES behaves as an effective orbital singlet like the GS (as explained in Sec. 1.3), the ES Hamiltonian is analogous to Eq. (1.2):

$$\mathcal{H}_e = D_e S_z^2 + \gamma_e \, \boldsymbol{S}\cdot\boldsymbol{B} + Q \, I_z^2 + \boldsymbol{S}\cdot\mathbf{C}\cdot\boldsymbol{I} + \gamma_n \, \boldsymbol{I}\cdot\boldsymbol{B}, \tag{2.4}$$

where the hyperfine interaction reads:

$$\boldsymbol{S}\cdot\mathbf{C}\cdot\boldsymbol{I} = C_\parallel S_z I_z + C_\perp (S_x I_x + S_y I_y). \tag{2.5}$$

All the previous constants already defined in Sec. 1.3 have been directly measured before this work, with the exception of $C_\perp$, and are shown in Tab. 1.2.

The transverse hyperfine coupling in the excited state is at the basis of the nuclear spin polarization process, since it leads to a mixing of the states with the same total (electronic plus nuclear) spin [81], and the eigenvectors of the system read:

$$\begin{cases} \psi_+ = \cos(\theta_+)\,|0,-1\rangle_e + \sin(\theta_+)\,|-1,0\rangle_e \\ \psi_- = \sin(\theta_-)\,|0,-1\rangle_e + \cos(\theta_-)\,|-1,0\rangle_e \\ \phi_+ = \cos(\eta_+)\,|0,0\rangle_e + \sin(\eta_+)\,|-1,1\rangle_e \\ \phi_- = \sin(\eta_-)\,|0,0\rangle_e + \cos(\eta_-)\,|-1,1\rangle_e \end{cases} \tag{2.6}$$

Again, here we used the notation $|m_S, m_I\rangle_e = |m_S\rangle_e \otimes |m_I\rangle_e$ to indicate the unperturbed hyperfine levels of the ES, in the absence of couplings and transverse magnetic fields. We note that $m_S = +1$ manifold of ES is not

involved in this process because of the high difference in energy due to the different sign of Zeeman interaction.

The mixing parameters $\theta_{\pm}$ and $\eta_{\pm}$ can be written as:

$$\begin{aligned}\theta_{\pm} &= \tan^{-1}\left[\frac{-2C_{\perp}}{(D_e-\gamma_e B-C_{\perp})\pm\sqrt{(D_e-\gamma_e B-C_{\perp})^2+4C_{\perp}^2}}\right]\\ \eta_{\pm} &= \tan^{-1}\left[\frac{-2C_{\perp}}{(D_e-\gamma_e B+C_{\perp})\pm\sqrt{(D_e-\gamma_e B+C_{\perp})^2+4C_{\perp}^2}}\right]\end{aligned} \tag{2.7}$$

The conditions for the maximum mixing are simply:

$$\begin{cases}\theta_+ = \theta_- \Rightarrow B = \frac{D_e-C_{\perp}}{\gamma_e}\\ \eta_+ = \eta_- \Rightarrow B = \frac{D_e+C_{\perp}}{\gamma_e}\end{cases} \tag{2.8}$$

Since $D_e \gg C_{\perp}$, both mixings become relevant (i.e. $\tan\theta_{\pm}\sim\tan\eta_{\pm}\sim 1$) near the level anticrossing in the excited state, where $D_e-\gamma_e B=0$, as illustrated in Fig. 2.4. Then, energy-conserving exchange of polarization by spin flip-flop can occur, that, when combined with a continuous cycle of optical excitation and non-radiative decay, leads to a polarization of both the electronic and the nuclear spins.

The relative population of the hyperfine levels of the ground-state achieved after long optical pumping depends *(i)* on the magnetic field strength and orientation with respect to the NV symmetry axis, and *(ii)* on the decay rates of the optical transitions between the spin states (spontaneous emission and intersystem crossing). On the other hand, the temporal dynamics of the nuclear polarization strongly depends on the rate of the flip-flop process, that is, on the transverse hyperfine interaction in the excited state. In the next section I present a characterization of the temporal dynamics of the population of the hyperfine levels in the ground-state of a single NV center, both in experiment and with a theoretical model. Since the characteristic timescale of the population (*resp.*, depletion) of the state $|0,+1\rangle_g$ (*resp.*, $|0,0\rangle_g$) crucially depends on the excited-state transverse hyperfine interaction, we determine, in Sec. 2.6, the excited-state coupling constant $C_{\perp}$.

2.3 DNP measurement

Two different NV centers, denoted as NV1 and NV2, were chosen since they are free from proximal ^{13}C. Typical working conditions were with magnetic fields ranging from 200 G to 420 G, and with a controlled orientation with

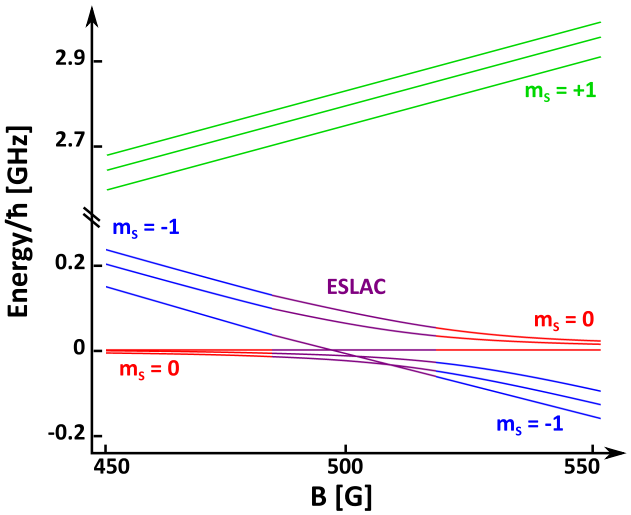

Figure 2.4: Sketch of the hyperfine energy levels of the excited state, close to the excited-state level anti-crossing.

respect to the defect symmetry axis. Thus, optical illumination induces polarization of the nuclear spin with variable efficiency due to the changing proximity to the ESLAC.

At a given magnetic field, we measured the relative population of the hyperfine sublevels of the ground-state electronic spin triplet by performing Ramsey experiments. The typical microwave $\pi/2$ pulse that drives the electronic spin lasts 25-50 ns, with a corresponding Rabi frequency large enough to simultaneously excite all the three transitions separated by the 2.16 MHz hyperfine interaction [2]. Due to the high frequency to be probed compared to $1/T_2^* \sim 0.2$-0.3 MHz, Ramsey experiments provided high resolution and signal-to-noise ratio.

Within each spin resonance, the intensities of the different hyperfine transitions give information on the ground state manifold populations (see Fig. 2.5 (b) and (c)). We extract the relative probability of the nuclear spin projection m_I as:

$$P_i = \frac{I(\nu_i)}{\sum_j I(\nu_j)}, \tag{2.9}$$

where $I(\nu_j)$ is the integral of the Fourier component of the Ramsey signal with frequency ν_j ($j = 0, \pm 1$).

In order to investigate the temporal dynamics of the polarization process, we prepare the system in a mixed state in the lowest-energy electronic level,

[2] The Rabi frequency varies at different driving frequencies, as set by the magnetic field, due to variation in the transmission of the wire used to drive the spins.

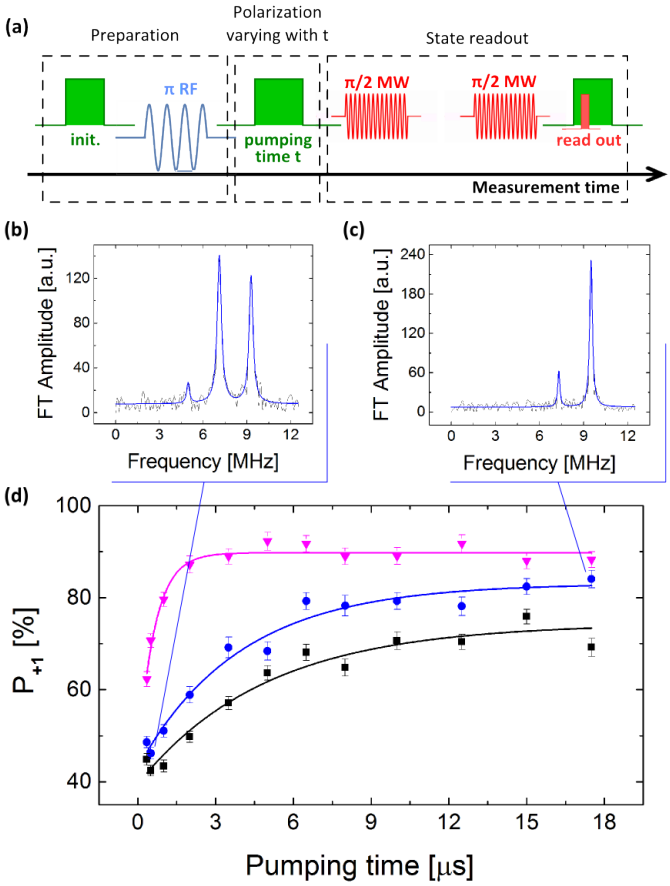

Figure 2.5: Experimental measurement for dynamical nuclear polarization. **(a)** Measurement sequence: After an initialization laser pulse, a RF π pulse resonant with the $|0,+1\rangle_g \rightarrow |0,0\rangle_g$ transition reverses the two populations; a pumping laser pulse with variable time t re-polarizes the nuclear spin; a Ramsey spectroscopy measurements on the electronic transition $|0,m_I\rangle_g \rightarrow |-1,m_I\rangle_g$ evaluates the polarized fraction of the three hyperfine levels. **(b)** and **(c)** Fourier transform of Ramsey measurements for the color center denoted as NV1 at $B = 348$ G for pumping time $t = 0.5$ μs and 17.5 μs, respectively; blue lines are Lorentzian fits. **(d)** Polarized fraction P_{+1} of the nuclear spin as a function of optical pumping time t, obtained from the Ramsey spectra. Black, blue and magenta points corresponds to $(252G, 1.7°)$, $(348G, 1.5°)$ and $(411G, 0.8°)$; the three lines are fit performed with an exponential function $P_{+1} = P_0 - A\,e^{-t/\tau}$.

and then we follow the behavior of polarization under optical illumination of variable time duration at the saturation power (see Fig. 2.5 (a)). For the preparation, first a 20 μs-long optical excitation partially polarizes the NV-^{14}N system, driving it into an unbalanced mixed state $\alpha_{-1}|0,-1\rangle\langle 0,-1|_g +$

$\alpha_0|0,0\rangle\langle 0,0|_g + \alpha_1|0,1\rangle\langle 0,1|_g$, where $\alpha_1 \sim 1$ for fields close to the ESLAC, and α_i depend on the magnitude B of the external magnetic field and on the angle θ with the NV axis. Then, a radiofrequency π pulse ($t_\pi \sim 30$ μs) on resonance with the $|0,+1\rangle_g \leftrightarrow |0,0\rangle_g$ coherently reverses the population of nuclear spin projections $m_I = 0, +1$ and alters polarization. To reveal the polarization dynamics, we use an optical pulse of variable length t, and probe the resulting population of the hyperfine levels with the Ramsey experiment explained in Sec. 1.5.2.

We characterized the polarization dynamics for different values of the magnitude and different orientations of the magnetic field. The method used for calibrating magnitude and orientation of the the magnetic field is described in Sec. 2.5. The polarized fraction P_{+1} is reported in Fig. 2.5 (d) as a function of the optical pumping time t for $(B, \theta) = (252$ G, $1.7°)$, (348 G, 1.5°) and (411 G, 0.8°). We observe that P_{+1} increases in time until reaching its final value, with variable time-constant ranging from 1 to 5 μs. This saturation level corresponds to the equilibrium condition between the two competing processes: Flip-flop between electronic and nuclear spin and optical spin pumping.

2.4 Numerical model

We compare the experimental results with simulations obtained by modelling the time evolution of the two-spin state with the Master equations in the Lindblad form [86, 87]. In turns, this allow us to determined the unknown parameters in the model.

The time evolution is dictated by the ground-state and excited-state Hamiltonians (H_g and H_e, which generate a coherent dynamics) as well as Markovian processes associated with coupling to photons and phonons, that induce transitions between different spin and orbit configurations, such as laser excitation, spontaneous and stimulated emissions, as well as intersystem crossing.

The two-spin system is described by the density operator ρ consisting of hyperfine states given by the direct product of the two sub-spaces $|m_S\rangle \otimes |m_I\rangle$, with dimensions $\dim[|m_S\rangle] = \dim[|m_I\rangle] = 3$ in the ground and excited states, whereas in the metastable singlet state $\dim[|m_S\rangle] = 1$. The resulting space of ρ is therefore given by 21 states. The population of the hyperfine sublevels of the ground state and the polarized fraction are calculated from the diagonal elements of the density matrix.

The time evolution of ρ is described by the generalized Liouville equation:

$$\frac{d}{dt}\rho = -\frac{i}{\hbar}[\mathbf{H}, \rho] + \hat{L}[\rho], \tag{2.10}$$

with $\mathbf{H}$ the total spin Hamiltonian of ground and excited states. This master equation allows us to go beyond a simple rate equation model, and fully account for the effects of transverse fields as well as coherent spin polarization exchange. The Lindbald operator $\hat{L}$ in the second term on the right is related to jumps L_k between different spin states through the equation [84]:

$$\hat{L}[\rho] = \sum_{k=1}^{N} \left(L_k \rho(t) L_k^\dagger - \frac{1}{2} L_k^\dagger L_k \rho(t) - \frac{1}{2} \rho L_k^\dagger L_k \right). \tag{2.11}$$

Most generally, we can write the jump operators as $L_k = \sqrt{\Gamma_{mn}}\,|m\rangle\langle n|$, with Γ_{mn} the rate of the transition between $|m\rangle$ and $|n\rangle$. We consider spin-conserving radiative transitions and the decay from the excited states to the ground through the metastable $S = 0$ level. We also introduce the contribution of spin non-conserving radiative processes, the rate of which we evaluated as $\epsilon = 0.01$ of the rate of spin conserving transitions [52]. All the rates related to these transitions are reported in Table 1.1. Note that these parameters have been independently measured before, from the dynamics of the NV center electronic spin alone [51–53]. In order to reproduce the measured polarization evolution at saturation, and extract the strength of the transverse hyperfine coupling from the comparison between theory and data, we set the optical pumping rate equal to the corresponding radiative relaxation rate.

The only experimentally unknown parameter in our model is then the transverse coupling $C_\perp$, that influences the rate of the flip-flop process and therefore determines the DNP dynamics.

With these mathematical tools, we performed numerical simulations in different temporal regimes of the optical pumping, investigating both the transient behavior for short time durations, and the stationary case. We first find, both experimentally and in simulations, that long optical pumping leads to a maximum constant polarized fraction, which depends on the magnetic field amplitude and its orientation with respect to the NV axis, as I discuss in Sec. 2.5. I underline that in our model we neglect the NV ionization process during optical illumination, which gives a small correction to the calculation, as shown in Sec. 2.4.1.

Finally, we need to note that the excitation rate from the ground to the excited levels, set by the laser power, plays a fundamental role in the time evolution of the population of the hyperfine sublevels of the GS, as I point

out in Appendix A. Therefore, I stress that all the experiments discussed in Sec. 2.6, and used to extract the strength of the transverse hyperfine coupling, were performed by exciting the NV defect at the saturation power; consequently, simulations were conducted setting the optical pumping rate to be equal to the corresponding relaxation rate, in order to reproduce the measured time evolution of the hyperfine sublevels.

2.4.1 Effects of charge-state conversion dynamics

The negatively charged NV center can undergo ionization (charge-state conversion to NV^0) during the 532 nm laser excitation. The ionization-deionization process has been studied under various conditions of laser wavelength and power [88–90], with rates, related to the excitation powers, varying between kHz [91,92] and MHz [93]. The NV^--NV^0 transitions during the polarization laser pulse can reduce the efficiency of the nuclear polarization mechanism and slow down its dynamics. To investigate the contribution of these effects on our estimate of $C_\perp$, we added in our simulations a simple model of the transitions involving the NV^0 state. The ionization process can only occur from the NV^- excited states, and the NV^0 state then decays to the NV^- ground state [91]; we assumed that these transitions are nuclear-spin conserving [94] and have nuclear-spin-independent rates.

We characterize the nuclear polarization time τ_{+1} as a function of the magnetic field strength for different ionization-recombination rates Γ_I. The results of the simulations are shown in Fig. 2.6. We observe that τ_{+1} increases with Γ_I, more markedly at relatively low magnetic field ($B \sim 100 - 200$ G) than close to the ESLAC, and saturates for $\Gamma_I \gtrsim 10$ MHz. Even for large ionization rate, $\Gamma_I = 10$ MHz, we verified that the estimated $C_\perp$ values are compatible with our evaluations in the absence of ionization, given our estimate uncertainty. At saturation power, we can assume Γ_I to be on the order of 1 MHz, implying a correction of $\sim 5\%$ of our estimate of the transverse hyperfine coupling, smaller than our experimental uncertainty, as we will see in Sec. 2.6. Finally, we note that if the ionization process had a larger effect, we would see a more pronounced effect at lower fields, where the polarization times were much longer than at higher field. This would have lead to a variation of the estimated $C_\perp$ with the magnetic field strength, which is instead absent, as shown in Fig. 2.9(c).

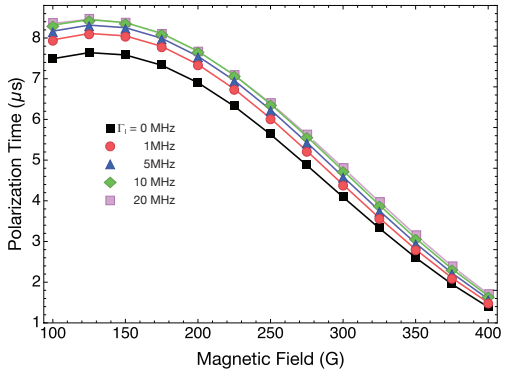

Figure 2.6: Characteristic rise-time τ_{+1} of the nuclear polarization process for different ionization-recombination rates Γ_I. τ_{+1} is shown as a function of the magnetic field strength for $\Gamma_I = 0$ (black squares), 1 (red circles), 5 (blue triangles), 10 (green diamonds), and 20 MHz (pink, light squares).

2.5 Steady-state nuclear spin population

Here, we show that the dependence of the asymptotic (long-time) nuclear spin populations on the magnetic field provides a precise method to calibrate the magnitude B of the local magnetic field at the NV position, and the angle θ between the magnetic field and the symmetry axis of the system.

To first obtain a rough calibration we use a method that relies only on the electronic spin, measuring the resonance frequencies $\nu_\pm$ of the two ground-state spin transitions $m_S = 0 \rightarrow \pm 1$, which are univocally determined by B and θ.

In the presence of the magnetic field $\boldsymbol{B}$, and excluding for now hyperfine spin Hamiltonian for sake of simplicity, the ground-state Hamiltonian of the NV electronic spin $S = 1$ can be written as:

$$\mathcal{H}_g = \gamma_e \, \boldsymbol{S}\cdot\boldsymbol{B} + D_g S_z^2 = \gamma_e \left(S_z B_z + S_x B_x\right) + D_g S_z^2, \tag{2.12}$$

where S_x, S_z are the orthogonal and parallel spin operators, respectively, and we remind that $D_g = 2.87$ GHz is the fine structure splitting. Thus, in analogy with Eq. (2.2) and (2.3), the eigenvalues of the Hamiltonian can be found as the solutions of the following characteristic equation

$$\lambda^3 - 2D_g\lambda^2 + (D_g^2 - (\gamma_e B)^2)\lambda + \frac{D_g}{2}(\gamma_e B)^2\left(1 - \cos(2\theta)\right) = 0 \tag{2.13}$$

and depend on B and θ. Note that the introduction of the nuclear quadrupole term and the parallel hyperfine interaction would just shift the hyperfine energy levels without changing the dependence from magnetic field strength

and angle and can therefore be included in the model; the transverse coupling with the ^{14}N nucleus gives very small corrections and could be neglect, as we discussed in Sec. 2.1.

For the measurements related to this chapter, we worked at local magnetic fields well-aligned with the NV symmetry axis, and far away from ground-state level-anticrossing (GSLAC) occurring at around $B \sim 1025$ G, so that the eigenvalues correspond to well defined electronic spin projections $m_S = 0, \pm 1$. We directly evaluated the zero-field splitting D_g with a magnetic resonance experiment in the absence of any external static magnetic field, and measure the two frequencies $\nu_\pm(B, \theta)$ of the transitions $m_S = 0 \rightarrow \pm 1$ of the NV in the local magnetic field via Ramsey spectroscopy. Then, we obtain a set of two equations $\nu_\pm(B, \theta) = (E_{\pm 1}(B, \theta) - E_0(B, \theta))/h$, where $E_{0,\pm 1}$ are the eigenvalues of the ground-state Hamiltonian. These equations can be solved with respect to the two unknown parameters B and θ. Because of uncertainty in the measured D_g value, as well as the measured frequencies, the estimate of the magnetic field angle θ is not accurate enough.

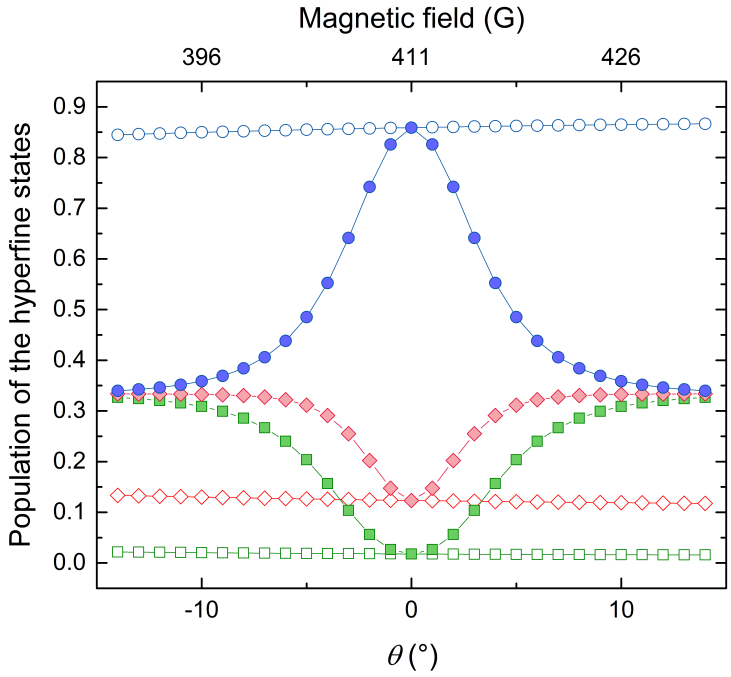

Figure 2.7: Steady-state population of the nuclear spin projections $m_I = 0, \pm 1$. Simulations are performed in presence of a magnetic field as a function of the orientation angle θ with fixed magnitude $B = 411$ G (solid symbols: $m_I = +1$ blue dots, $m_I = 0$ red diamonds, $m_I = -1$ green squares), and as a function of the magnitude B in the range $B = 390 - 432$ G for $\theta = 0°$ (empty symbols, same color code).

Thus, we also extract an independent estimate of the orientation angle θ of the local magnetic field, by measuring the steady-state populations $P_{0,+1}$ of the nuclear spin projections $m_I = 0, +1$ of the spin state $m_S = 0$. The solution of the generalized Liouville equation has shown us that the short-time dynamics of the hyperfine populations is governed by the excited-state transverse hyperfine coupling $C_\perp$, as discussed in Sec. 2.6, whereas the steady-state populations $P^\infty_{0,+1}$ at long-polarization time is unaffected by $C_\perp$, as shown in Fig. 2.9 (a). The steady-state populations $P^\infty_{0,+1}$ is found instead to strongly depend on the angle θ, and less crucially on the magnitude of the field B, within our typical experimental uncertainty on the order of few %, as exemplified in Fig. 2.7.

For any given B and θ, we evaluate the characteristic rise-time τ (*resp.*, depletion time) of $P_1(t)$ (*resp.*, $P_0(t)$). The time average of $P_{0,+1}(t)$ for $t > 5\tau$ is used to estimate $P^\infty_{0,+1}$.

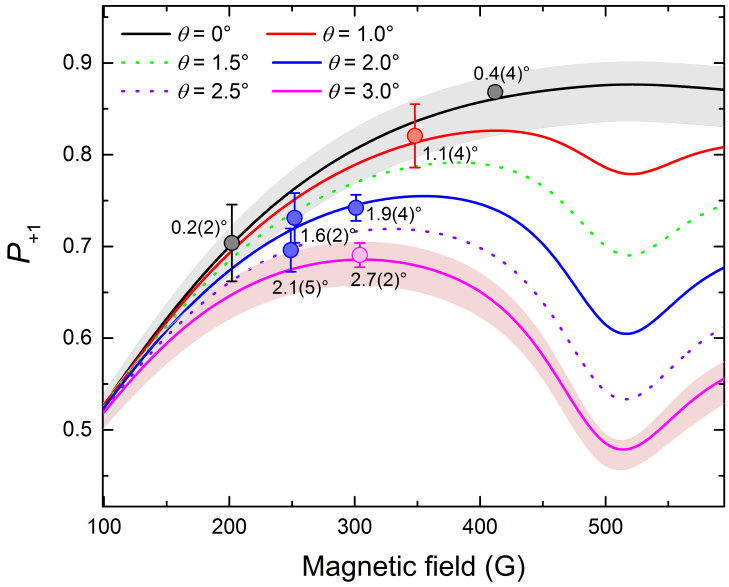

Figure 2.8: Steady-state population P_{+1} of the hyperfine state $|0, +1\rangle_g$, as a function of the modulus of the magnetic field, B, for different angles θ with respect to the NV axis. The curves are numerical solutions of the generalized Liouville equation ($\theta = 0.0°, 1.0°, 1.5°, 2.0°, 2.5°$, and $3.0°$). For the $\theta = 0°, 3°$ lines, the shaded area represents the error due to the uncertainty in the decay rates reported in Table 1.1 (we expect similar uncertainties for the other angles). Circles are experimental results, with color code and labels indicating the field orientation θ.

Comparing the asymptotic polarization obtained from simulation and from experiments allowed us to verify the validity of our model. We note

that our model reproduces very well the experimental findings at small angles ($\theta < 3°$), as shown in Fig. 2.8. For larger angles the observed polarization is lower than expected; this deviation could be attributed to other spin decoherence processes in the excited state that reduce the effective interaction time available for the polarization exchange [36]. Although in our model we did not include these processes, such as the excited state electronic spin dephasing, we verified that they do not have a significant influence on the dynamics at small angles. Therefore, the theoretical steady-state populations $P^{\infty}_{0,+1}(B,\theta)$ is fitted to the experimental data, with the angle θ as the only free parameter of the fit, by minimizing the mean squared residuals χ^2 between data and theoretical curves.

With this method, we extracted a second refined estimate of the angle θ, which we found to be consistent with (but more accurate than) the value estimated from the frequencies of ground-state spin transitions. We use this refined estimate of the angle as an input in further calculations of the polarization dynamics.

2.6 Excited-state transverse hyperfine coupling evaluation

Although the spin structures of both the ground [49, 57, 58, 80, 95, 96] and excited [57, 60, 97] triplet states have been characterized in experiments, the transverse hyperfine coupling between electronic and nuclear spin is in general difficult to measure. In particular, the excited state transverse hyperfine coupling strength has been inferred by assuming an isotropic interaction [57, 60], although *ab initio* calculations indicate an anisotropy of the hyperfine tensor for the ^{15}N isotope [36].

Once defined and verified the model that can reproduce well the behavior of the nuclear spin polarization for long polarization times, we investigate the dynamics of the process and its characteristic times. We now discuss the time-evolution the population of the $|0,+1\rangle_g$ and $|0,0\rangle_g$ states as a function of the interaction between the optical excitation and the NV system.

For various experimental conditions, B and θ, we performed simulations of the time-evolution of the state probability as a function of $C_\perp$, which is the only free parameter in the master equation Eq. (2.10). This was done for both the $|0,+1\rangle_g$ and the $|0,0\rangle_g$ spin components. The $|0,-1\rangle_g$ was excluded because in most cases the amplitude of its Ramsey component is very small and comparable with our signal to noise ratio.

In Fig. 2.9 (a) we report the relative probability of the states $m_I = 0, \pm 1$

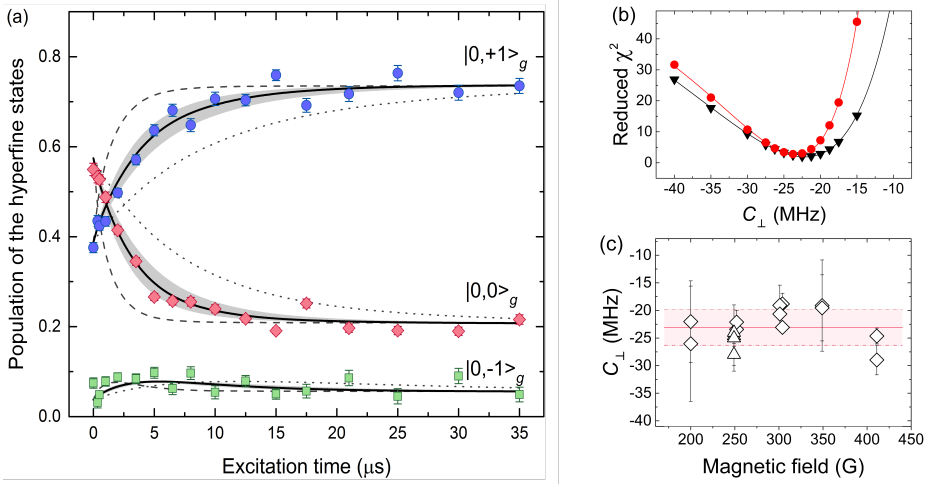

Figure 2.9: Dynamical nuclear polarization analysis. **(a)** Comparison between experimental data and calculation of the relative population of the states $|0,-1\rangle_g$, $|0,0\rangle_g$ and $|0,+1\rangle_g$ after optical pumping of variable length t. Blue dots, red diamonds, and green squares correspond to $m_I = +1, 0, -1$ nuclear spin relative probability. Dotted and dashed lines are the theoretical curves for $C_\perp = -15$ MHz and -40 MHz, respectively; black line and gray region correspond to $C_\perp = (-23 \pm 3)$ MHz. **(b)** Mean squared residuals χ^2 between data and theoretical curves, as a function of the hyperfine transverse coupling $C_\perp$ at $B = 252$ G; black and red scatters refer to $m_I = +1$ and $m_I = 0$, respectively. The fit to the residuals (black and red lines) were used to find the minimum of the residual distribution and thus the best-fit estimate for $C_\perp$. **(c)** Transverse hyperfine coupling parameter of the excited state, $C_\perp$, evaluated for different values of the magnetic field. The analysis of both the $|0,+1\rangle_g$ and the $|0,0\rangle_g$ components is included, for NV1 (diamonds) and NV2 (triangles). Red straight line and shaded region denote weighted average and standard deviation of the sixteen values of (B, θ).

as a function of the optical pumping time for $B = 252$ G, compared with the theoretical calculation for $C_\perp = -15$ MHz, -23 MHz, -40 MHz. I note that the value often used in literature, $C_\perp = -40$ MHz [60,98], which derives from the assumption of isotropic interaction in the excited state, does not fit the experimental findings – neither the rise-time of the population of the $|0,+1\rangle_g$, or the-decay time of the $|0,0\rangle_g$ population.

For both $|0,+1\rangle_g$ and $|0,0\rangle_g$, from the comparison between simulations and experimental data of the DNP we calculate the normalized mean squared residuals χ^2:

$$\chi^2 = \frac{1}{N} \frac{\sum_{i=1}^{N} (P_{i_{cal}} - P_{i_{exp}})^2}{\sum_{i=1}^{N} \Delta P_{i_{exp}}^2}, \tag{2.14}$$

where N is the number of each measurement related to a given optical pumping time; $P_{i_{cal}}$, $P_{i_{exp}}$ and $\Delta P_{i_{exp}}$ are the calculated polarized fraction for the pumping time i, the experimental value and its associated error. In order to extract the minimum $C_{\perp_{min}}$ in the residual distribution we built an empirical function:

$$\chi^2 = \chi^2_{min} + \mathrm{A}\left[\left(\frac{b}{C_\perp - C_{\perp_0}}\right)^{12} - 2\left(\frac{b}{C_\perp - C_{\perp_0}}\right)^{6}\right], \tag{2.15}$$

where χ^2_{min} represents the minimum value of χ^2 and A is an amplitude parameter; from the derivative of 2.15 we directly extract $C_{\perp_{min}}$ as:

$$C_{\perp_{min}} = C_{\perp_0} - b. \tag{2.16}$$

By averaging $C_{\perp_{min}}$ over the two nuclear spin components and over the different experimental magnetic field magnitudes and orientations (Fig. 2.9 (c)), we obtain a precise estimate of the transverse hyperfine coupling, $C_\perp = (-23 \pm 3)$ MHz. This is the first experimental measurement of the transverse hyperfine coupling in the excited-state of the NV center, obtained with simple magnetic resonance tools [83]. The common assumption $C_\perp \approx C_\parallel$, which can be more easily measured, is not consistent with the present experimental observation of the timescale of the nuclear polarization.

Our result does not depend on the specific NV, and is representative of NVs in low concentration bulk diamond. Our findings can be useful in NMR experiments enhanced by DNP, hyperpolarization of nuclear spin ensembles, and in all the protocols involving fast and accurate control of nuclear spins, which are crucial for many applications in quantum technologies, including quantum computation, communication and sensing.

Chapter 3

Optimal control of NV electronic spin for quantum sensing

As already discussed in the Introduction, quantum control has been demonstrated to be a crucial tool both in quantum information processing [15] and in quantum sensing [4,7] on a variety of experimental platforms, ranging from trapped ions [99] to ultracold atoms [100] and superconducting qubits [101, 102], as well as nuclear [103, 104] and electronic spin qubits [78, 105]. Quantum sensing poses peculiar challenges to control, as sensor qubits need to interact strongly with the target field to be probed, but this also leads to undesired coupling with external noise of the same nature of the target field, which often gives rise to either energy losses or decoherence. A paradigmatic scenario is when one wants to measure a frequency shift of a spin qubit sensor, as due to a magnetic field, in the presence of magnetic dephasing noise.

Optimal control theory [106, 107] exploits numerical optimization methods [108–112], to find the best control fields that steer the dynamics of a system towards the desired goal. Quantum optimal control has been successfully applied in the case of one- and few-body systems [113–118], as well as in ensembles [119] and correlated many-body quantum systems [100, 120, 121].

Typically, the optimal control problem involves the search for the optimal transformation that, given a system Hamiltonian H dependent on a set of time-dependent control fields, drives the system from an initial state into a target state, whose desired properties are expressed by a cost function that one wants to minimize. Often this means maximizing the fidelity of the unitary operation, which describes this transformation, with the desired one.

However, the goal of quantum sensing is different. Since there is at most only some partial knowledge of the external field to be measured, the expected unitary dynamics is unknown, and thus the fidelity cannot be used to optimize control. In addition, quantum sensing is usually concerned with

optimizing sensitivity, a quantity that intrinsically includes noise, also arising from the external environment.

In this Chapter, I present our work [122] on how we adapted optimal control theory to the quantum-sensing scenario by introducing a cost function that, unlike the usual fidelity of operation, correctly takes into account both the field to be measured and the environmental noise. We experimentally implemented this novel control paradigm using a NV center, finding improved sensitivity to a broad set of time-varying fields. The demonstrated robustness and efficiency of the numerical optimization, as well as the sensitivity advantage it bestows, will prove beneficial to many quantum-sensing applications.

In Sec. 3.1, I describe a robust and efficient scheme devised for optimal control of a sensing qubit, which enhances its sensitivity to the amplitude of time-varying target fields. For this purpose, we use an unconventional optimization metric, the sensitivity, and develop a practical way of computing it (which allows for fast numerical searches). Furthermore, our search method includes, in the cost metric itself, the presence of an environment and the consequent decoherence induced on the qubit. While optimal control has been used before for sensing [123–125], the optimization was only targeted at improving the control fidelity and bandwidth, not the sensitivity itself. Sec. 3.2 is dedicated to the methods to obtain the theoretical optimization of the sensitivity and the experimental observable to compare with.

Afterwards, I analyze the different variable magnetic fields considered as exemplary cases for the application of our initialization protocol. In Sec. 3.3 I start considering the simple case of a monochromatic cosinusoidal field and the optimization of a small space of parameters, the total and the starting times of the measurement routine. Then, I tackle the complex task of measuring multichromatic variable (AC) target fields, engineering the design of non-equidistant multipulse sequences, enabling to simultaneously collect signal from all the various frequency components; moreover, we demonstrated the effectiveness of the method by investigating different frequency ranges.

In Sec. 3.4 I discuss sensing of different significant waveforms, such as trains of magnetic impulses, which are relevant for applications in biology, physiology, and neuroscience [27, 126–128]. We show that, in these cases, optimal control demonstrates better performance than traditional dynamical decoupling since it allows for both a larger accumulation of the spin phase that encodes the field information and for an improved compensation of environment-induced decoherence, thus boosting the qubit's sensitivity and enabling detection of very weak magnetic fields. Finally, Sec. 3.5 summarizes the main results and provides an outlook of our new optimal control strategy.

3.1 Optimal control of a qubit sensor with dephasing noise.

In this section I address the topic related to the measurement of time-varying magnetic fields in the presence of magnetic noise, which induces dephasing of the sensing qubit, using the electron spin states of an NV center. All the experiments discussed in this chapter have been performed on a single negatively charged NV center, located at ~ 13.5 μm below the diamond surface. A static bias magnetic field $B = 39.4$ mT, aligned along the symmetry axis of the NV center, removes the degeneracy of levels with spin projection $m_z = \pm 1$, and the microwave excitation selectively addresses the $|0\rangle \rightarrow |-1\rangle$ transition; therefore, the NV center can be effectively described as a single two-level system [1].

The spin qubit couples both with a time-dependent external field to be measured and with environmental magnetic noise. We model those couplings extending the Hamiltonian in Eq. (1.8):

$$H = H_{field} + H_{int} = \gamma_e \, b(t) S_z + \gamma_e \, \beta(t) S_z, \tag{3.1}$$

where the field to be measured has the general form

$$b(t) = b \, f(t), \tag{3.2}$$

and $\beta(t)$ is a stochastic variable with power spectral density $S(\omega)$ in the frequency domain. $\gamma_e = 2.80 \times 10^4$ Hz/μT and S_z are again the gyromagnetic ratio and the z component of the spin operator. Performing metrology means reaching a compromise between two conflicting tasks, i.e., minimizing the noise effects while maximizing the signal stemming from the field, during the sensing time. In particular, we assume to know the temporal dependence $f(t)$ of the field, aiming at measuring its amplitude b (beeing thus interested in a parameter estimation task). I note that by embedding our scheme in an adaptive strategy, it would be also possible to tackle waveforms of unknown time dependency [129].

While different control strategies can be used for sensing, here we consider control via pulsed dynamical decoupling. We limit the notion of "optimal" control to optimality over this restricted choice of control strategies. The support in this choice of strategy derives by the great success that dynamical decoupling has obtained in quantum sensing. Even if allowing general

[1] Here I neglect the hyperfine coupling of the NV electronic spin to nearby nuclear spins since, in the presence of a static bias magnetic field close to 40 mT, we observe full polarization of the nuclear spin of the ^{14}N composing the NV center (as discussed in Ch. 2)

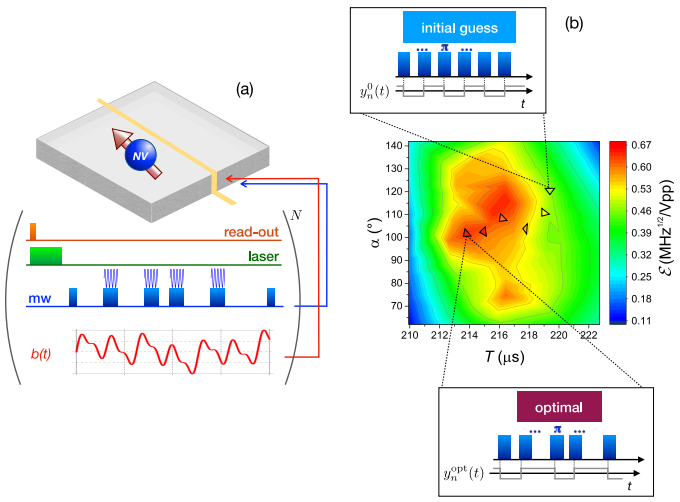

Figure 3.1: One-qubit optimization strategy. **(a)** The electronic spin of a single NV center is optically initialized in the $|0\rangle$ state, and read out after the sensing period. The antenna delivers both the resonant control field (MW) (see also Sec. 1.4) and the target magnetic field $b(t)$ to be measured, in the proximity of the spin qubit. Each measurement shot is repeated $N = 2 \times 10^5$ times. **(b)** Illustration of the optimization protocol. The starting point is an initial guess for the control sequence described by a modulation function $y_n^0(t)$, which depends on a given number of parameters. While in Sec. 3.3 and 3.4 I consider more general cases, for the sake of simplicity the central panel shows a search in a two-parameter space (sensing time T and phase shift α) for CPMG control sequence used to detect a monochromatic AC field $b(t) = b\cos(2\pi\nu_0 t + \alpha)$, with frequency $\nu_0 = 20.5$ kHz, and unknown amplitude b to be measured. The map represents the experimentally measured inverse sensitivity $\mathcal{E} = C/\eta$ (see Sec. 3.2). The algorithm computes the sensitivity η under the initial control sequence and then produces and evaluates a number of other trial points $y_n^{(i)}(t)$ and moves in the multidimensional parameter space until global convergence is reached. The final point, described by $y_n^{\rm opt}$, represents the optimal control sequence.

control fields could lead to a true optimal solution, it would also complicate the search space and its computational cost. Nevertheless, while we do not demonstrate the realization of the ultimate limit of sensitivity, that is, the Quantum Cramér-Rao bound [130] (discussed in Sec. 3.1.1), our optimal control method remarkably enhances sensitivity in a number relevant and demanding experimental scenarios.

The phase $\varphi_n(T)$ accumulated by the spin during the sensing time T,

under the action of the control field, is

$$\varphi_n(T) = \int_0^T \gamma\, b(t)\, y_n(t) dt \equiv b\, \phi_n. \tag{3.3}$$

The Ramsey interferometer, that hold the control sequence, enables the mapping of the phase accumulated around the $\hat{z}$ axis into the observable population of the spin projection $m_S = -1$. In this way, it allows us to read out the effect due to the target field.

As said, during the sensing process, the sensor qubit is also subject to noise. In the case of the NV center, as introduced in Sec. 1.6 and discussed in Ch. 4, this is mainly due to the nuclear spin bath that generates a stochastic time-varying field, which leads to a reduction of the observed population.

The state of the qubit after the sensing process is described, as in a Ramsey interferometer, by population and coherence of the density matrix

$$\rho_{1,1}(T) = \frac{1}{2}, \quad \rho_{1,2}(T, b) = \frac{1}{2} e^{-i\varphi_n(T)} e^{-\chi_n(T)}, \tag{3.4}$$

with the temporal coherence function $\chi_n(T)$ defined in Eq. (4.1). Thus, a projective measurement on the σ_x basis, $|\pm\rangle = (|0\rangle \pm |-1\rangle)/\sqrt{2}$ gives a signal

$$p_n(T) = \langle + |\, \rho(T, b)\, | + \rangle = \frac{1}{2} \left(1 + e^{-\chi_n(T)} \cos \varphi_n(T)\right). \tag{3.5}$$

I point out that here we treat the environment as a source of pure decoherence noise and further assume a classical bath described by its spectrum $S(\omega)$, as this allows the simple expression in Eq. (4.1) to describe its effects [64, 131] (see Sec. 3.1.2 for further discussion of this approximation validity). While a classical bath is a good model for many physical systems [132–137], the same formalism can tackle more complex and quantum baths [72, 138]. More generally, using Eq. (4.1) to calculate the environmental effects on the sensor only simplifies the numerical optimization, but a more complex noise model could also be taken into account.

3.1.1 The sensor sensitivity

As already mentioned in the Introduction, the quality of the quantum sensor is crucially described by its sensitivity. The latter is defined as the minimum measurable signal for an integration time of 1 s. The minimum signal is limited by the signal-to-noise ratio (SNR) achieved with the measurement. In the present case, the signal is nothing else than the probability p_n. With noise we indicate here the total uncertainty given by the sum of all the possible error sources. A first contribution to the error is given by the quantum

projection noise. As we discussed, to measure p_n we need to collect a statistics, since each repetition gives only a binary value, so we have to repeat the procedure N times in order to extract the real value of p_n. The associated error would be equal to 0 for an infinite number of measurements, up to 0.5 for $N = 1$ and in general it scales as $1/\sqrt{N}$. Another cause of uncertainty is the classical readout noise due to the fraction of measurement that are erroneously assigned to $|0\rangle$ or $|1\rangle$ with respect to the total number of measurements. If the classical read out noise is small with respect to the quantum projection noise, the overlap of the measurement distributions with results 1 and 0 is small. In the opposite case, classical readout noise much bigger than the quantum projection one, it is possible to obtain just a single distribution of measured values over the N repetitions. Its variance can be expressed by the ratio between the distribution variance and the contrast of the binary measurement (i.e. difference between observed values for measuring 0 or 1) and goes like $1/N$.

To evaluate the denominator of the SNR, the total error is the sum of readout noise and quantum projection error. A different argument has to be done for decoherence and errors due to initialization and qubit manipulations, since they directly affect the amplitude of the measurable p_n. Indeed, they reduce the dynamical range of p_n, i.e. the possible values that it could achieve, limiting the numerator of the SNR. Summarizing, a signal correspondent to a SNR equal to one (i.e. the minimum measurable signal) achieved with a measurement integration time of 1 s is the experimental sensitivity.

Up to now, we just provided an operational definition, but the ultimate limit for the intrinsic sensitivity is more rigorously identified by the (quantum) Cramér-Rao bound (CRB). The latter states that the lower bound for any unbiased estimator obtained with a positive operator-valued measure (POVM) is proportional to the inverse of the Fisher information (FI) [139]. In other words, maximizing the information obtained on the quantum system through the measurement, we obtain the minimum uncertainty on the observable. Considering to maximize the Fisher information over all the possible POVM, we would obtain the quantum FI and the quantum CRB. Integrating this limit over a measurement time of 1 s we define the possible minimum sensitivity achievable by a sensor.

To assess the quality of parameter estimation, as achievable under a given control protocol and within the experimental constraints, we start from the definition of F_N, the Fisher information [130, 139] associated with the measurement:

$$F_N = \sum_x \frac{1}{\mathcal{P}_N(x|b)} \left(\frac{\partial \mathcal{P}_N(x|b)}{\partial b} \right)^2 . \tag{3.6}$$

Here $\mathcal{P}_N(x|b) = \mathrm{Tr}[E_x^{(N)}\rho_b^{\otimes N}]$ are conditional probabilities of obtaining x as a measurement result for a given field b over N repeated measurements, E_x being a positive measurement estimator [2] and ρ the density matrix of each independent copy of the system.

From F_N we can extract the minimum distance between two different results of the measurement by optimizing over possible estimators for a given quantum measurement: We get the limit on the variance of any estimator for the classical distinguishability metric, known as the Cramér-Rao bound (CRB) [140]:

$$\Delta p_n \geq \frac{1}{\sqrt{NF_N}}, \tag{3.7}$$

where Δp_n represents the minimum measurable difference between two $p_n(T)$ measurements. Sensitivity, that is, the minimum detectable signal per unit time, is simply related to the CRB by

$$\eta = \frac{\sqrt{\mathbb{T}}}{\sqrt{NF_N}}, \tag{3.8}$$

where $\mathbb{T} = NT$ is the total sensing experiment time. For the one-qubit sensing schemes we are considering, putting Eq. (3.5) in Eq. (3.6)[3], η reduces to

$$\eta = \min\left\{\frac{p_n}{\partial_b p_n}\right\}\sqrt{T} = \frac{e^{\chi_n(T)}}{|\phi_n|}\sqrt{T}. \tag{3.9}$$

This is indeed the cost function that we want to minimize. In practice, for a given field $b(t)$, we are searching for the optimal control field that steers the spin trajectory of the electronic spin on the Bloch sphere in such a way that, while the accumulated phase $\varphi_n(T)$ is maximized, the effect of non-Markovian noise described by $\chi_n(T)$ is minimized.

For this purpose, we have designed a direct and fast search method that looks for the optimal modulation function $y_n^{\mathrm{opt}}(t)$ that minimizes the cost function η. We have investigated various multidimensional parameter spaces and analyzed which optimization parameters (e.g., total sensing time, π-pulse positions, signal phase, signal trigger time) provide the largest improvement without requiring excessive computational resources, as we detail in the following. The search of the optimal control field is performed by means of a simplex (Nelder Mead) minimization numerical algorithm that allows us to reach global convergence in the parameter space, as illustrated in Fig. 3.1(b).

[2] We can restrict ourselves without any concerning to consider only positive operator-valued measure (POVM), as it is for projecting measurements [15].

[3] That is, considering in the sum also the possible outcome $\langle -|\,\rho(T,b)\,|-\rangle$, meaning a sign change on the second term of the right hand side of Eq. (3.5).

The method requires a precise knowledge of the temporal coherence function of the electronic spin sensor, which depends on the noise spectrum induced by its spin bath, as I detail now.

3.1.2 Measuring the sensor noise spectrum

As expressed by Eq. (3.9), our optimal control strategy depends on knowledge of the coherence function $\chi_n(T)$. As shown in Eq. (4.1), $\chi_n(T)$ depends on both the noise spectrum and the frequency filter $Y_{n,T}(\omega)$ given by the specific sensing sequence. In order to compute the sensitivity η, the optimization algorithm calculates the value of $\chi_n(T)$ for different trial sequences; thus, it needs the noise spectral density $S(\omega)$ as an input. Various methods to measure the noise spectrum have been suggested in the literature [132,135,141–145]. In our case, although the environment exhibits a relatively abundant amount of ^{13}C nuclei, meaning a strong spin-bath coupling, for the sensitivity optimization we limited ourselves to an approximated procedure, presented in Ref. [141]. I will discuss its limitations and alternative methods for the environment characterization in Ch. 4.

Then, the coherence signal decays as $p_n(t) \sim e^{-t/T_2^{\mathrm{CP}}(\tau)}$, where $T_2^{\mathrm{CP}}(\tau)$ is a coherence time directly related to the noise spectral density via [141]

$$\frac{1}{T_2^{\mathrm{CP}}(\tau)} \simeq \frac{8}{\pi^2} S(\pi/\tau). \tag{3.10}$$

For each value of τ (which sets the noise frequency that we are considering), we measured the signal decay as a function of the number of pulses, obtaining $T_2^{\mathrm{CP}}(\tau)$. By varying the time τ between MW π pulses, we can extract the main frequency components of the noise spectral density using Eq. (3.10). The spectrum was finally obtained by fitting the raw data with a sum of Gaussian functions, as shown in Fig. 3.2(a).

In the mean peak we can recognize the known Larmor frequency for the ^{13}C bath ($\sim$ 424 kHz at 394 G). Nevertheless, the experimental spectrum $S(\omega)$ obtained for sequences with different number of pulses showed some additional peaks and variations. Thus, we further refine $S(\omega)$ by fitting the signal $s(T)$ measured after a CPMG decoupling sequence as in Ref. [146] (see, e.g., Fig. 3.2). This procedure is aimed at correcting $S(\omega)$ for sequence-dependent noise related to two different reasons, which are not taken into account in our model: The first concerns control imperfections, e.g. the finite π-pulses duration [147]. The second approximation is given by coherent couplings due to strongly interacting nearby nuclear spins, generating a signal oscillation as a function of the number of pulses (see [148–150], and Ch. 4 for further discussion); indeed, the signal $p_n(T)$ exhibits periodic collapses

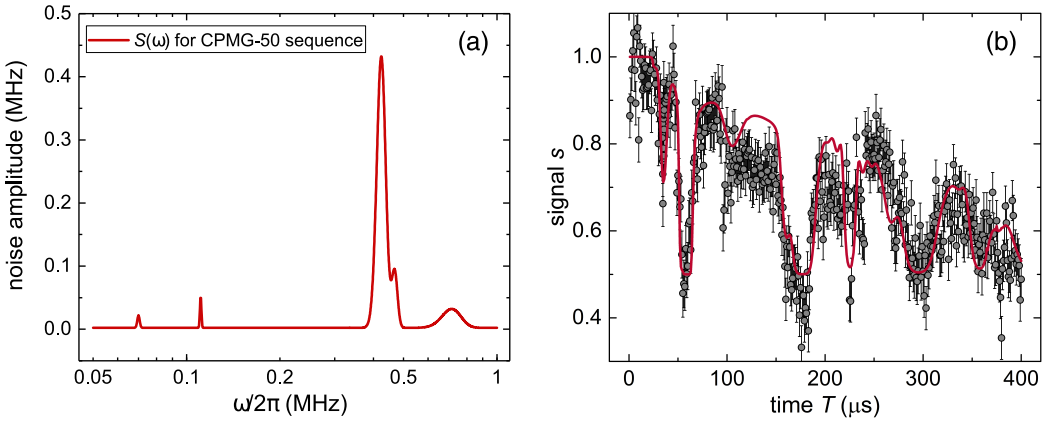

Figure 3.2: Experimental and reconstructed NV spin coherence under CPMG sequence. **(a)** Reconstructed $S(\omega)$ based on a classical model of the bath, for CPMG decoupling sequence with $n = 50$. The main component at $\sim$ 424 kHz, related to the interaction with the ^{13}C bath, is in common with all CPMG sequences. Other peaks are aimed to reproduce the effects of control imperfections and strong coupled ^{13}C nuclei (see text). **(b)** Measured signal $s(T)$ (gray dots) after a CPMG-50, as a function of time $T = n\tau$. Here, the sensor is not irradiated with any external target field $b(t)$ to be measured. The solid red line is a simulation of the signal produced with $S(\omega)$ represented in (a).

due to the nuclear spin bath, with additional dips below 0.5 (see Fig. 3.2) that are a signature of a quantum environment, more precisely, of a hyperfine interaction between the NV electronic spin and isolated nearby nuclear spins. Although the latter interactions give rise to unitary evolution of the NV, we include them in the model as classical external noise sources at fixed frequency. This approximation can be possible only once fixed the number of pulses composing the sensing sequence [4] and we chose a Gaussian lineshape as for the case of the carbon bath. This allows us to use Eq. (3.5), which does not take unitary evolutions into account but provides a speedup of the numerical optimization, with the important caveat to require corrections once changed n. We emphasize that good agreement between predicted and measured sensitivity (also for 150 μs $< T <$ 200 μs, where we see a dip below 0.5; see Fig. 3.6 and 3.5) is proof of the robustness of the model to the effects of weak couplings between NV and isolated spins, as well as to imperfections in the empirical function $\chi_n(T)$. Therefore, we finally find a noise spectrum that, for a fixed number of pulses, is completely independent of the timing at which each π pulse occurs; thus, it can be used for sequences that are

[4] Even if the characteristic frequency of this interaction does not depend on the specific measurement filter, its amplitude is strongly dependent on it, as I will detail in Sec. 4.4.

very different from CPMG in the optimization procedure. Including pure quantum noise effects in the optimization routine would be an interesting technical extension of the present method.

3.2 Optimal control simulation and experiment

The experimental procedure is sketched in Fig. 3.1(a) (see also Sec. 1.4). After the initialization in $|0\rangle$, the spin qubit is coherently controlled with a resonant field and radiated with the off-resonance, time-varying, target magnetic field to be measured. To experimentally validate the optimal control, we compare the optimized sensitivity η with the corresponding measured quantity. We obtain the sensitivity of the spin qubit to the target field by sweeping the amplitude of the magnetic field and measuring the slope of the signal $p_n(T)$, depicted in Eq. (3.5), at the points of maximum slope (where $s = 0.5$), as shown in Fig. 3.3(a).

However, since we do not have an independent measure of the local amplitude of the magnetic field at the position of the NV center, in the experiment we measure $\mathcal{E} = \max\{\partial_b p_n\}/\sqrt{T}$, where p_n is the normalized signal presented in Eq. (1.14). Following Eq. (3.9), this experimental observable is simply related to sensitivity through $\mathcal{E} = K/\eta$, where K represents a conversion factor between the generated RF field amplitude and the unknown magnetic field at the defect; as K is the only calibration constant and does not depend on the target field strength and of the control sequence, it can be evaluated once and then used for all the control scenarios considered.

In particular, we estimate K from the experimental results for CPMG sequences. We experimentally evaluate $\mathcal{E}(T)$ as a function of the sequence total time T and fit the curve to extract the maximum $\mathcal{E}_{CP_M}$. Similarly, we evaluated the theoretical value of η and obtained its minimum η_{CP_m}. We then defined K as the product $K = \mathcal{E}_{CP_M}\,\eta_{CP_m}$. This procedure allows us not only to define K but also to estimate its uncertainty ΔK, from the fit error. We can then compare the (inverse) experimental sensitivity $\mathcal{E}_i$ and the theoretical sensitivity η_i for each control sequence by rescaling the theoretical sensitivity by K.

In the following, I consider different time-varying target fields that mimic signals of interest and highlight the advantage of our optimal control method. The method can be applied over the same frequency range accessible by a non-optimized sensor, with a typical bandwidth of the sensor under pulsed control set by the pulse length and by the control-dependent decoherence time T_2 (~ 2 kHz -15 MHz).

From a theoretical point of view, the core of our optimal control technique

for sensing is an optimization algorithm that minimizes the sensitivity as a function of the parameters of the control function, e.g. total sensing time, phase of the AC field, and time intervals between π pulses.

We use a MATLAB routine based on the simplex minimization algorithm to achieve global optimization of the figure-of-merit, the sensitivity η. The two main ingredients of this quantity, represented in Eq. (3.9), are the electron spin phase $\varphi_n(T)$ and the coherence function $\chi_n(T)$. We consider pulsed control sequences described by the π-pulse times $\{t_j\}$. For any time-varying external magnetic field $b(t) = bf(t)$ to be measured, we can define the integral of the magnetic field (known) temporal profile $f(t)$

$$F(t) = \frac{1}{t}\int_0^t f(t')\,dt'. \tag{3.11}$$

The phase $\varphi_n = b\,\phi_n$ acquired by the NV qubit can then be calculated for any given control sequence as

$$\phi_n = (-1)^{n+1}F(T)T - 2\sum_{j=0}^{n+1}(-1)^j F(t_j)t_j. \tag{3.12}$$

The coherence $\chi_n(T)$ is instead obtained from the experimentally measured spectrum with the method described in Sec. 3.1.2. From $\chi_n(T)$ and $\phi_n(T)$ we can calculate η for each trial sequence according to Eq. (3.9).

In order to verify the global convergence of the optimization algorithm, we tested different initial guesses and found the same optimized parameters for a given AC target field. In most cases, we used a constrained search, by setting bounds for each parameter or constraining the overall result, for instance, to keep the total time T constant. We investigated also the effect of the finite MW pulse duration. Considering the case of a Gaussian-shaped train of magnetic impulses under a CPMG control sequence, we calculated phase accumulation and sensitivity when excluding from the spin evolution the time intervals where the π pulses occur, finding the same theoretical values of η, for all the considered total sensing times T. We underline that this procedure does not correct the model for the contribution to $\chi_n(T)$ given by MW pulse imperfections or finite duration [147], but it confirms that the pulses can be considered instantaneous in our picture for the accumulated spin phase $\varphi_n(T)$; we verified that this approximation is valid up to $\pi_{MW} \leq 0.5$ μs for $n = 50$ and $T \sim 250$ μs and was very effective for pulses duration $\pi_{MW} = 56$ ns and $T \geq 50$ μs, as in our case.

The described procedure is quite general and could be applied to a broad range of sensing scenarios. To demonstrate its reliability, we considered some

exemplary target fields and related control models, varying, e.g., the number of parameters tackled by the optimization algorithm. We first considered AC fields with single or multiple frequencies, and we started optimizing η as a function of total time T and the AC field phase α, while fixing the number of pulses ($n = 8$) and setting $\tau = T/n$ for all time intervals between the π pulses. We proceeded then to allow more flexibility in the optimization by varying the duration of each time interval between π pulses, starting from an initial guess given by a periodic (CPMG) sequence with $n = 50$. The experimental results, presented in Sec. 3.3.2 and 3.4, are in agreement with our theoretical optimization and pave the way for more complex treatments, e.g. extending the noise model or the typology of considered measurement techniques, for optimal sensing perspectives towards the sensitivity limits.

3.3 Optimized sensing for oscillating fields

In this section, I address the problem related to the optimization for sensing oscillating magnetic fields. We start from the simple single-frequency case, in order to test the reliability of the method, to ones with arbitrary spectral composition, for which searching the best experimental conditions in a multi-parameters space parameter to boost the sensitivity is necessary.

3.3.1 Monochromatic field case

As a proof of principle, I first focus on the simple case of monochromatic sinusoidal signals

$$b(t) = b\cos(2\pi\nu t + \alpha), \tag{3.13}$$

with $\nu \approx 20 - 125$ kHz (further results will be shown in 3.3.3). We note that measuring signals in this frequency range at a magnetic field $B \sim 39.4$ mT is a difficult task since the signal is obscured by the ^{13}C bath field. Indeed, even if the Larmor frequency at such field is $\omega_L = 2\pi \times 424$ kHz (as shown in Fig. 3.2(a)), the presence of a periodic filter produces coherence collapses at times $T_k = nk\pi/\omega_L$, with k odd integer, and therefore competing with the target for $k \in \{3, 21\}$. We start from a common pulsed dynamical decoupling sequence, the CPMG multipulse sequence, which has been demonstrated not only to extend the qubit's coherence [66], but has been also successfully employed in sensing to measure monochromatic AC magnetic fields (see, e.g., Refs. [22, 149–152]). However, CPMG is highly selective in frequency: Its filter function $Y_{n,T}(\omega)$ is indeed peaked at $\nu = 1/(2\tau)$ [5]. In the case of

[5] For a bare CPMG sequence, the filter function is $Y_{n,T} = \sqrt{2}\left[2\sec(\pi\nu\tau)\sin(\pi\nu n\tau)\sin\left(\frac{\pi\nu\tau}{2}\right)\right]$, which is peaked at $\nu = k/2\tau$, with k being an

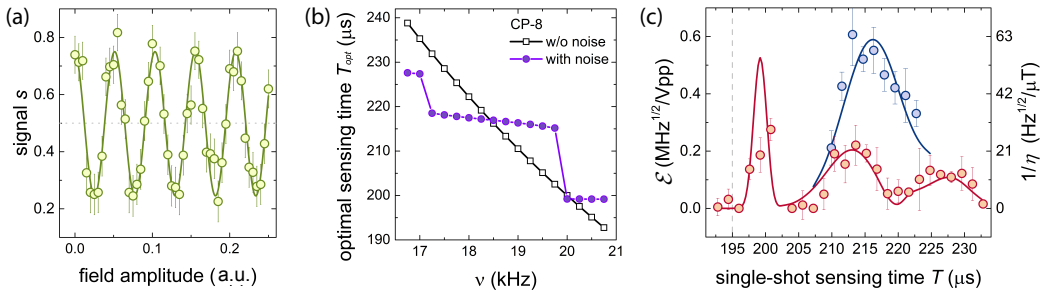

Figure 3.3: Optimized sensing of monochromatic fields. **(a)** Experimental signal measured in the presence of a monochromatic target AC magnetic field, $b(t) = b\cos(2\pi\nu t + \alpha)$, with $\nu = 9.24$ kHz and $\alpha = 0$, as a function of the target magnetic field amplitude b. Here, the spin sensor is controlled with a CPMG sequence of $n = 4$ equidistant π pulses. Dots are the experimental data, the curve is a cosinusoidal fit. Error bars are the statistical errors over 2×10^5 repeated measurements. **(b)** Theoretical prediction of the optimal sensing time of a CPMG-8, calculated for a target AC magnetic field $b(t) = b\cos(2\pi\nu t + \alpha)$, as a function of the AC frequency ν. The black empty squares are the optimized solutions of the sensing problem when neglecting the presence of the noisy environment, and the black curve represents the expected optimal time, $T_{opt} = n/(2\nu)$, with no fitting parameters. Purple dots are optimized solutions including the noise-induced decoherence of the spin qubit (the line is a guide to the eye). **(c)** Inverse of sensitivity, in the presence of a cosinusoidal field $b(t)$ of frequency $\nu_0 = 20.5$ kHz under CPMG control, with $\alpha = 0$ (in red), and with $\alpha = 102°$ (that is, an initial delay time $t_0 = 0.28/\nu_0$) resulting from optimization (in blue). Dots are experimental value of $\mathcal{E}$ (left side vertical axis - see text) lines are theoretical $1/\eta$ (right side vertical axis) The experimental error bars come from the slope uncertainty of the experimental signal p_n.

interest, if the target signal has frequency close to the center of the noise spectrum (the Larmor frequency of the ^{13}C spin bath), CPMG control may not be the best choice, since the sequence achieving noise cancellation also leads to a significant attenuation of the signal to be measured.

As a warmup for the full optimization, we optimized the control over a restricted space of two parameters, the sensing time T and the initial phase shift α, with a fixed number of pulses, $n = 8$. First, fixing $\alpha = 0$, we found the optimal sensing time as a function of the AC frequency, as reported in Fig. 3.3(b). Taking into account decoherence effects appreciably modifies the optimal sensing time (purple curve), compared to the results obtained

odd integer index, where the higher harmonics have decreasing weight (see [7] and Tab. B.1).

in the absence of noise sources (black curve), where the optimization routine recovers the expected analytic solutions $T_{opt} = n/(2\nu)$; the latter would be given considering $\chi_n(T) = 0$ by maximizing the phase ϕ_n in Eq. 3.12. Then, we optimized both T and α. To evaluate the global convergence of the optimization, we have also mapped $1/\eta$ in the two-dimensional (2D) parameter space (T, α). Figure 3.1(b) shows this map for an AC field of frequency $\nu_0 = 20.5$ kHz. This allows the results of the optimization to be compared with the brute-force approach of an extensive search in the parameter space. The full optimization of the two parameters, including noise effects, is able to find the global minimum of sensitivity (the optimized parameters are $T = 216$ μs and $\alpha = 102°$, corresponding to an initial delay time $t_0 = 0.28/\nu_0$ of the control sequence). Figure 3.3(c) shows some cuts of the previous 2D map as a function of T, with $\alpha = 0$ (red solid line) and with $\alpha = 102°$ (the optimal value resulting from the numerical search, blue line). Using Eq. (3.9), we have also calculated the experimental observable $\mathcal{E} = K/\eta$ (left side, vertical axis in Fig. 3.3(c)), which can be directly compared with the experimental findings at fixed $\alpha = 0$ (red dots) and with $\alpha = 102°$ (blue dots). We find good agreement of the experiments with the results of the optimization.

We also investigated monochromatic AC magnetic fields in a different frequency range, at 125 kHz, as shown in Fig. 3.4. For a CPMG sequence with $n = 8$, we evaluated the theoretical value of $1/\eta$ and measured $\mathcal{E}$ as a function of the measurement time T. I also remark that even in the simple case

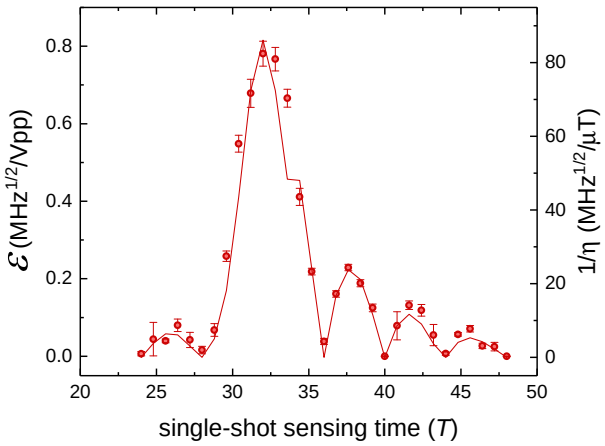

Figure 3.4: Sensitivity to a monochromatic field as a function of sensing time T. We plot $\mathcal{E}$ from experimental data and $1/\eta$ from simulations, for an XY-8 CPMG sequence used to sense a field $b(t) = b\cos(2\pi\nu_0 t)$ with $\nu_0 = 125$ kHz. Solid lines and scatters refer to simulations and experimental data, respectively.

of one-parameter optimization, including the noise effects yields a different optimal sensing time than what was calculated in the absence of noise ($T = n/(2\nu_0)$, gray vertical dashed line), and this is also reflected in the observed experimental peak of $\mathcal{E}$ - vs - T.

3.3.2 Optimized sensing of multitone AC signals.

We now tackle the more complex task of measuring arbitrary time-dependent signals. We consider multitone magnetic fields, in the form

$$b(t) = b \sum_{i}^{m} w_i \cos(2\pi\nu_i t + \alpha_i), \tag{3.14}$$

where m is the number of Fourier components, $b_i = b\, w_i$ their amplitudes (with $\sum_i w_i = 1$), ν_i their frequencies, and α_i the initial phases. We employ our optimization tool to engineer optimal control sequences of nonequidistant π pulses that may extract information from multitone target signals, while refocusing spin dephasing better than common dynamical decoupling solutions.

As already mentioned, common multipulse control sequences like CPMG are, in general, highly selective in frequency. For this reason, these sequences may exhibit suboptimal performances when probing a multitone target field due to attenuation of some frequency components. In addition, increasing the interrogation time to enable a larger phase accumulation, thus improving measurement sensitivity, also further narrows the width of the filter function $Y_{n,T}$ as $\sim 1/(T)$. If the magnetometry task consists in measuring the signal amplitude of a spectrally characterized source as we are considering here, CPMG looses significant part of information apart from one frequency component at a given sensing time, when fixing the number of pulses n and sweeping the total time $T = n\tau$.

We started by analyzing the sensitivity in three (total) time intervals, $T < T_2$, corresponding to different measurable frequencies, given for the simple CPMG sequence by $\nu = n/(2T)$. For each of these total time intervals, we increased the complexity of the magnetic field by choosing three random frequency components $\{\nu_i\}$, $i = 1, 2, 3$ (or, equivalently, fields made of $m = 3$ Fourier components each), in different ranges between 20 kHz up to 141 kHz, and with different amplitudes. In these cases, we optimized the sensitivity as a function of the total time under a CPMG-8. The results, presented in Fig. 3.5, show good agreement between data and our predictions for all the cases investigated.

To emphasize that the phase accumulated by the spin-qubit sensor under CPMG control reflects the spectral composition of the signal, showing peaks

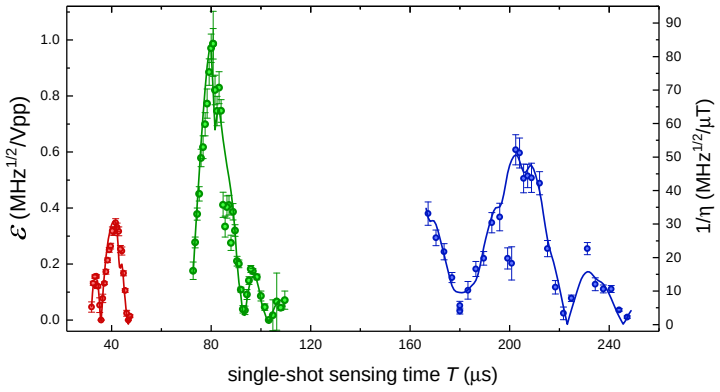

Figure 3.5: Three-components target fields in different frequency ranges. $\mathcal{E}$ (left vertical axis) and $1/\eta$ (right vertical axis) as a function of the sensing time T for 3-chromatic AC fields under CPMG-8 sequences. Solid lines and scatters refer to simulations and experimental data, respectively. Given the field $b(t) = b\sum_i^m w_i \cos(2\pi\nu_i t + \alpha)$, the three datasets correspond to the following parameters: In red, $\nu_i = (77; 96; 141)$ kHz and $w_i = (0.45; 0.43; 0.12)$; in green $\nu_i = (50.5; 48.1; 46.2)$ kHz and $w_i = (0.40; 0.44; 0.16)$; in blue, $\nu_i = (25.0; 20.4; 19.9)$ kHz and $w_i = (0.54; 0.13; 0.33)$.

at times $\tau_i = 1/(2\nu_i)$, we tested one of the previous three cases under a CPMG train of $n = 50$ pulses, where the width of the filter is narrower by a factor $50/8 \sim 6$; the results are shown in Fig. 3.6(b) (green solid line). However, the sensor's decoherence influences the final sensitivity by suppressing the response of one of the three frequency components, as shown both in theory and in experiment (green solid line and yellow dots in Fig. 3.6(c)).

For this kind of scenario, optimal control strategies offer a key advantage. Optimal control can indeed be exploited to find optimal distributions of the π-pulse positions. Sequences of non-equally distributed pulse spacings, devised by means of analytical models, have been indeed demonstrated to correct for selectivity of CPMG in certain cases [73, 74, 153, 154], also for different experimental platforms [133]. In the case of multitone AC signals to be measured, such sequences enable to simultaneously collect signal from all the various frequency components thus achieving a faster phase accumulation.

Therefore, we optimized the single time intervals, maintaining the number of pulses fixed to $n = 50$, by keeping the time delay symmetric around each π pulse, as shown in Fig. 3.7, in order to ensure cancellation of static noise and better refocusing of low-frequency noise. Including also the optimization of the phase of the multitone field ($\alpha_i = \alpha$), or equivalently, the initial time of the measurement sequence, this optimization manages 51 free

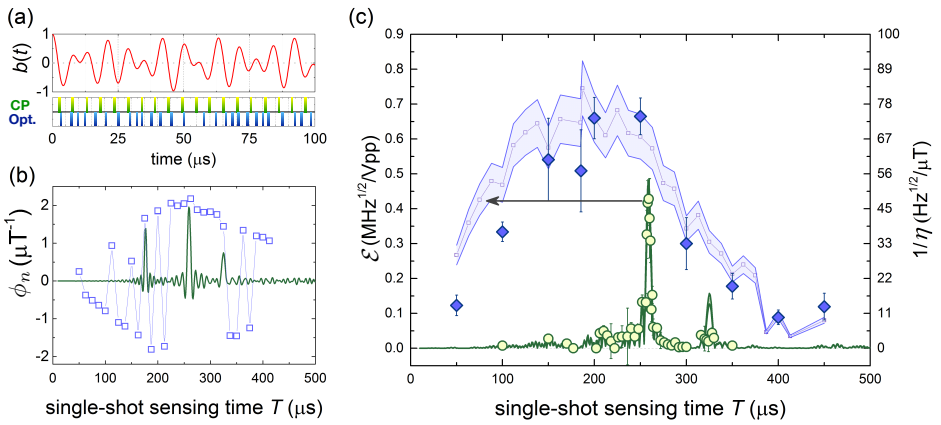

Figure 3.6: Optimized sensing of multitone AC fields. (a) Upper panel: Sample multitone target field, $b(t) = b\sum_i^3 w_i \cos(2\pi\nu_i t + \alpha_i)$, with $\alpha_i = 0$, frequencies $\nu_i = (77; 96; 141)$ kHz, and amplitudes $w_i = (0.45; 0.43; 0.12)$ G, respectively. Bottom panel: In green, position of the first 19 π pulses of a Carr-Purcell sequence of 50 equidistant π pulses (CPMG-50) with optimized sensing time ($T = 260$ μs); in blue, position of the first 27 π pulses of an optimal control sequence of 50 non equally-distributed π pulses with optimized time intervals and optimized initial phase ($T = 187$ μs, $\alpha_i = 0.3$). (b) Phase $\phi_n(T) = \varphi_n(T)/b$ accumulated by the spin qubit sensor during the sensing time T in the presence of the field $b(t)$, under a control field of $n = 50$ π pulses, in the cases of CPMG-50 (solid line) and optimized control (blue squares). (c) Experimentally measured $\mathcal{E} = K/\eta$ in the presence of the field $b(t)$ under CPMG-50 (dots) and optimized control (diamonds). The curves represent the theoretical prediction for $\mathcal{E}$, for CPMG-50 (solid green line) and optimized control (blue line), respectively, obtained by rescaling $1/\eta$ (right-hand side, vertical scale) with the unique factor K. The shaded area takes into account the experimental uncertainty due to K (see Sec. 3.2).

parameters. We performed different optimization runs as a function of the total measurement time, keeping T constant in each of them. The only additional constraint that we imposed was to force the times τ_j between different π pulses to be longer than about 10 times the π pulse duration, which in our case means $\tau_j > 600$ ns. This restriction was to ensure that no MW pulses would be very close to each other, as that would have resulted in the π pulses canceling each other, giving an effective sequence with a different n.

The results of optimization for the multitone field considered above are shown in Fig. 3.6. As shown in Fig. 3.6(b), the optimization method leads to a remarkable improvement in the accumulated phase per unit field amplitude ϕ_n (blue squares) compared to CPMG (green line), over an extremely wide range of sensing times. The overall-optimal control sequence (obtained with

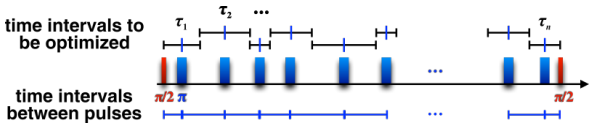

Figure 3.7: Time interval τ_j engineering. Optimization scheme of the n time intervals τ_j of a measurement sequence with n π pulses. Here, $\tau_j = (t_j + t_{j+1})/2$, where t_j are the $n+1$ time intervals between the π pulses, with $j = 0, ..., n$, and $t_0 = t_{n+1} = 0$.

sensing time $T = 187$ μs and phase shift $\alpha = 0.3$) realizes a sensitivity $\eta_{opt}^{best} = 12$ nT/$\sqrt{\text{Hz}}$. Since each of our sensing experiments is typically obtained by averaging over $N = 2 \times 10^5$ measurement shots, the optimized control sequence enables the measurement of a local field of 2 nT. The improvement in sensitivity is more than 2 orders of magnitude compared to the sensitivity of CPMG ($\eta_{CP} = 8.3$ μT/$\sqrt{\text{Hz}}$) at the same sensing time. We remark that the best sensitivity obtained with CPMG control is still a factor of 1.75 worse than the best sensitivity achieved with the optimized control ($\eta_{CP}^{best} = 21$ nT/$\sqrt{\text{Hz}}$), and with an acquisition time ($T = 260$ μs) that is 40% longer than the optimal sequence. In addition, optimized control is able to achieve the same η_{CP}^{best} 3 times faster then CPMG ($T = 75$ μs, compared to $T = 260$ μs; see black arrow in Fig. 3.6(c)).

Thus, optimal control is able to attain a remarkable enhancement of sensitivity compared to standard control when measuring multitone AC fields at fixed interrogation time. Besides, optimal control makes it possible to speed up the measurement while maintaining the same sensitivity of standard control, e.g., when measuring target signals with inherently short coherence times or in the presence of fast experimental drifts that limit the available coherent single-shot measurement time.

We then characterized the sensitivity of the qubit sensor to a multitone signal as a function of the amplitude of one of its components. We still considered the case of the field discussed in Fig. 3.6. We tuned the weight of the third frequency component, while maintaining constant the total field amplitude b ($w_1 + w_2 + w_3 = 1$), and $w_2/w_1 = 0.96$ as in the previous case. As shown in Fig. 3.8, under the CPMG sequence, the increase of the amplitude of the third field component w_3 corresponds to the emergence of a peak of $1/\eta$ at $T = n/(2\nu_3)$, as expected. The signal amplitude increases indeed due to the combination of good spin coherence at that specific measurement time and larger acquired phase because of longer integration time. For the optimal control results we observe not only better performance for increasing

w_3 amplitudes, but we still preserve the broadening of the $1/\eta$ peak already observed in the case presented in the main text, as well as a small shift of the optimum η towards shorter times T.

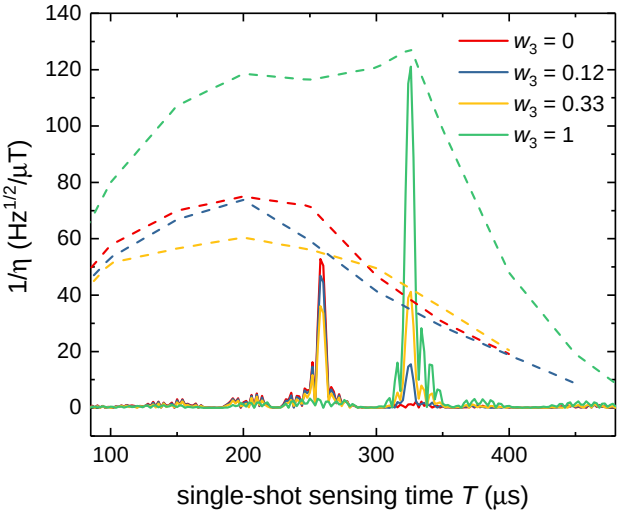

Figure 3.8: Multitone target signals with different relative weights. Inverse of sensitivity to a multitone signal with three frequency components $\nu_i = (77; 96; 141)$ kHz, when varying the weight of the third component w_3 compared to the others (with $w_1 + w_2 + w_3 = 1$). Solid lines refer to CPMG-50 sequences, dashed lines refer to optimal control sequences of $n = 50$ pulses with optimized time intervals, respectively.

3.3.3 High frequency range for cosinusoidal signals

Up to now, I focused on an intermediate frequency range that overlaps with the main source of decoherence present in our system. However, measuring fields at higher frequency with our optimization protocol is possible. The general upper limit for measurement methods based on dynamical decoupling is given by the inverse of the interaction time for the spin control, i.e. the π-pulse duration, typically on the order of some tens of nanoseconds (but pulses as short as 1 ns are possible [155]).

In order to show the potential of our optimization method at higher frequencies, we consider a practical scenario where the high frequency of the target field competes with the noise. This is for example the case of shallow NVs [44, 75, 136, 156], where the interaction with surface spins, e.g. hydrogen nuclear spins [157], introduces a noise source in the same high frequency range. Following Ref. [136], we consider a typical noise spectrum in the presence of a static magnetic field $B \approx 45$ mT, given by a

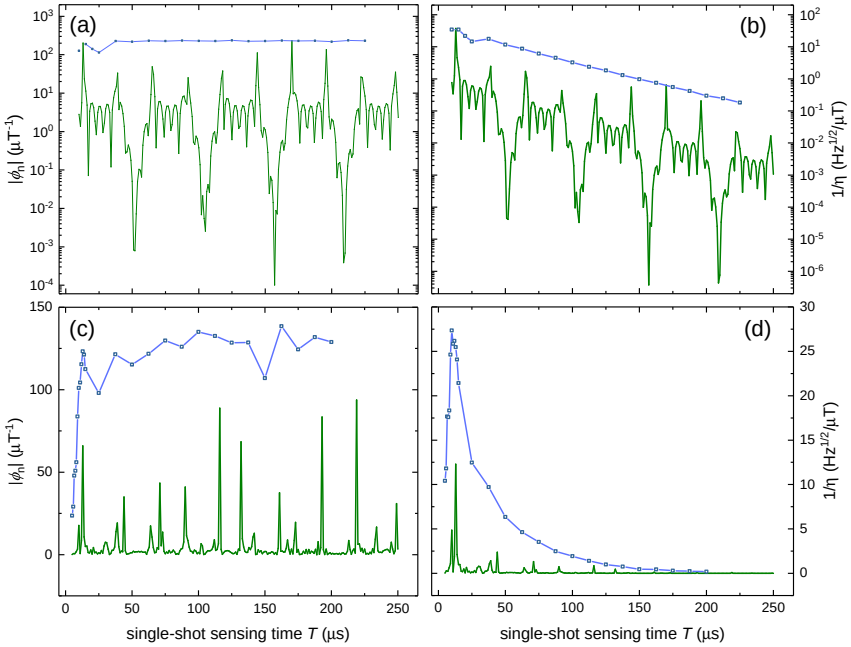

Figure 3.9: Target fields in the frequencies range [1.5 − 2.5] MHz. Acquired phase $|\phi_n|$ (left panels) and inverse of sensitivity $1/\eta$ (right panels) of a qubit sensor under CPMG-50 control sequences (green solid lines) and optimized control sequences with the same ($n = 50$) number of pulses (blue lines with squares). (a)-(b): Monochromatic target field with frequency $\nu = 1.912$ MHz; logarithmic scales emphasizes the similar behavior of $|\phi_n|$ and $1/\eta$ as a function of time T. (c)-(d): Multitone target field, with frequencies $\nu_i = (1.708; 1.941; 2.461)$ MHz and amplitudes $w_i = (0.15; 0.42; 0.43)$.

spin bath with Larmor frequency close to 2 MHz, yielding decoherence time $T_2 \simeq 50$ μs under multipulse control. As for target fields, we consider both a monochromatic signal and a 3-chromatic field with the same amplitude weights, $w_i = (0.15; 0.42; 0.43)$; the frequencies are again randomly picked, in the range $1.5-2.5$ MHz. Figure 3.9 shows numerical simulations of the acquired phase and sensitivity of the qubit sensor under CPMG and optimized sequences with $n = 50$ pulses. For a monochromatic target field (Fig. 3.9a and 3.9b), our optimization protocol yields an enhancement of the acquired phase compared to CPMG control on a wide range of total time. Both CPMG and optimized sequences show the same sensitivity trend as a function of total time, and reach the same minimum sensitivity. For the multitone case, shown in Fig. 3.9c and 3.9d, the optimized control provides significant advantage, confirming that our method can overcome the "monochromaticity"

of the CPMG filter, and achieving an improvement of the optimal sensitivity by a factor of 2.

3.4 Optimized sensing of trains of magnetic impulses.

We have applied optimal control to the different scenarios where the target magnetic field is a train of impulses. This is, in general, the case of the temporal shape of electric and magnetic fields associated with cardiac, neural, and nervous activities of human and animal organs [27, 126–128]. For this kind of application, the NV sensors may offer the remarkable advantages of subcellular spatial resolution, in addition to high sensitivity, and biocompatibility [158].

As illustrative models for these biological applications, we consider a train of Gaussian-shaped impulses. The target field is thus of the general form, shown in Fig. 3.10(a),

$$b(t) = b \sum_{i=0}^{m_r} e^{-\frac{(t-i\Delta t)^2}{2\sigma^2}}, \tag{3.15}$$

where $1/\Delta t$ is the repetition rate and m_r is the number of repetitions, with $m_r\,\Delta t \gg T$. In this case, standard dynamical decoupling may be underperforming since the target signal $b(t)$ is positive definite in the whole temporal domain; thus, the product $y_n(t)b(t)$ may be alternately positive and negative, reducing the accumulation of a useful phase (see Eq. (3.3)). In other words, each time a π pulse reverses the spin dynamics, it can partially cancel not only the effect of unwanted noise but also the phase associated with the field to be measured.

Figure 3.10(b)-3.10(i) compares the results of CPMG control (green-colored curves) and optimal control (in blue), when varying the width σ of the target Gaussian pulse train and its repetition rate $1/\Delta t$. In this case as well, we evaluate the effect of control sequences made of $n = 50$ π pulses. In the optimization, all the time intervals between the control pulses, symmetrized around the π-pulse positions, are free parameters. The left panels represent the modulus of the phase accumulated by the spin qubit sensor per unit of the target magnetic field amplitude $|\phi_n|$, whereas the right panels represent the inverse of sensitivity $1/\eta$, as a function of the sensing time T.

Optimal control outperforms CPMG in accumulating a useful phase due to $b(t)$ over a large sensing-time range. Both CPMG and optimal control lead to their largest phase accumulation when $T \simeq n\Delta t/2$, where they give similar results in ϕ_n. This condition corresponds to having couples of π

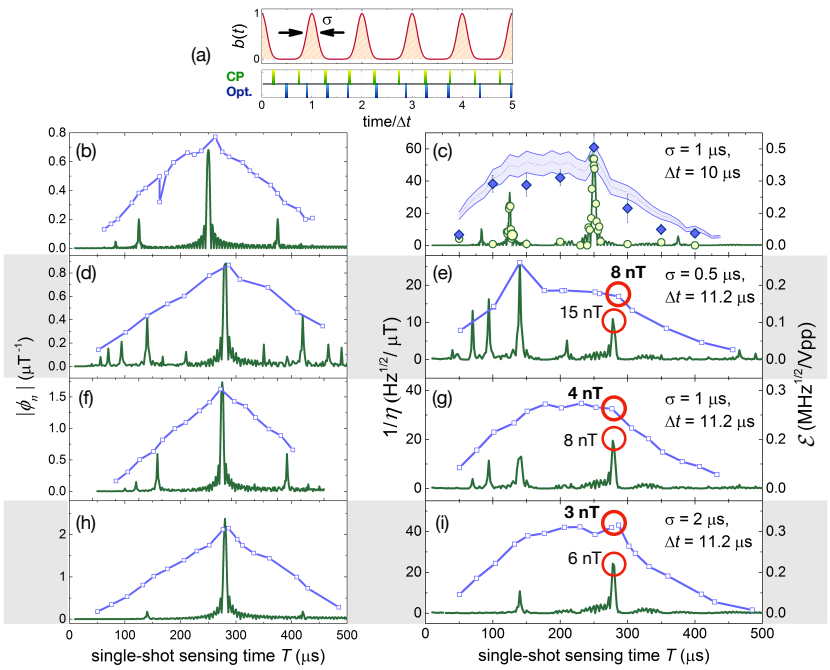

Figure 3.10: Optimal sensing of Gaussian impulses. (a) Upper panel: Target signal made of a train of Gaussian impulses of width σ and repetition rate $1/\Delta t$. Bottom panel: Position of the first 10 π pulses of a CPMG control sequence of 50 π pulses (CPMG-50), with total sensing time $T = 280$ μs optimized to sense a train of Gaussian impulses with $\sigma = 2$ μs, $\Delta t = 11.2$ μs (in green), and optimal position of the first 10 π pulses of a control sequence of 50 π pulses (in blue), optimized to sense the same target field (50 optimization parameters). (b)-(i) Modulus of the phase accumulated by the spin qubit sensor in the presence of the target field (left panels), and the inverse of sensitivity $1/\eta$ (right panels), as a function of the sensing time T, under CPMG-50 control (green solid curves), and under optimized control (blue lines with squares) with bounds $\tau \in (0.6 - 10)$ μs (see Sec. 3.3.2). (c) Measurement of the experimental observable $\mathcal{E}$ as resulting from CPMG experiments (yellow dots), and from optimized control (blue diamonds), scaling as indicated on the right-hand side vertical axis. The target field parameters of panels (b)-(i) are as follows: (b,c), $\sigma = 1.0$ μs, $\Delta t = 10$ μs; (d,e), $\sigma = 0.5$ μs, $\Delta t = 11.2$ μs; (f,g), $\sigma = 1.0$ μs, $\Delta t = 11.2$ μs; (h,i), $\sigma = 2.0$ μs, $\Delta t = 11.2$ μs.

pulses located in each “empty" time window between two Gaussian pulses of the target field, albeit optimal control corrects, in a nontrivial way, the distribution of π-pulse positions to minimize η, as represented in Fig. 3.10(a) (CPMG, green vertical bars; optimal control, blue vertical bars). Thus, the π pulses partially reverse the spin qubit dynamics due to undesired noise,

but do not cancel the phase due to the target field $b(t)$.

We note that, even when the phases accumulated with CPMG and with optimal control are comparable, optimal control compensates better than CPMG for decoherence, leading to better overall sensitivity. While here I do not explore this result further, it seems to indicate that numerically optimized sequences might also be useful for other quantum information tasks, such as building a robust memory. Figures 3.10(e), 3.10(g), and 3.10(i) show that optimal control of the spin qubit improves its sensitivity to Gaussian multipulse signals up to a factor of 2, enabling the measurement of multipulse magnetic fields down to 3 nT. As shown in Fig. 3.10(c), the measurement of the experimental observable $\mathcal{E} = K/\eta$ confirms the theoretical prediction of sensitivity both for the CPMG control (yellow dots) and for optimal control (blue diamonds).

3.4.1 Optimized sensing of a slowly-varying Gaussian impulse

The final target field that we considered is a magnetic field with a slow temporal profile given by a single Gaussian impulse of several hundreds of microseconds; this profile results in a quasi-constant signal, broad and positive during the whole sensing time. This target signal is a good model for any slow varying field, and in particular it can be considered a good model of neural action potentials associated with human cells [27, 159, 160]. We note that those signal durations are even longer than what considered here, but still on the same order of the milliseconds coherence time of NV spins in purified ^{12}C samples. Here, to take into account our sample coherence time, we considered a field similar to the one expressed in Eq. (3.15), $b\, e^{-(t-t_G)^2/(2\sigma^2)}$ with $\sigma = 150$ μs.

We first study the acquired spin phase per unit field amplitude, $\phi_n = \varphi_n/b$, and the sensitivity η as a function of the Gaussian center t_G under CPMG sequences ($n = 50$ π pulses) with different values of pulse delay τ. Figure 3.11 shows that for both these quantities, when $\tau \leq 10$ μs the optimal center position is $t_G = T/2$. For larger τ, $1/\eta$ and ϕ_n show a minimum at $t_G = T/2$ and are symmetric around it. In particular, when $T = n\tau \geq 4\sigma$ (here 600 μs) the optimal case is to have the magnetic field pulse at the beginning or end of the measurement sequence. Moreover, even if the trend of $1/\eta$ is the same of ϕ_n, the relative amplitude at different τ changes, due to the dependence of the electronic spin coherence on T. We note that the value of $1/\eta$ in these conditions is too low to be measured in our experiments.

We investigated also CPMG with different pulse numbers, $n = 8$, finding

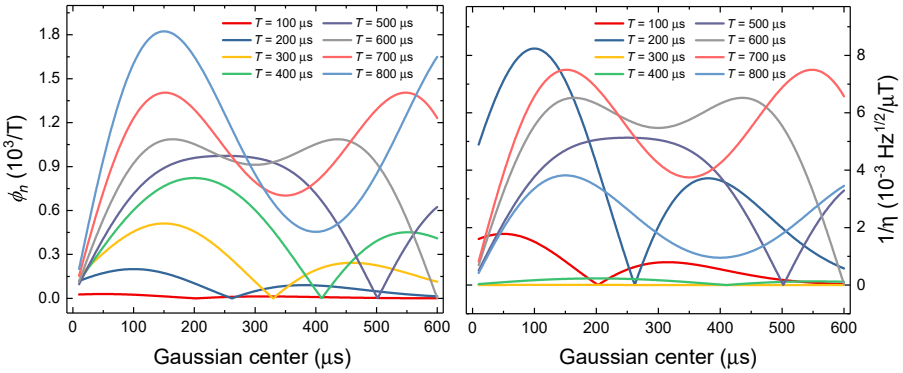

Figure 3.11: Sensing slowly-varying fields. Phase accumulated and sensitivity of the spin qubit, in the case of a slowly varying Gaussian target field, as a function of the Gaussian center for CPMG sequences, $n = 50$, for eight different values of $\tau = T/n$.

for $T \sim 150$ μs a better (lower) value of η with respect to the previous case. So we decided to perform an optimization of the time intervals τ_j between the MW pulses. We found a high improvement with a large peak of $1/\eta$ centered at measurement time around 100 μs. Results for both CPMG and sequences with optimized time vector are shown in Fig. 3.12. Also in this case, the best value of η is at the limit of our experimental signal to noise ratio.

3.5 Discussion

We have devised a versatile and robust method of optimal control for quantum metrology with one qubit, and we have applied this optimal control method to the measurement of weak time-varying magnetic fields with an NV spin sensor.

The key insight of our optimal control strategy is the introduction of an unconventional optimization metric, the qubit sensor's sensitivity. The minimization of sensitivity is made by searching the optimal control field that realizes the optimal compromise between useful accumulation of the spin phase due to the external field to be measured and noise refocusing. The developed optimization algorithm offers the advantage of fast convergence and simplicity. We have further investigated the robustness of this method for different kinds of real target fields. Optimal control outperforms standard dynamical decoupling in different scenarios, ranging from multicomponent

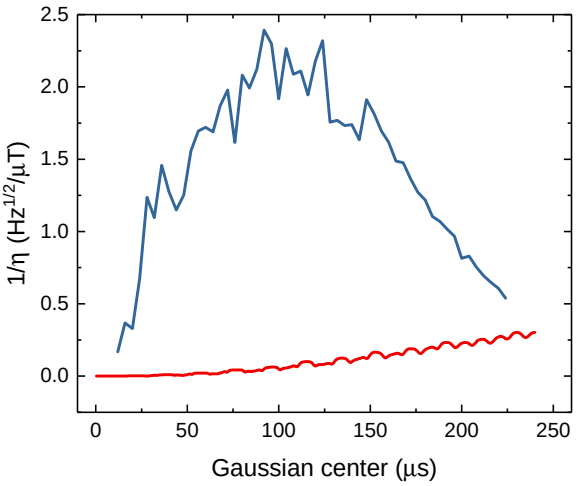

Figure 3.12: Optimized vs CPMG sequences to probe a Gaussian pulse as large as the total sensing time. Inverse of sensitivity for a CPMG sequence (red), and a optimal control sequence (blue) with optimized time intervals τ_j. In both the cases, $n = 8$.

AC target fields in a wide frequency range of the radio-frequency domain, to trains of impulses, which are illustrative examples of the typical shape of the electromagnetic field of interest in biology and physiology.

In the cases investigated, optimal control enables larger phase accumulation over wide sensing-time windows, as well as better cancellation of the effect of external noise on the spin dynamics. Sensitivity of the qubit sensor under optimized control shows an improvement up to a factor of 2, enabling the measurement of pulsed magnetic field down to amplitudes of 2 nT. The comparison of $1/\eta$ with the experimental observable $\mathcal{E}$ demonstrates the reliability of this optimal control method applied to the NV spin sensor.

Beyond the results obtained in exemplary situations, our novel method is one of the first extensions of optimal control methods to quantum sensing. This application raises novel challenges and opportunities, in particular related to the need for new metrics for optimization, as well as the challenge to include nonunitary evolution in the numerical optimization. We underline that our optimization method can be extended to larger multidimensional space of parameters; for instance, one can optimize the number of π pulses that flip the spin qubit during the sensing time, according to the target signal to be measured. Moreover, while we always considered control sequences given by a series of π pulses, our scheme can also be generalized to other control strategies of the NV spin qubit.

Our strategy can be useful for metrology in the face of more and more

demanding requirements for the NV spin qubit to sense weak time-varying electric and magnetic fields in noisy environments, with the sensing task aimed at measuring their amplitude, e.g., for detecting the number of spins in small electronic or nuclear ensembles [161–163], revealing excitations in nanostructured antiferromagnetic or multiferroic materials [164], or measuring biological activity at the nanoscale [27]. Adaptive strategies could also be used to extend this scheme to fields with an unknown temporal profile. Moreover, the method can also be applied to other physical platforms, such as ultracold atoms or trapped ions. Furthermore, the demonstrated enhanced protection of the spin qubit against noise-induced decoherence also makes optimal control a strategic tool for building memories in solid-state systems.

Chapter 4

Environment characterization: From spin bath to coherent coupling

As introduced in Ch. 3, the knowledge of the environment surrounding a quantum system is an important tool to enhance the capabilities of the qubit control techniques for sensing purposes. Moreover, characterizing the qubit-environment interactions is critical for its practical use for the realization of robust quantum devices, also for quantum information processing. A full understanding of the qubit environment enables developing effective strategies against decoherence, including optimized dynamical decoupling sequences [72] or quantum error correction codes [165]. Moreover, the controlled and coherent coupling of the qubit with part of its environment may provide an additional resource to enhance its computational or sensing performance [166, 167].

In this chapter I present a protocol implemented with an NV center that extends the method already presented in Sec. 3.1.2 and allows us to unravel the characteristics of the NV environment, comprising ^{13}C nuclear spins randomly distributed in the diamond lattice. They give rise to both unknown coherently coupled quantum systems, and a larger quantum bath that can be modeled as a classical noise field [168]. The thermal and quantum fluctuation of this environment, and the distribution of environment-qubit interaction strengths make this an extremely rich scenario where to test our method. Several methods [64, 135, 141, 169, 170] have been proposed for noise spectroscopy. Relaxometry, stemming from magnetic resonance [171], has been exploited to investigate especially high-frequency noise based on the measurements of the sensor T1 relaxation time. Dynamical decoupling [142,143] and dynamic sensitivity control [172,173] techniques are also used to to probe

colored noise via pulsed or continuous driving of the NV electronic spin. Most of these methods, however, assume the environment to be simply a classical stochastic bath and rely on the assumption that the noise is weak enough to enable relatively long qubit coherence time under the applied control.

The protocol that we implemented for characterizing the qubit environment overcomes the challenges arising when those assumptions are not verified. We show how to reconstruct the noise spectral density even when limited by relatively short coherence times, and identify the coherent quantum coupling with the nearest nuclear spins. Importantly, we also demonstrate that in the presence of high magnetic field ($\approx 200 - 635$ G) the acquired knowledge of the environment can reliably predict the qubit dynamics quite generally, even under driving controls that differ from the ones used for noise spectroscopy.

The first part of the Chapter, Sec. 4.1, provides a short introduction to noise spectroscopy, focusing in particular on methods based on DD techniques. Sec. 4.2 shows the specific experimental conditions and some exemplary experimental results that we use to distinguish different interactions between the NV spin and the environment. In Sec. 4.3 I present our method to obtain the noise spectral density exploiting DD techniques. In particular, when the noise amplitude due to the carbon nuclear spin bath induces a fast coherence decay in correspondence of its noise frequency, we demonstrate that it is necessary to resort to high harmonics of the filter function to obtain accurate and precise information of the spectrum. Then, in Sec. 4.4, I pass to analyze the hyperfine coupling with nearby ^{13}C nuclear spins, showing also our ability to model the different behavior under different $|0\rangle \leftrightarrow |\pm 1\rangle$ combinations. Sec. 4.5 presents a systematic characterization of both the spin bath and the coherent coupling with nearby nuclear spins when varying the external environment by tuning the magnetic field strength. In Sec. 4.6 I discuss the predictive power of the reconstructed environment, also for qubit control techniques different from the ones used to obtain the NSD. Finally, I summarize the main results obtained from our environment characterization in Sec. 4.7.

4.1 Noise spectroscopy

The interaction of a system with a noisy environment can be spectrally characterized through the analysis of relaxation and dephasing processes occurring to the system itself.

As already mentioned in Sec. 3.1.2, the approach that we exploit is based on the systematic analysis of the sensor decoherence under a set of dynam-

ical decoupling (DD) control protocols [66, 133, 141, 143–145]. As already discussed in Sec. 1.6 and widely in Ch. 3, ideally, periodic DD protocols realize narrow frequency filters that select only a specific coupling and frequency, while decoupling the sensor from all the other interactions. Referring to App. B, the control field acting on the sensor can be described by a modulation function $y_n(t)$, the squared Fourier transform of which defines the control filter function $Y_{n,T}(\omega)$ (see Eq. (B.2)) over the measurement time T. We recall here the definition of the sensor coherence decay:

$$\chi(t) = \int \frac{d\omega}{\pi\omega^2} S(\omega)|Y_{n,T}(\omega)|^2, \tag{4.1}$$

where $S(\omega)$ is the power spectral density function of noise. The filter function approach effectively describes pure classical dephasing [64, 169, 174]. To fully characterize the environment of an NV spin, we followed the method proposed in Ref. [141] and proven in Ref. [142] for a nuclear spin system. The method stems from the relation between the NSD and the coherence decay time of the qubit under multipulse control (see Sec. 4.3). To achieve high spectral resolution, one exploits the frequency selectivity of equispaced sequences of π pulses separated by a constant time, here defined $2t_1$, such as CPMG [67]. For sufficiently high number of pulses, this kind of control sequences is well described by a narrow monochromatic filter function, the width of which scales as $1/(n\,t_1)$. As we will discuss in Sec. 4.3, the validity of this approximation depends on the characteristics of the noise itself, and deviations could lead to an inaccurate evaluation of the NSD in terms of noise amplitude and frequency width.

In the practical scenario, where we apply our method, the NV spin couples with both a dephasing spin bath and individual nearby nuclear spins. While the nuclear spin bath exhibits collective effects, even in the quantum regime, and can be trated with a classical central spin model [175, 176], the strong coupling with single proximal nuclei induces a coherent dynamics of the qubit sensor and must be treated independently.

4.2 Experimental conditions

We investigated the environment of a single deep nitrogen-vacancy center placed around 13 μm below the diamond surface. All the experimental work was performed by taking advantage of the setup discussed in Sec. 1.4.

A Ramsey free-induction-decay experiment features the presence of at least one strongly-coupled nucleus close to the NV spin (coupling strength $\omega_h \sim 2\pi \times 700$ kHz), apart from the nitrogen composing the NV center

itself (see Fig. 4.1). We also observe the coupling of the NV spin to the carbon nuclear spin bath, visible in spin-echo experiments at low magnetic field strength ($B \lesssim 150$ G) as periodic collapses and revivals of coherence spaced by the bare ^{13}C Larmor period, as expected [148].

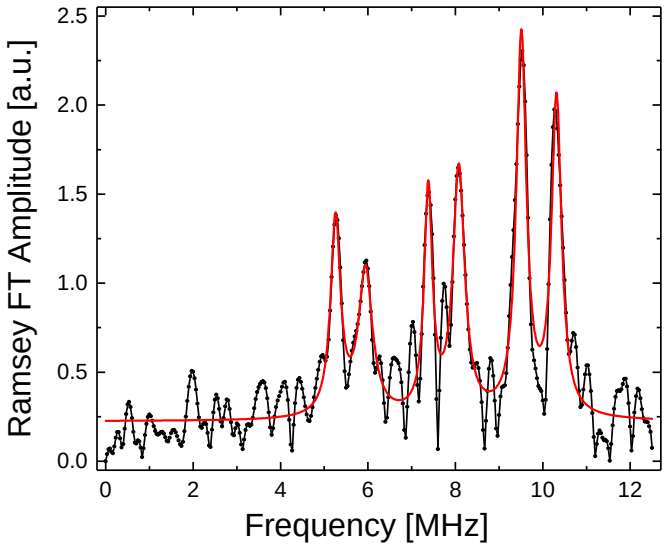

Figure 4.1: Fourier transform of a Ramsey measurement on the NV subject of NSD analysis. Experimental amplitude of the Fourier components as a function of frequency (black dots) and Lorentzian fit (red solid line) are shown. The six peaks correspond to the six components of the hyperfine structure: Each state correspondent to the ^{14}N triplet (with a splitting $A_{\parallel} = 2.16$ MHz) is divided in a doublet given by a ^{13}C nuclear spin, with a coupling strength (extracted from the fit) of 0.73 ± 0.07 MHz. Measurement performed with a static magnetic field $B \sim 80$ G.

To measure the NSD (see Sec. 4.3), we measured the spin coherence under sequences of π pulses separated by a time delay $2t_1$, using the XY-8 sequence [70, 177] as a base cycle, as in Fig. 1.7. We verified that applying the $\pi/2$ pulses along Y improves coherence with respect to using $\pi/2$ pulses along X. Even under these circumstances I maintain the sequence nomenclature of XY throughout the text. In all the experiments, we also average the signal over two measurements where the last $\pi/2$ rotation is applied respectively along Y and $-$Y, to improve reproducibility of the signal. The sequences of the XY family are designed to improve robustness against detuning and imperfections on the shape of the π pulses. As usual, the Ramsey interferometer maps residual coherence after the spin manipulation into the

observable population p_n of the $m_s = -1$ spin projection. We collected data for a large set of t_1 values ($0.15 - 6.5\,\mu$s), and repeated each measurement for different number of pulses, typically multiple of $n = 8$ [1].

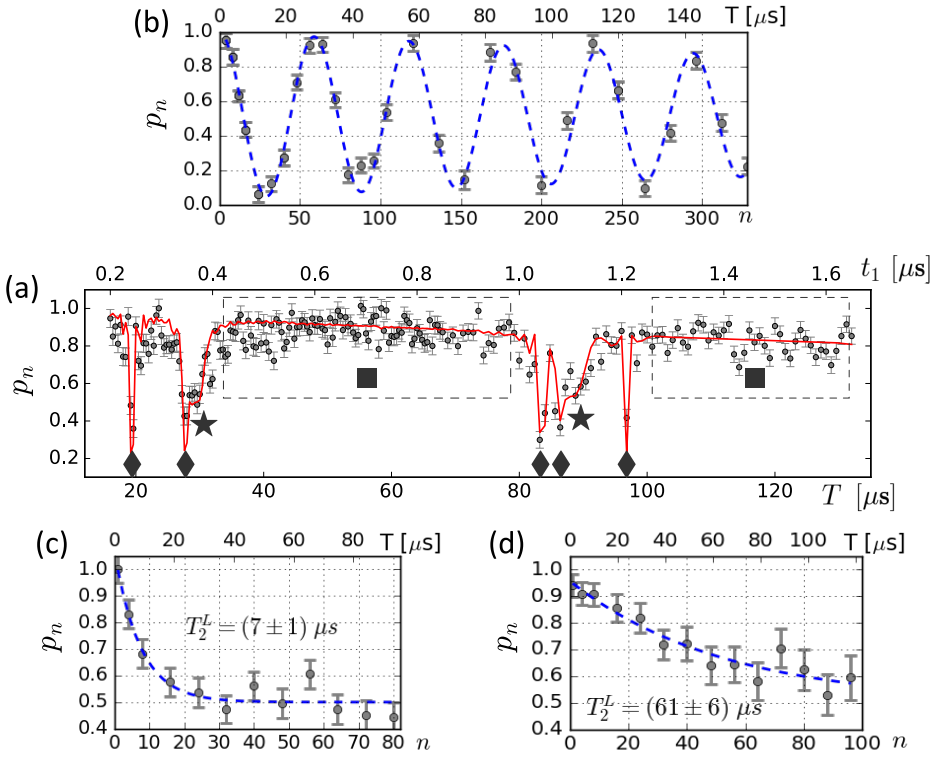

Figure 4.2: Evolution of p_n under an XY-8 sequence for a $|0\rangle \leftrightarrow |-1\rangle$ system. **(a)** Varying the time between pulses, with $n = 40$. Black dots are experimental data for a static magnetic field $B = 635 \pm 1$ G, red solid line is a simulation of the evolution of the spin with the environment reconstructed as discussed in following Sections 4.3, 4.4 and 4.6. **(b-d)** Varying the number of pulses, fixing t_1 to the center of a ♦ collapse (b), a ★ collapse (c) and a ■ flat region (d).

By combining the data sets associated to each t_1 value, we separated the contribution of different noise frequency components $\omega = \pi/2t_1$. We then categorized the coherence behavior as a function of n into two different cases: Decay and modulation, as presented on Fig. 4.2(a), (c-d). For most of the range of t_1, we observe an exponential decay of coherence, which is faster for t_1 around the coherence collapses, due to the semi-classical coupling with the spin bath. For certain t_1, coherence also presents sharp peaks with an amplitude that oscillates as a function of n, even going to negative values

[1] For t_1 values with coherence showing a fast decay, we also included $n = 1, 4$, and 12.

($p_n < 0.5$). These coherent modulations arise from the coupling with single nuclear spins. With this method, we detected at least three nearby nuclei. We investigate these features for different intensities of a bias magnetic field aligned with the NV spin, as shown in Sec. 4.5.

4.3 Effect of the decoherence

To characterize the effect of the classic bath we measure the NSD via a systematic spectral analysis of coherence under DD sequences with an increasing number of equidistant pulses.

In the limit of a long spin evolution time, once fixed the inter-pulse delay time $2t_1$ (that is, for sufficiently large number of pulses n), the residual coherence $W(nt_1)$ decays with a generalized coherence time T_2^L [141], as

$$W(nt_1) \simeq \exp(-2nt_1/T_2^L). \tag{4.2}$$

For a given t_1, T_2^L is affected by the convolution of $S(\omega)$ with the filter function $Y_n(\omega)$. For long enough evolution time, T_2^L depends only on the spectral weight of the NSD at frequency ω (whereas the equispaced DD sequence filters out all the nearby noise components):

$$S(\pi/2t_1) \simeq \frac{\pi^2}{8\,T_2^L}. \tag{4.3}$$

Given the observed time evolution, which presents collapses and revivals of the signal, a practical protocol is to extract T_2^L as the characteristic coherence decay time for various t_1 values, in a window around the first collapse, where no additional modulations are observed. The inset of Figure 4.3(a) shows $1/T_2^L$ measured with this procedure (blue dots).

However, our experiments show that the coupling to the spin bath leads to very fast decay of the NV spin coherence for t_1 around the first collapse – where coherence is lost within $n < 8$, so that using large number of pulses is not possible. For low number of pulses the filter induces an additional broadening of the NSD. An accompanying issue is that XY-8 sequences can no longer be used for the measurement of T_2^L, but one needs to use alternative equidistant-pulse sequence, as CPMG or XY-4, which although robust enough for small n, might still introduce some pulse error effects.

Indeed, Eq. (4.2)-(4.3) offer only an approximated, idealized picture of our practical scenario. As depicted in App. B, since a sequence of equidistant π pulses acts on the spin evolution as a step modulation function $y_n(t)$ with periodic sign switches, its filter function $Y_n(\omega)$ is not a single δ-function, but

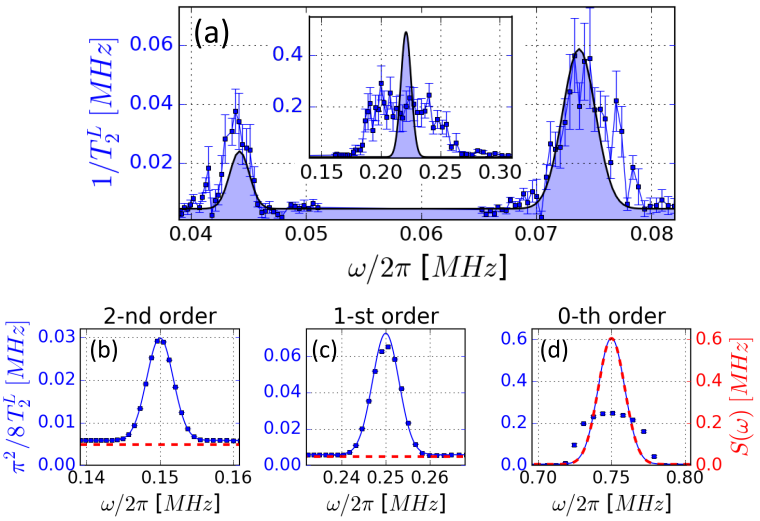

Figure 4.3: NSD evaluation for different filter orders. (a) The peaks of the 1^{st} and 2^{nd} harmonics. The blue points are the experimental data for $1/T_2^L$. The black line is the fit of Eq. (4.4) using as $S(\omega)$ a Gaussian curve. Inset: Data for the 0^{th} order $1/T_2^L$ peak, together with the fit extracted from higher harmonics. The data corresponds to an external magnetic field of (208±1) G. **(b-d)** Reconstruction of a model NSD (at $\sim$ 700 G), used to proof self-consistency of the used method. The blue squares are proportional to $1/T_2^L$, resulting from the fit of the simulated coherence. The blue line is the fit of the 1^{st} and 2^{nd} harmonics with Eq. (4.4) using a Gaussian distribution. The dashed red line is the original model NSD.

shows periodic sinc-shaped peaks at frequency $\omega_l = (2l+1)\pi/(2t_1)$, which can be well approximated by a periodic comb of δ-functions only for large n. Then, T_2^L is affected not only by the noise spectral weight (convoluted with the filter function) at frequency $\omega = \pi/(2t_1)$, but also by its higher harmonics [141, 142]:

$$\frac{1}{T_2^L(\omega)} = \frac{8}{\pi^2}\sum_{l=1}^{\infty}\frac{1}{(2l+1)^2}S(\omega_l). \tag{4.4}$$

This second observation gives us a simple tool to overcome the limitation of the short coherence decay time, and thus the small feasible number of pulses, in the collapses time windows. We can center the NSD maximum around the higher order harmonics of the filter function to partially attenuate strong noise that would saturate the coherence decay. In addition, the filter function gets narrower at higher orders, for a fixed number of pulses.

Simultaneously fitting different harmonics $l > 0$ results in a good estimation of the center and shape of the nuclear spin bath noise peak. In Fig. 4.3.a

Table 4.1: Comparison between original and reconstructed NSD peaks. The noise peak is defined by its center $\nu_L = \omega_L/(2\pi)$, amplitude A, width σ and offset y_0. The original parameters correspond to the dashed red line in Fig. 4.3.d and the parameters of the reconstructed NSD using the first two harmonics correspond to the blue line in the same figure. For the reconstruction, we simulated the coherence only for $n \geq 8$, including the points with $n < 8$ increases the percentage error on the estimated amplitude and width by a factor of 100 and 40, respectively. The estimation of the center was the same, within the error bars, in all cases.

	Original	Reconstructed		
		(0-th order)	(two harmonics)	(ten harmonics)
ν_L †	750	748(2)	750.0(2)	750.02(2)
A ‡	600	266(34)	601(13)	603(1)
σ †	9	21(4)	9.0(1)	9.01(2)
y_0 ‡	5	5.00(5)	5.860(4)	5.983(2)

† Values have units of kHz.

‡ Values have units of kHz^2/kHz.

we show an example of the noise peaks for $l = 1, 2$ fitted with Eq. (4.4) using a Gaussian noise distribution. The inset shows the data for the 0^{th}-order peak together with the corresponding curve predicted from the higher harmonics. We note that both the amplitude and width of the 0^{th}-order peak data are not compatible with the values predicted from the fit of higher harmonics.

To correctly interpret these experimental results, and reliably extract the NSD, we performed the same analysis starting from a simple model of noise, and we verified auto-consistency of the method. We considered a Gaussian noise ($S(\nu) = y0 + A\, e^{-(\nu-\nu_L)^2/(2\sigma^2)}$) centered at the Larmor frequency $\nu_L = \omega_L/(2\pi)$ of a carbon nuclear spin bath, for an external magnetic field of 700 G. We then calculated the temporal dependence of spin coherence under control sequences with different numbers of equidistant pulses (see Appendix B), and we used this coherence to reconstruct the original NSD with the same procedure used to treat the experimental data. As shown in Fig. 4.3(d), the 0^{th} order peak of the reconstructed spectrum shows the same trend of the experimental data (inset of Fig. 4.3(a)), and significantly deviates from the original spectrum. Our analysis shows that using only the first two harmonics we can reliably reconstruct the NSD peak. We also performed the same analysis taking the first ten harmonics, with similar results. The four parameters that define the noise peak are listed in Tab. 4.1, for the original noise peak and for the reconstructed ones. By comparing the reconstructed

spectra with two and ten harmonics, it is possible to note that they are strongly compatible between each other. Moreover, with the exception of the offset y_0, they can reconstruct the original version of the NSD: This means that consider $l = 1, 2$ is sufficient to extract a complete information on the noise components, overcoming the (still present) limitations related to spectroscopy based on dynamical decoupling [178].

4.4 Coupling with single nuclei

The reconstruction of NSD fails at some narrow time intervals, but this allows us to identify the coherent coupling of the NV spin qubit to other quantum systems. Because the equispaced DD sequences partially filter out the spin bath, we can observe the effect of single proximal nuclear spins, provided that their coupling strength to the NV electronic spin is large enough to be distinguished from the bath itself. This hyperfine interaction reads $H_{hf} = \hbar S_z \boldsymbol{\omega}_h \cdot \boldsymbol{I}$, where S_z is the electronic spin operator, $\boldsymbol{I}$ is the nuclear spin operator (in this case, a ^{13}C: $I_C = 1/2$), and $\boldsymbol{\omega}_h/(2\pi)$ is the hyperfine coupling vector frequency. This interaction induces different phase acquisition of the states $|\pm\rangle = (|0\rangle \pm |1\rangle)/\sqrt{2}$ during the spin evolution time [149, 151, 179], and thus modulates the residual NV spin coherence in terms of the number of pulses, as shown in Fig. 4.2(a).

The time evolution of the qubit coherence under the effect of a single nuclear spin can be calculated as [180]:

$$M(T) = \mathrm{Tr}\left(U_0 U_1^\dagger\right), \tag{4.5}$$

where $U_0 = \cdots e^{-iH_0 t_3} e^{-iH_1 t_2} e^{-iH_0 t_1}$, and $U_1 = \cdots e^{-iH_1 t_3} e^{-iH_0 t_2} e^{-iH_1 t_1}$. Here t_i is the free evolution time between two consecutive microwave pulses. $H_{0(1)}$ is the Hamiltonian that describes the interaction between the $m_s = 0(+1)$ electron spin and a nearby ^{13}C nucleus [149]:

$$H_0 = \omega_L \sigma_z, \tag{4.6}$$

$$H_1 = (\omega_h^{\parallel} + \omega_L)\sigma_z + \omega_h^{\perp}\sigma_x, \tag{4.7}$$

where σ_i are the Pauli matrices related to the nuclear spin operator. This treatment allows us to simulate $M(T)$ under different kinds of DD sequences.

To experimentally determine the components of the coupling strength, $\omega_h^{\parallel}$ and $\omega_h^{\perp}$, we used an analytic expression for $M(T)$ valid for an even number of equidistant pulses n

$$M = 1 - 2\left(\frac{\omega_h^{\perp}}{\omega_1}\right)^2 \sin^2\left(\frac{\omega_1 t_1}{2}\right) \sin^2\left(\frac{\omega_L t_1}{2}\right) \frac{\sin^2\left(\frac{n\phi}{2}\right)}{\sin^2\left(\frac{\phi}{2}\right)}, \tag{4.8}$$

where $\omega_1 = \sqrt{(\omega_h^{\parallel} + \omega_L)^2 + (\omega_h^{\perp})^2}$ is the frequency seen by the spin in the $m_s = +1$ state, and the phase ϕ is the modulation frequency of the transition probability as a function of n, given by

$$\cos\phi = \frac{\omega_h^{\parallel} + \omega_L}{\omega_1} \sin(\omega_1 t_1) \sin(\omega_L t_1) - \cos(\omega_1 t_1) \cos(\omega_L t_1) \,. \tag{4.9}$$

We observe that ϕ is small for times t_1 corresponding to the minimum values of M.

Note that equations (4.8) and (4.9) are already present in literature in Refs. [149, 179], with the simple transformation $\phi \to \phi' = \pi - \phi$. Both of these conventions are consistent with the model and suitable to evaluate the two components of the hyperfine strength, because they assume the same M values for even integer n; nonetheless, they result in a very different periodicity of p_n as a function of n, as shown in Fig. 4.4, making the analysis of the data very different in terms of the convergence of the fit.

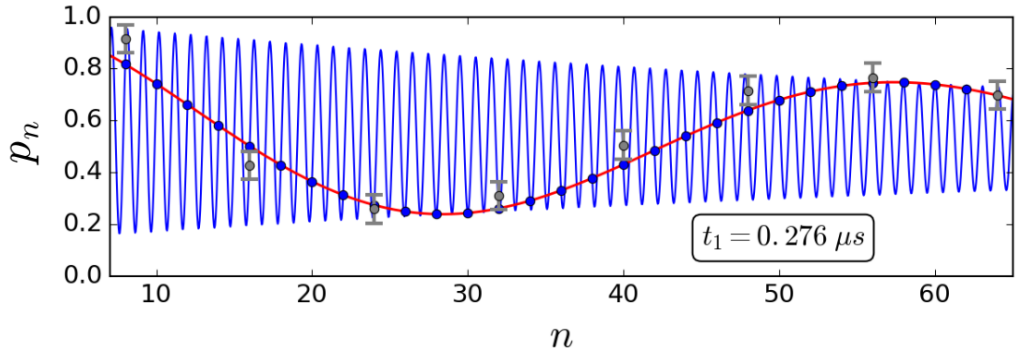

Figure 4.4: Probability p_n of the electronic spin to be in the state $|-1\rangle$, in terms of the number of n (external bias field $B = (528 \pm 1)$ G). The gray points are the experimental data, the blue and red solid lines are obtained from fit when considering ϕ and ϕ', respectively (see text). The blue points show the intersection points of the two curves with even n values.

The analysis of this modulation gives information on the coupling strength and relative orientation of the NV spin to nearby nuclear spins [149, 179]. In our specific case, for a $|0\rangle \leftrightarrow |-1\rangle$ system, the amplitude of the modulation shows sharp peaks (red dots in Fig. 4.6), from which we can identify three different carbon nuclei coupled to the NV. The frequency position of each peak give an approximate estimation of the parallel component of the coupling strength of a nuclear spin to the NV axis, $\omega_h^{\parallel}$ [149]. We use this value as the initial guess to fit the observed modulation using Eq. (4.8), with $\omega_h^{\parallel}$ and

$\omega_h^{\perp}$ as free parameters (blue dashed line in Fig. 4.6(b)). We thus extract a refined estimation of the parallel and orthogonal components of the coupling strength, as shown in Table 4.2. Note that we treat each coupling separately, since intraspin couplings are found to be negligible.

Table 4.2: Components of the coupling strength of the three ^{13}C nuclei detected with the NV spin.

$\omega_h^{\parallel}/(2\pi)$ [kHz]	$\omega_h^{\perp}/(2\pi)$ [kHz]
-698 ± 8	148 ± 13
-73 ± 4	59 ± 3
-25 ± 2	42 ± 1

Two of the three observed nuclei are so weakly coupled that they are not visible in an usual Ramsey experiment. The more strongly coupled nucleus is visible with a Ramsey experiment, which still gives a consistent but less precise estimation of the coupling strength, due to decoherence.

It is also important to note that the sign of the hyperfine interaction is dependent on the electronic spin projection $m_S = \pm 1$. This leads to change the sign of ω_h components in Eq. (4.7). For this reason, if we have the case $\omega_h^{\parallel} \sim \omega_L$, the parallel component in ω_1 ($\omega_h^{\parallel} \pm \omega_L$) would pass from an amplitude $\sim 2\omega_L$ to another one close to 0, strongly influencing ϕ in Eq. (4.9) [2]. Therefore, we can exploit the spin triplet nature of the NV center to validate the fact that the reconstructed environment model is predicted independently of the qubit properties, that is, the environment model extracted from the dynamics of the the two spin states $|0\rangle$ and $|-1\rangle$ can predict also the dynamics of the $m_S = \{0, +1\}$ manifold and not only the $\{0, -1\}$ manifold as presented in Fig. 4.2. Figure 4.5 shows two different sequences for the two different electronic spin projections together with their simulations, that take into account also the correspondent NSD. In both cases we found a good agreement between the prediction and the experimental data.

4.5 Characterization with the external field

We used the method described in the previous two sections, to extract information about the NSD and the coupling strength with nearby nuclei, for different intensities of the magnetic field. However, I underline that, meanwhile the spin bath can always be treated as a classic noise source [175], a

[2] The orthogonal component of ω_1 (equivalent to $\omega_h^{\perp}$) is a different case: Since it appears always on the second order, its sign does not influence Eq. (4.9) and (4.8).

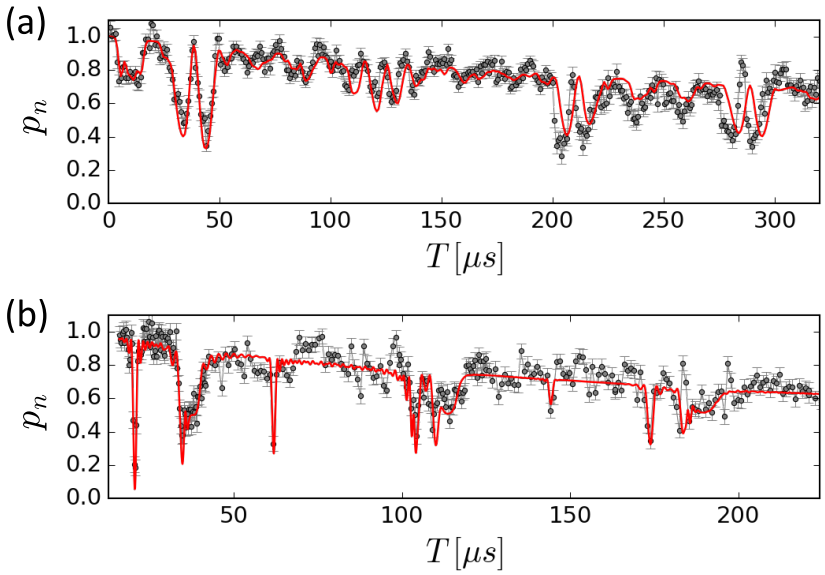

Figure 4.5: Time evolution of spin coherence at field $B = (394 \pm 1)$ G. The dots are the experimental data, and the red line is the simulation, in both cases the prediction was done using the same environment, *i.e.* same NSD and same nearby nuclei coupling strengths. (a) Two level system formed by $\{|0\rangle, |+1\rangle\}$. Sequence: One repetition of XY-4 ($n = 4$). (b) Two level system formed by $\{|0\rangle, |-1\rangle\}$. Sequence: Four repetitions of XY-8 ($n = 32$).

single central spin model is feasible only if most of the nuclei composing the bath are weakly coupled with the NV spin, that is, the condition $\gamma_e B \gg \omega_h$ has to be verified [146]. Below that limit, the interaction with the nuclear spin ensemble exhibits peculiar quantum properties and more than one classical model is necessary to describe the evolution of the NV electron spin under different control sequences. In case of diamonds with natural abundance of ^{13}C nuclei, the classical limit results verified for $B \geq 150$ G. For an in-depth study is possible to refer to [168].

The obtained NSDs are shown on Fig. 4.6 and their parameters are listed on Table 4.3. As expected, the center of the NSD peak shows a linear dependence with the magnetic field, having the gyromagnetic ratio $\gamma_N = 2\pi \times 1.08$ kHz/G of the ^{13}C as proportional constant. The position in frequency of the modulations due to the coupling to nearby carbons follows the same trend. On the other hand, the width of the noise peak increases with the intensity of the magnetic field whilst the height of the noise peak decreases: For a detailed analysis of this phenomenon, it is possible to refer to [168].

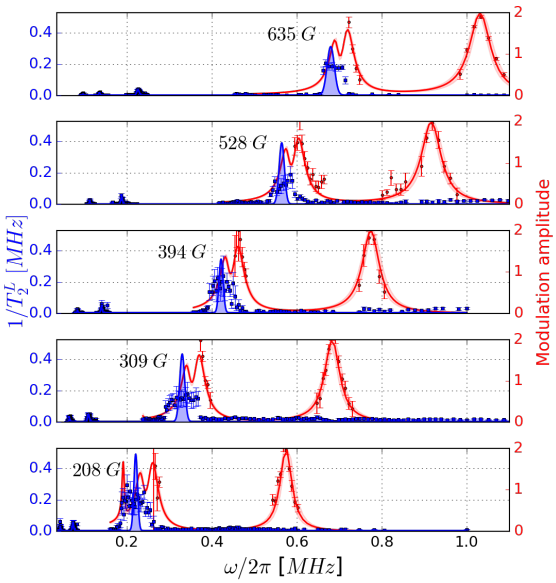

Figure 4.6: NSD and coupling with nearby nuclei varying the magnetic field amplitude. We report $1/T_2^L$ (blue, left-hand side vertical scale) and the amplitude of the observed coherent modulations (red, right-hand side vertical scale), for magnetic field strengths $B = 208 - 635$ G. The blue lines are the fit of high-order harmonics (see text). The red lines are the results of simulation (see Sec. 4.4). The red shadow describes the uncertainty on the estimation of the coupling strength components.

Table 4.3: Parameters obtained for the NSD peak ($\nu_L = \omega_L/(2\pi)$) using only the 0-th order collapse and using higher harmonics.

B [G]	Just 0-th order				Higher orders: 1st & 2nd			
	$y_0^\star$	$A^\ddagger$	$\nu_L^\dagger$	$\sigma^\dagger$	$y_0^\star$	$A^\ddagger$	$\nu_L^\dagger$	$\sigma^\dagger$
635*	19.1(7)	0.35(8)	683(3)	18(2)	3.7(2)	0.38(5)	679.9(8)	8.5(7)
528	17.4(8)	0.16(3)	571(2)	19(2)	4.0(3)	0.48(7)	564.7(7)	6.2(6)
394	14.4(7)	0.25(4)	425(2)	17(1)	6.1(3)	0.42(6)	422.0(6)	4.8(5)
309	26.0(8)	0.21(3)	331(2)	18(1)	7.0(6)	0.53(7)	330.6(6)	5.9(5)
208	16(1)	0.29(2)	223(1)	18.7(8)	5.6(4)	0.60(8)	221.2(4)	4.3(4)

‡ Values have units of MHz^2/MHz. * Values have units of kHz^2/kHz.
† Values have units of kHz.
* For 635 G we also used the 3rd order harmonic.

4.6 Non-periodic decoupling

In principle we have extracted all the information on noise spectrum and coherent interaction with nearby impurities. To confirm that we have a full picture of the NV spin environment, now we want to predict the spin evolution under different kinds of time-dependent control. Until now we have used equidistant pulses to measure the NSD and the hyperfine coupling strength of nearby nuclei, at different magnetic fields, mainly because these sequences are associated with a δ-shaped filter function [7]. However, our characterization of the noise should be useful for any kind of sequence. To prove the robustness of our method, we use the measured spectrum and hyperfine couplings to simulate the spin coherence under other kind of DD sequences, and we compared this prediction with measurements.

The simulation calculates the residual coherence after the pulse sequence, p_n. As the spin dynamic is affected by both the spin bath and m strongly-coupled single spins, we expect p_n to reflect those two contributions:

$$p_n(T) = \frac{1}{2}\left(1 + e^{-\chi_n(T)} \prod_{i=1}^{m} M_n^{(i)}(T)\right). \tag{4.10}$$

Here, $\chi_n(T)$ is obtained from the measured NSD via Eq. (4.1), whereas $M_n(T)$ is extracted by evolving the spin under conditional evolution operators, as discussed in Sec. 4.4.

Nonuniformly-spaced π-pulse sequences [74, 154] have been designed to improve resolution of single nuclear spin spectroscopy. A first important example is represented by Uhrig-DD (UDD) sequence [72], recently used to detect remote dimers formed by couples of nuclei [162], while suppresses the effect of the coupling of the NV spin with single nearby nuclei, which only results in a fast and small modulation. Results about the capability to predict the NV spin evolution under UDD with our reconstructed environment can be found in [168].

Here, I discuss a different type of non-equidistant sequences, that is, adaptive XY-$\mathcal{N}$ (AXY-$\mathcal{N}$) [73]. They have been proposed to enhance robustness by sending the pulses along different axes within each other. AXY-8 is constructed by eight blocks, each containing five equidistant pulses with specific phases – known as Knill pulse [73, 181]. The phase distribution of the pulses in each block is:

$$\Pi_\varphi = \pi_{\varphi+\pi/6} - \pi_\varphi - \pi_{\varphi+\pi/2} - \pi_\varphi - \pi_{\varphi+\pi/6}. \tag{4.11}$$

Including 8 blocks alternating their phase as in Fig. 4.7 we produce a AXY-8 sequence. The blocks are themselves equidistant, thus the position in time

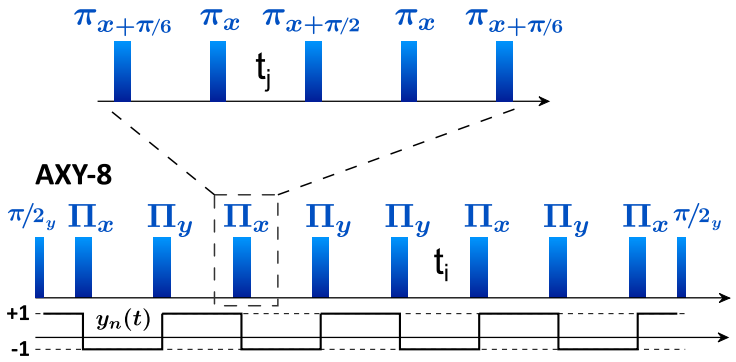

Figure 4.7: Scheme of adaptive XY-8 sequence.

for each π pulse is given by

$$t_{i,j}(r_m) = \frac{T}{\mathcal{N}}\left(\frac{2i-1}{2} + r_m\frac{2j-\mathcal{M}-1}{2\mathcal{M}}\right), \tag{4.12}$$

where $\mathcal{M}$ is the number of pulses inside each nest ($\mathcal{M} = 5$ in this case), $i \in \{1,\ldots,\mathcal{N}\}$, $j = \{1,\ldots,\mathcal{M}\}$, and r_m is a parameter that defines how close within each other are the pulses inside each nest. For example, with $r_m = 1$ the 40 pulses are equidistant, and in the limit of $r_m = 0$ we would have only eight π pulses (each one formed by the superposition of five pulses). As we can see, this kind of sequence is characterized by two different time constants: The inter-block interval t_i and the intra-block one t_j.

The comparison between simulation of p_n, performed without any fit parameter, and experimental data is shown in Fig. 4.8. First of all, Fig. 4.8(a) shows one of the sequences used to characterize the noise – a concatenation of XY-8 sequences, with $n = 32$ π pulses. In Fig. 4.8(b) and (c) I present the cases for AXY-8 sequence (i.e. $n = \mathcal{N}\mathcal{M} = 40$) with $r_m = 0.5$ and 0.25, respectively, which exhibits a good agreement for different values of the parameter r_m. We noted that, as expected, AXY-8 and XY-8 are more robust compared to CPMG and XY-4 against detuning and pulse shape imperfections, which our simulations do not take into account.

4.7 Results summary

To summarize, we have experimentally demonstrated a method to spectrally characterize the nuclear spin environment of NV centers, even when the resulting NV coherence time is short. The environment comprised both nearby nuclei, that induce coherent modulations, and a larger ensemble of nuclear spins, which we aim to model with a classical bath. Our method allows

identifying the characteristic parameters of both components of the environment (Hamiltonian of nearby nuclei and NSD of the bath). The method thus empowers the reconstruction of a full environment model that can be also used to predict the NV coherence even when the spin dynamics is driven by different kinds of control.

For high bias magnetic fields, we found remarkable agreement between the expected behavior predicted by the environment model and the measured spin coherence under various control sequences. This shows that the extracted environment model has not only descriptive, but also predictive power. The latter ability would represent a considerable enhancement of the optimal control method presented in Ch. 3, enabling the extension of the optimal sensitivity search with a wider space of control parameters, as, for instance, sequences with different number of π pulses.

Even if I did not explore the case, we can further tune the ratio between the environment internal energy and its coupling to the NV center by varying the strength of an applied external magnetic field, thus exploring different bath regimes [146]. For rather low magnetic field, where the quantum dynamics of the carbon nuclear spins is expected to have larger influence, the intrinsic quantum nature of the bath cannot be neglected; nevertheless, it has been demonstrated that we could identify a classical noise model describing the NV central spin decoherence [168], even if decoherence is fundamentally induced via bath-NV center entanglement. However, a univocal classical noise model is not sufficient, and we verified instead that different environment models are needed to describe the evolution under different types of applied controls.

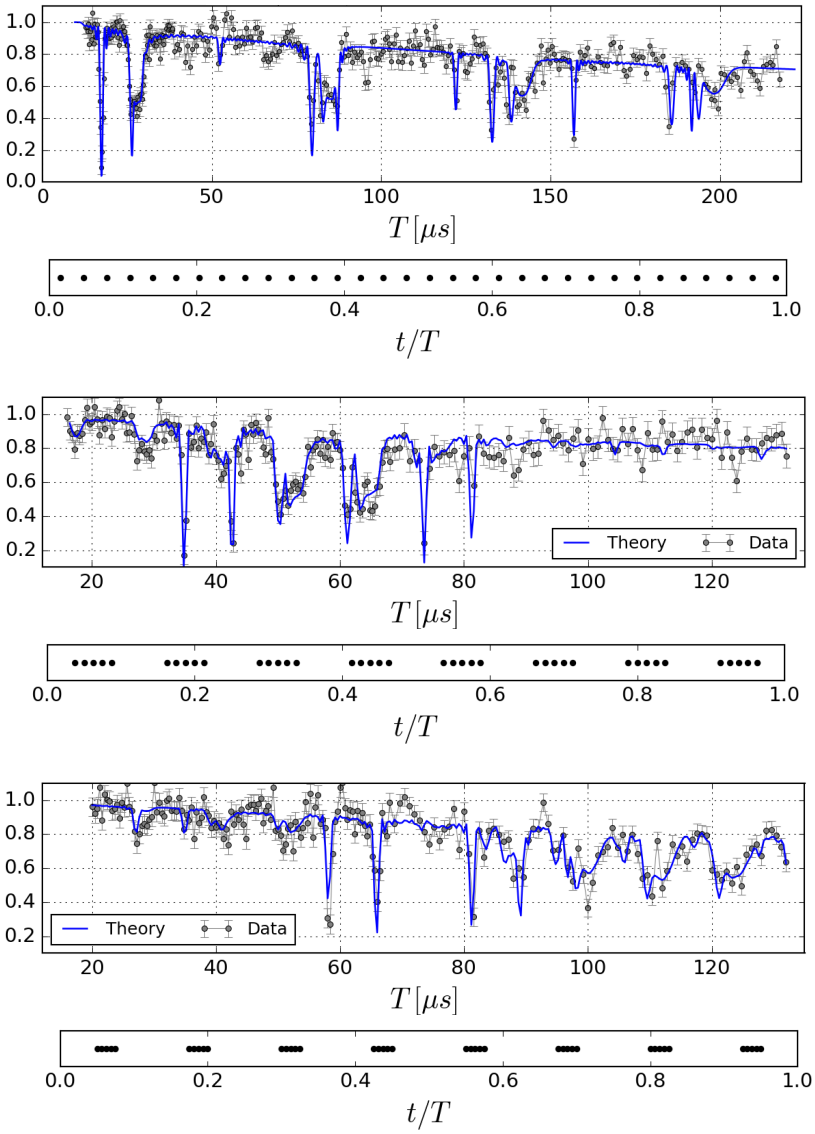

Figure 4.8: Time evolution of the coherence under different DD sequences. (a) Four repetitions of XY-8 ($n = 32$ pulses) at $B = (528 \pm 1)$ G. **(b-c)** Adaptive XY-8 with a total of $n = 40$ pulses but with different spacing between subsequences corresponding to $r_m = 0.5$ and 0.25 (see text), at $B = (635 \pm 1)$ G. Dots represent the experimental data with statistical error. Blue lines are the predicted coherence under the effect of the measured environment given by both pure quantum and semi-classical contributions, with no free parameters. The mean squared residuals ($\chi^2 = 1/N$) is, respectively, (a) $\chi^2_\nu = 3.8$, (b) $\chi^2_\nu = 2.2$ and (c) $\chi^2_\nu = 4.1$. Below each plot, the distribution of the π pulses is shown.

Conclusions and perspectives

In conclusion, the goal of my Ph.D. work was represented by the experimental implementation of quantum control techniques for the spins associated to single NV centers. To achieve it, the preliminary step was the completion of the existing experimental setup and the engineering of measurement routines for the control of the static magnetic field, and electronic and nuclear spin degrees of freedom. The main scientific results, discussed in depth in Chapters 2, 3 and 4, could be schematically summarized as:

- Study of the nuclear spin polarization of nitrogen and characterization of its dynamics [83]
- Optimal control of the NV electronic spin for quantum sensing [122]
- Characterization of the NV-environment interactions: Coherent coupling with nearby ^{13}C nuclei and "classical" spin bath [168]

The core of all these three projects was the development of new measurement protocols, aimed for the initialization of a fiducial state with high fidelity, and to enhance the quality of a quantum measurement, as achieving a better sensitivity for ultraweak magnetic field sensing. To this purpose, the characterization of the environment is a fundamental ingredient for the protection of the qubit from external perturbations. Therefore, this work represents a step for further measurement techniques implementations and opens new direct perspectives.

In the short term, the first possible extension could be to improve our optimal control technique including the environment reconstruction, that takes into account both the nuclear spin bath and the coherent interaction with strongly coupled nearby nuclei. Although this would complete the model, we need to consider a possible increase of the cost-to-benefit ratio for the computational sources for the evaluation of the optimal sequence that minimizes the sensitivity.

A second interesting outlook of the present dissertation is the further investigation about the possible presence of a transition between a quantum

and classical regime of coupling between the qubit and the spin bath inside the diamond, as recently proposed in [182]. Experimentally, this would require to extend the study of the noise spectral density as a function of a tunable parameter, e.g. the external magnetic field amplitude or the nuclear spin impurities concentration. The characterization close to the quantum-classical cross would shed new light on the description of the NV-environment interaction.

As a mid term perspective, we can extend the study of optimal control applied to sensing. We note that the optimal control that we implemented corresponds to an open-loop optimization scheme, where the (arbitrary) spectral composition of the variable magnetic field is known and the optimization of the sequence is a preliminary process before starting to measure. The combination of our technique with methods for spectral reconstruction, as Walsh sequences [183], can be a crucial target for its generalization. Another important extension would be also implementing and testing a closed-loop optimization [107], i.e. exploiting the output of the measurements as input for the algorithm [184] to find the best sensitivity, or performing coherent feedback control [19, 185].

In order to develop applications, would also be interesting to integrate and test our optimization protocol on different experimental platforms, as shallow NVs [44, 75] or nano-diamonds [24]. They would allow us to check the improvement given by optimal control for magnetic field sensing in practical scenarios, as the detection of paramagnetic molecules [25] or weak signals in biological samples [26, 27].

Appendix A

Effects of the Laser Excitation Power on DNP

The optical power used to excite from the ground to the excited levels set the rate of the process and strongly influences the time evolution of the population of the hyperfine sublevels of the electronic ground-state. To discuss its role, we introduce the optical pumping parameter W. Since we consider the relaxation rate via the spin-conserving radiative decay channel to be spin-independent (i.e., $\Gamma = \Gamma_{0e,0g} = \Gamma_{-1e,-1g} = \Gamma_{+1e,+1g}$), and the optical pumping rates from the ground to the excited level to be proportional to the corresponding relaxation rates [53], we define $W = \Gamma_{ij}/\Gamma_{ji}$, with $i = 0g, -1g, +1g$, and $j = 0e, -1e, +1e$.

In Fig. A.1 we characterize the time evolution of the populations $p_{0,+1}$ of three hyperfine states $|0,0\rangle_g$ and $|0,\pm1\rangle_g$ as a function of W, for a typical value of magnetic field ($B = 249$ aligned along $\theta = 2.1°$). Figure A.1 (a) shows the theoretical curves obtained from the solutions of the generalized Liouville equation described in Sec. 2.4 with $C_\perp = -23$ MHz, and compare them with the experimental data obtained with optical excitation at the saturation power. From the exponential fit of the theoretical curves we obtain the characteristic rise-time τ_{+1} of the population of the hyperfine state $|0,+1\rangle_g$, and the decay-times τ_0 and τ_{-1} of the population of $|0,0\rangle_g$ and $|0,-1\rangle_g$, respectively. We observe that the characteristic times $\tau_{0,\pm1}$ drop logarithmically when increasing the pumping parameter W, as shown in Fig. A.1 (b).

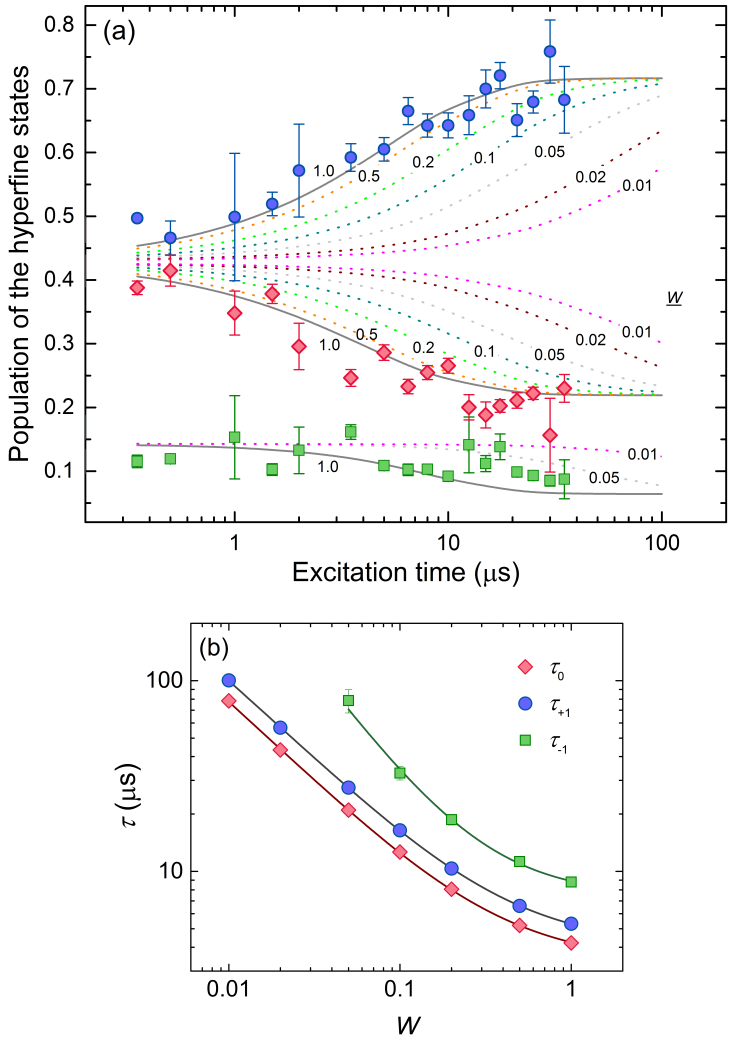

Figure A.1: Analysis of DNP as a function of the laser excitation power. **(a)** Time-evolution of the populations of the hyperfine sublevels of the electronic ground-state, for a magnetic field $B = 249$ G aligned along $\theta = 2.1°$. The points are the experimental results obtained for NV2, with laser excitation at saturation power (blue dots, population of $|0,+1\rangle_g$; red diamond, $|0,0\rangle_g$; green squares, $|0,-1\rangle_g$). The curves are obtained from the solutions of the generalized Liouville equation with $C_\perp = -23$ MHz, for different excitation rates $W\Gamma$. The solid line corresponds to $W = 1$, *i.e.*, to the excitation rate at saturation power. The dotted lines refer to $W = 0.01, 0.02, 0.05, 0.1, 0.2$, and 0.5, as denoted in the Figure. For $W \geq 1$, we do not observe further changes in the population dynamics. **(b)** Characteristic rise-time τ_{+1} of the population of the state $|0,+1\rangle_g$ (blue dots), and decay-times τ_0 and τ_{-1} of the population of the state $|0,0\rangle_g$ (red diamonds) and $|0,-1\rangle_g$ (green squares) as a function of the pumping rate parameter W, in log-log scale. The curves are logarithmic fit of $\tau_{0,\pm1}$.

Appendix B

Filter function picture

As introduced in Sec. 1.6, under the effect of a spin bath the time evolution of the electron spin can be described by the temporal coherence function $\chi_n(T)$ defined on Eq. (1.11), which depends on the NSD and on the specific filter control function $|\mathcal{Y}_{n,T}(\omega)|^2$. In particular, $\mathcal{Y}_{n,T}(\omega)$ represents the Fourier transform of the modulation function $y_n(t)$ and has a simple form for any pulsed sequence of dynamical decoupling, which is realized with series of n π pulses that repeatedly flip the spin, thus reversing its time evolution. The control field can be thus described by considering $y_n(t)$ as a sign switch at the position of each π pulse, indicating the direction of time evolution, forward or backward.

In these circumstances, recalling the filter function definition in Eq. (1.12)

$$\mathcal{Y}_{n,T}(\omega) = \int_0^T y_n(t) e^{i\omega t}\, dt, \tag{B.1}$$

it is possible to redefine $Y_{n,T}$ in order to put in evidence $1/(i\omega)$ and obtain

$$Y_{n,T}(\omega) = \mathcal{Y}_{n,T}(\omega) \cdot i\omega = 1 + (-1)^{n+1}\, e^{i\omega T} + 2\sum_{j=1}^{n} (-1)^j\, e^{i\omega\delta_j}, \tag{B.2}$$

where δ_j is the j-th π-pulse timing, and the pulses are assumed to be instantaneous. For some relevant pulsed sequences it is possible to find an analytic expression for Eq. (B.2), recalled in Tab. B.1 for sake of clarity.

As example, in Fig. B.1 I present the case of a CPMG sequence with $n = 12$ and inter-pulse spacing $\tau = 2$ μs: The corresponding modulation function is shown, as well as the filter function amplitude as a function of the frequency. In the limit of large pulse numbers, the filter function can be approximated by a δ-function at the angular frequency π/τ; I point out that the actual filter width scales as $1/(n\tau)$ and the limit of the δ-function

Table B.1: $Y_{n,T}(\omega)$ for Ramsey-free induction decay (FID), spin-echo (SE), periodic dynamical decoupling (PDD), and Carr-Purcell-Meiboom-Gill (CPMG) [7, 133].

Sequence	$\lvert Y_{n,T}(\omega)\rvert^2$
FID	$2\sin^2\left(\frac{\omega\tau}{2}\right)$
SE	$16\sin^4\left(\frac{\omega\tau}{4}\right)$
PDD (odd n)	$4\tan^2\left(\frac{\omega\tau}{2n+2}\right)\sin^2\left(\frac{\omega\tau}{2}\right)$
CPMG (even n)	$8\left[\sec\left(\frac{\omega\tau}{2}\right)\sin\left(\frac{\omega n\tau}{2}\right)\sin\left(\frac{\omega\tau}{4}\right)\right]^2$

approximation becomes relevant for regimes with high noise amplitude, as discussed in Ch. 4. Although the π-pulses phases are crucial to engineer sequences in order to correct for pulses imperfections, it is also important to note that they are not relevant for the filter modeling.

Finally, the probability $p_n(T)$ of the state $m_S = 0$ can be then obtained from $\chi_n(T)$ as

$$p_n(T) = \frac{1}{2}\left(1 \pm e^{-\chi_n(T)}\right), \tag{B.3}$$

where the sign is determined depending on the total, even ($-$ sign) or odd ($+$ sign), number of π pulses with the same phase of the $\pi/2$ pulses characterizing the Ramsey interferometer.

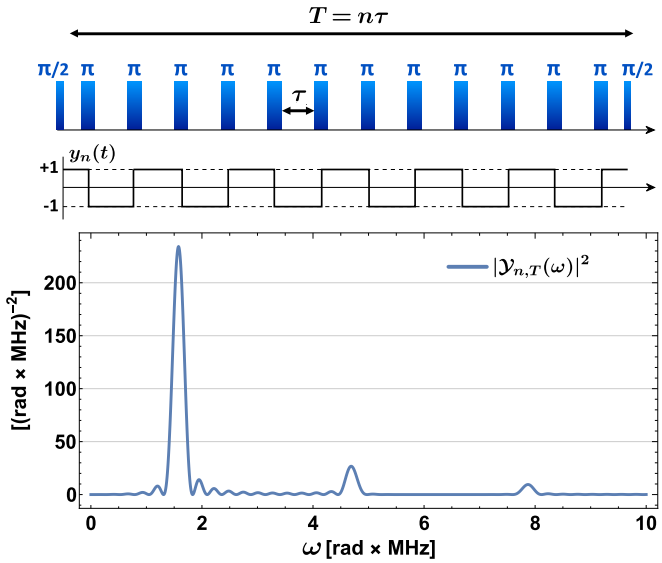

Figure B.1: Modulation and filter functions of a CPMG multi-pulse sequence. A CPMG sequence, with $n = 12$ π pulses and total time $T = n\tau$, is represented together with the correspondent modulation function. The bottom graph shows a simulation for the filter function $|\mathcal{Y}_{n,T}(\omega)|^2$ as a function of the angular frequency for an inter-spacing $\tau = 2$ μs.

Bibliography

[1] P. Shor, "Polynomial-time algorithms for prime factorization and discrete logarithms on a quantum computer," *SIAM Journal on Computing*, vol. 26, no. 5, pp. 1484–1509, 1997. [Online]. Available: https://doi.org/10.1137/S0097539795293172 1

[2] C. M. Caves, "Quantum-mechanical noise in an interferometer," *Phys. Rev. D*, vol. 23, pp. 1693–1708, Apr 1981. [Online]. Available: http://link.aps.org/doi/10.1103/PhysRevD.23.1693 1

[3] R. P. Feynman, "Simulating physics with computers," *Inter. J. Th. Phys.*, vol. 21, no. 6-7, pp. 467–488, 1982. [Online]. Available: http://dx.doi.org/10.1007/BF02650179 1

[4] V. Giovannetti, S. Lloyd, and L. Maccone, "Advances in quantum metrology," *Nat. Photon.*, vol. 5, no. 4, pp. 222–229, 2011. [Online]. Available: http://dx.doi.org/10.1038/nphoton.2011.35 1, 47

[5] D. P. DiVincenzo, "The physical implementation of quantum computation," *Fortschr. Phys.*, vol. 48, pp. 771–793, 2000. 1

[6] T. D. Ladd, F. Jelezko, R. Laflamme, Y. Nakamura, C. Monroe, and J. L. O'Brien, "Quantum computers," *Nature*, vol. 464, no. 7285, pp. 45–53, Mar. 2010. [Online]. Available: http://dx.doi.org/10.1038/nature08812 2, 5

[7] C. L. Degen, F. Reinhard, and P. Cappellaro, "Quantum sensing," *Rev. Mod. Phys.*, vol. 89, p. 035002, Jul 2017. [Online]. Available: https://link.aps.org/doi/10.1103/RevModPhys.89.035002 3, 4, 23, 47, 59, 86, 95

[8] I. K. Kominis, T. W. Kornack, J. C. Allred, and M. V. Romalis, "A subfemtotesla multichannel atomic magnetometer," *Nature*, vol. 422, pp. 596 EP –, Apr 2003. [Online]. Available: http://dx.doi.org/10.1038/nature01484 4

[9] M. P. A. Jones, C. J. Vale, D. Sahagun, B. V. Hall, and E. A. Hinds, "Spin coupling between cold atoms and the thermal fluctuations of a metal surface," *Phys. Rev. Lett.*, vol. 91, p. 080401, Aug 2003. [Online]. Available: https://link.aps.org/doi/10.1103/PhysRevLett.91.080401 4

[10] T. W. Kornack, R. K. Ghosh, and M. V. Romalis, "Nuclear spin gyroscope based on an atomic comagnetometer," *Phys. Rev. Lett.*, vol. 95, p. 230801, 2005. [Online]. Available: http://link.aps.org/doi/10.1103/PhysRevLett.95.230801 4

[11] R. L. Fagaly, "Superconducting quantum interference device instruments and applications," *Review of Scientific Instruments*, vol. 77, no. 10, p. 101101, 2006. [Online]. Available: https://doi.org/10.1063/1.2354545 4

[12] M. Bal, C. Deng, J.-L. Orgiazzi, F. Ong, and A. Lupascu, "Ultrasensitive magnetic field detection using a single artificial atom," *ncomms*, vol. 3, pp. 1324–, Dec. 2012. [Online]. Available: http://dx.doi.org/10.1038/ncomms2332 4

[13] J. E. Sonier, J. H. Brewer, and R. F. Kiefl, "μsr studies of the vortex state in type-ii superconductors," *Rev. Mod. Phys.*, vol. 72, pp. 769–811, Jul 2000. [Online]. Available: https://link.aps.org/doi/10.1103/RevModPhys.72.769 4

[14] S. Forstner, E. Sheridan, J. Knittel, C. L. Humphreys, G. A. Brawley, H. Rubinsztein-Dunlop, and W. P. Bowen, "Ultrasensitive optomechanical magnetometry," *Advanced Materials*, vol. 26, no. 36, pp. 6348–6353, 2014. [Online]. Available: https://onlinelibrary.wiley.com/doi/abs/10.1002/adma.201401144 4

[15] M. A. Nielsen and I. L. Chuang, *Quantum computation and quantum information*. Cambridge; New York: Cambridge University Press, 2000. [Online]. Available: https://books.google.com/books?id=65FqEKQOfP8C 4, 47, 53

[16] R. Schirhagl, K. Chang, M. Loretz, and C. L. Degen, "Nitrogen-vacancy centers in diamond: Nanoscale sensors for physics and biology," *Annual Review of Physical Chemistry*, vol. 65, no. 1, pp. 83–105, 2014, pMID: 24274702. [Online]. Available: https://doi.org/10.1146/annurev-physchem-040513-103659 5

[17] L. Rondin, J.-P. Tetienne, T. Hingant, J.-F. Roch, P. Maletinsky, and V. Jacques, "Magnetometry with nitrogen-vacancy defects in diamond,"

Reports on Progress in Physics, vol. 77, no. 5, p. 056503, 2014. [Online]. Available: http://stacks.iop.org/0034-4885/77/i=5/a=056503 5

[18] M. V. G. Dutt, L. Childress, L. Jiang, E. Togan, J. Maze, F. Jelezko, A. S. Zibrov, P. R. Hemmer, and M. D. Lukin, "Quantum register based on individual electronic and nuclear spin qubits in diamond," *Science*, vol. 316, pp. 1312–1316, 2007. [Online]. Available: http://dx.doi.org/10.1126/science.1139831 5

[19] M. Hirose and P. Cappellaro, "Coherent feedback control of a single qubit in diamond," *Nature*, vol. 532, no. 7597, pp. 77–80, Apr. 2016. [Online]. Available: http://dx.doi.org/10.1038/nature17404 5, 28, 32, 91

[20] P. Neumann, N. Mizuochi, F. Rempp, P. Hemmer, H. Watanabe, S. Yamasaki, V. Jacques, T. Gaebel, F. Jelezko, and J. Wrachtrup, "Multipartite entanglement among single spins in diamond," *Science*, vol. 320, no. 5881, pp. 1326–1329, 2008. [Online]. Available: http://dx.doi.org/10.1126/science.1157233 5

[21] H. Bernien, B. Hensen, W. Pfaff, G. Koolstra, M. S. Blok, L. Robledo, T. H. Taminiau, M. Markham, D. J. Twitchen, L. Childress, and R. Hanson, "Heralded entanglement between solid-state qubits separated by three metres," *Nature*, vol. 497, pp. 86 EP –, Apr 2013. [Online]. Available: http://dx.doi.org/10.1038/nature12016 5

[22] J. M. Taylor, P. Cappellaro, L. Childress, L. Jiang, D. Budker, P. R. Hemmer, A. Yacoby, R. Walsworth, and M. D. Lukin, "High-sensitivity diamond magnetometer with nanoscale resolution," *Nat. Phys.*, vol. 4, no. 10, pp. 810–816, 2008. [Online]. Available: http://dx.doi.org/10.1038/nphys1075 5, 58

[23] J. R. Maze, P. L. Stanwix, J. S. Hodges, S. Hong, J. M. Taylor, P. Cappellaro, L. Jiang, A. Zibrov, A. Yacoby, R. Walsworth, and M. D. Lukin, "Nanoscale magnetic sensing with an individual electronic spin qubit in diamond," *Nature*, vol. 455, pp. 644–647, 2008. [Online]. Available: http://dx.doi.org/10.1038/nature07279 5

[24] C. L. Degen, "Scanning magnetic field microscope with a diamond single-spin sensor," *App. Phys. Lett*, vol. 92, no. 24, p. 243111, 2008. [Online]. Available: http://dx.doi.org/10.1063/1.2943282 5, 91

[25] T. Staudacher, F. Shi, S. Pezzagna, J. Meijer, J. Du, C. A. Meriles, F. Reinhard, and J. Wrachtrup, "Nuclear magnetic

resonance spectroscopy on a (5-Nanometer)^3 sample volume," *Science*, vol. 339, no. 6119, pp. 561–563, 2013. [Online]. Available: http://www.sciencemag.org/content/339/6119/561.abstract 5, 91

[26] L. T. Hall, G. C. G. Beart, E. A. Thomas, D. A. Simpson, L. P. McGuinness, J. H. Cole, J. H. Manton, R. E. Scholten, F. Jelezko, J. Wrachtrup, S. Petrou, and L. C. L. Hollenberg, "High spatial and temporal resolution wide-field imaging of neuron activity using quantum nv-diamond," *Sci. Rep.*, vol. 2, p. 401, May 2012. [Online]. Available: http://dx.doi.org/10.1038/srep00401 5, 91

[27] J. F. Barry, M. J. Turner, J. M. Schloss, D. R. Glenn, Y. Song, M. D. Lukin, H. Park, and R. L. Walsworth, "Optical magnetic detection of single-neuron action potentials using quantum defects in diamond," *Proc. Nat Acad. Sc.*, vol. 113, no. 49, pp. 14 133–14 138, 2016. [Online]. Available: http://www.pnas.org/content/113/49/14133.abstract 5, 48, 67, 69, 72, 91

[28] F. Jelezko and J. Wrachtrup, "Single defect centres in diamond: A review," *Physica Status Solidi (A)*, vol. 203, no. 13, pp. 3207–3225, 2006. [Online]. Available: http://dx.doi.org/10.1002/pssa.200671403 7

[29] G. Balasubramanian, P. Neumann, D. Twitchen, M. Markham, R. Kolesov, N. Mizuochi, J. Isoya, J. Achard, J. Beck, J. Tissler, V. Jacques, P. R. Hemmer, F. Jelezko, and J. Wrachtrup, "Ultralong spin coherence time in isotopically engineered diamond," *Nat. Mater.*, vol. 8, no. 5, pp. 383–387, 2009. [Online]. Available: http://dx.doi.org/10.1038/nmat2420 7

[30] A. Zaitsev, *Optical Properties of Diamond: A Data Handbook*. Springer Berlin Heidelberg, 2013. [Online]. Available: https://books.google.it/books?id=WsvuCAAAQBAJ 8

[31] C. Schreyvogel, V. Polyakov, R. Wunderlich, J. Meijer, and C. E. Nebel, "Active charge state control of single nv centres in diamond by in-plane Al-Schottky junctions," *Scientific Reports*, vol. 5, pp. 12 160 EP –, Jul 2015, article. [Online]. Available: http://dx.doi.org/10.1038/srep12160 8

[32] Y. Mita, "Change of absorption spectra in type-Ib diamond with heavy neutron irradiation," *Phys. Rev. B*, vol. 53, no. 17, pp. 11 360–11 364, 1996. [Online]. Available: http://dx.doi.org/10.1103/PhysRevB.53.11360 8, 9

[33] L. Du Preez, "Electron paramagnetic resonance and optical investigations of defect centres in diamond," Ph.D. dissertation, University of Witwatersrand, Johannesburg, 1965. 8

[34] A. Gruber, A. Drabenstedt, C. Tietz, L. Fleury, J. Wrachtrup, and C. v. Borczyskowski, "Scanning confocal optical microscopy and magnetic resonance on single defect centers," *Science*, vol. 276, no. 5321, pp. 2012–2014, 1997. [Online]. Available: http://dx.doi.org/10.1126/science.276.5321.2012 8

[35] M. Pfender, N. Aslam, P. Simon, D. Antonov, G. Thiering, S. Burk, F. Fávaro de Oliveira, A. Denisenko, H. Fedder, J. Meijer, J. A. Garrido, A. Gali, T. Teraji, J. Isoya, M. W. Doherty, A. Alkauskas, A. Gallo, A. Grüneis, P. Neumann, and J. Wrachtrup, "Protecting a diamond quantum memory by charge state control," *Nano Letters*, vol. 17, no. 10, pp. 5931–5937, 2017, pMID: 28872881. [Online]. Available: https://doi.org/10.1021/acs.nanolett.7b01796 8

[36] A. Gali, "Identification of individual ^{13}C isotopes of nitrogen-vacancy center in diamond by combining the polarization studies of nuclear spins and first-principles calculations," *Phys. Rev. B*, vol. 80, p. 241204, Dec 2009. [Online]. Available: http://link.aps.org/doi/10.1103/PhysRevB.80.241204 8, 28, 43, 44

[37] L. M. Pham, "Magnetic field sensing with nitrogen-vacancy color centers in diamond," Ph.D. dissertation, Harvard University, 2013. [Online]. Available: http://nrs.harvard.edu/urn-3:HUL.InstRepos:11051173 8

[38] M. Werner and R. Locher, "Growth and application of undoped and doped diamond films," *Reports on Progress in Physics*, vol. 61, no. 12, p. 1665, 1998. [Online]. Available: http://stacks.iop.org/0034-4885/61/i=12/a=002 8

[39] A. M. Edmonds, U. F. S. D'Haenens-Johansson, R. J. Cruddace, M. E. Newton, K.-M. C. Fu, C. Santori, R. G. Beausoleil, D. J. Twitchen, and M. L. Markham, "Production of oriented nitrogen-vacancy color centers in synthetic diamond," *Phys. Rev. B*, vol. 86, p. 035201, Jul 2012. [Online]. Available: http://link.aps.org/doi/10.1103/PhysRevB.86.035201 8

[40] J. J. Harris, "Delta-doping of semiconductors," *Journal of Materials Science: Materials in Electronics*, vol. 4, no. 2, pp. 93–105, Jun 1993. [Online]. Available: https://doi.org/10.1007/BF00180462 9

[41] K. Ohno, F. Joseph Heremans, L. C. Bassett, B. A. Myers, D. M. Toyli, A. C. Bleszynski Jayich, C. J. Palmstrom, and D. D. Awschalom, "Engineering shallow spins in diamond with nitrogen delta-doping," *App. Phys. Lett*, vol. 101, no. 8, p. 082413, Aug. 2012. [Online]. Available: http://link.aip.org/link/?APPLAB/101/082413/1 9

[42] J. Meijer, B. Burchard, M. Domhan, C. Wittmann, T. Gaebel, I. Popa, F. Jelezko, and J. Wrachtrup, "Generation of single color centers by focused nitrogen implantation," *App. Phys. Lett*, vol. 87, no. 26, p. 261909, 2005. 9

[43] S. Pezzagna, D. Rogalla, H.-W. Becker, I. Jakobi, F. Dolde, B. Naydenov, J. Wrachtrup, F. Jelezko, C. Trautmann, and J. Meijer, "Creation of colour centres in diamond by collimated ion-implantation through nano-channels in mica," *physica status solidi (a)*, vol. 208, no. 9, pp. 2017–2022, 2011. [Online]. Available: http://dx.doi.org/10.1002/pssa.201100455 9

[44] M. Loretz, S. Pezzagna, J. Meijer, and C. L. Degen, "Nanoscale nuclear magnetic resonance with a 1.9nm-deep nitrogen-vacancy sensor," *Appl. Phys. Lett.*, vol. 104, no. 3, p. 033102, jan 2014. [Online]. Available: http://dx.doi.org/10.1063/1.4862749 9, 65, 91

[45] J. O. Orwa, C. Santori, K. M. C. Fu, B. Gibson, D. Simpson, I. Aharonovich, A. Stacey, A. Cimmino, P. Balog, M. Markham, D. Twitchen, A. D. Greentree, R. G. Beausoleil, and S. Prawer, "Engineering of nitrogen-vacancy color centers in high purity diamond by ion implantation and annealing," *Journal of Applied Physics*, vol. 109, no. 8, p. 083530, 2011. [Online]. Available: https://doi.org/10.1063/1.3573768 9

[46] J. R. Maze, A. Gali, E. Togan, Y. Chu, A. Trifonov, E. Kaxiras, and M. D. Lukin, "Properties of nitrogen-vacancy centers in diamond: the group theoretic approach," *New J. Phys.*, vol. 13, no. 2, p. 025025, 2011. [Online]. Available: http://stacks.iop.org/1367-2630/13/i=2/a=025025 9, 10

[47] A. Gali, M. Fyta, and E. Kaxiras, "Ab initio supercell calculations on nitrogen-vacancy center in diamond: Electronic structure and hyperfine tensors," *Phys. Rev. B*, vol. 77, no. 15, p. 155206, 2008. [Online]. Available: http://dx.doi.org/10.1103/PhysRevB.77.155206 9

[48] P. Kok and B. W. Lovett, "Qubits in the pink," *Nature*, vol. 444, pp. 49 EP –, Nov 2006. [Online]. Available: http://dx.doi.org/10.1038/444049a 9

[49] M. W. Doherty, N. B. Manson, P. Delaney, F. Jelezko, J. Wrachtrup, and L. C. Hollenberg, "The nitrogen-vacancy colour centre in diamond," *Physics Reports*, vol. 528, no. 1, pp. 1 – 45, 2013, the nitrogen-vacancy colour centre in diamond. [Online]. Available: http://www.sciencedirect.com/science/article/pii/S0370157313000562 10, 44

[50] L. J. Rogers, S. Armstrong, M. J. Sellars, and N. B. Manson, "Infrared emission of the nv centre in diamond: Zeeman and uniaxial stress studies," *New J. Phys.*, vol. 10, no. 10, p. 103024, 2008. [Online]. Available: http://dx.doi.org/10.1088/1367-2630/10/10/103024 10

[51] N. B. Manson, J. P. Harrison, and M. J. Sellars, "Nitrogen-vacancy center in diamond: Model of the electronic structure and associated dynamics," *Phys. Rev. B*, vol. 74, no. 10, p. 104303, 2006. [Online]. Available: http://dx.doi.org/10.1103/PhysRevB.74.104303 10, 11, 39

[52] L. Robledo, H. Bernien, T. van der Sar, and R. Hanson, "Spin dynamics in the optical cycle of single nitrogen-vacancy centres in diamond," *New J. Phys.*, vol. 13, no. 2, p. 025013, 2011. [Online]. Available: http://stacks.iop.org/1367-2630/13/i=2/a=025013 10, 11, 39

[53] J.-P. Tetienne, L. Rondin, P. Spinicelli, M. Chipaux, T. Debuisschert, J.-F. Roch, and V. Jacques, "Magnetic-field-dependent photodynamics of single nv defects in diamond: An application to qualitative all-optical magnetic imaging," *New J. Phys.*, vol. 14, no. 10, p. 103033, 2012. [Online]. Available: http://stacks.iop.org/1367-2630/14/i=10/a=103033 11, 39, 92

[54] J. Wolters, M. Strauß, R. S. Schoenfeld, and O. Benson, "Quantum Zeno phenomenon on a single solid-state spin," *Phys. Rev. A*, vol. 88, p. 020101, Aug 2013. [Online]. Available: https://link.aps.org/doi/10.1103/PhysRevA.88.020101 11

[55] L. J. Rogers, R. L. McMurtrie, M. J. Sellars, and N. B. Manson, "Time-averaging within the excited state of the nitrogen-vacancy centre in diamond," *New J. Phys.*, vol. 11, p. 063007, 2009. [Online].

Available: http://iopscience.iop.org/article/10.1088/1367-2630/11/6/063007/meta 13

[56] A. Batalov, V. Jacques, F. Kaiser, P. Siyushev, P. Neumann, L. J. Rogers, R. L. McMurtrie, N. B. Manson, F. Jelezko, and J. Wrachtrup, "Low temperature studies of the excited-state structure of negatively charged nitrogen-vacancy color centers in diamond," *Phys. Rev. Lett.*, vol. 102, no. 19, p. 195506, 2009. [Online]. Available: http://link.aps.org/abstract/PRL/v102/e195506 13

[57] G. D. Fuchs, V. V. Dobrovitski, R. Hanson, A. Batra, C. D. Weis, T. Schenkel, and D. D. Awschalom, "Excited-state spectroscopy using single spin manipulation in diamond," *Phys. Rev. Lett.*, vol. 101, no. 11, p. 117601, 2008. [Online]. Available: http://link.aps.org/abstract/PRL/v101/e117601 14, 28, 44

[58] B. Smeltzer, J. McIntyre, and L. Childress, "Robust control of individual nuclear spins in diamond," *Phys. Rev. A*, vol. 80, p. 050302, Nov 2009. [Online]. Available: http://link.aps.org/doi/10.1103/PhysRevA.80.050302 14, 28, 44

[59] M. Chen, M. Hirose, and P. Cappellaro, "Measurement of transverse hyperfine interaction by forbidden transitions," *Phys. Rev. B*, vol. 92, p. 020101, Jul 2015. [Online]. Available: http://link.aps.org/doi/10.1103/PhysRevB.92.020101 14

[60] M. Steiner, P. Neumann, J. Beck, F. Jelezko, and J. Wrachtrup, "Universal enhancement of the optical readout fidelity of single electron spins at nitrogen-vacancy centers in diamond," *Phys. Rev. B*, vol. 81, no. 3, p. 035205, 2010. [Online]. Available: http://dx.doi.org/10.1103/PhysRevB.81.035205 14, 44

[61] C. J. Foot, *Atomic physics*, ser. Oxford master series in atomic, optical and laser physics. Oxford: Oxford University Press, 2004. [Online]. Available: https://cds.cern.ch/record/1080846 17, 19

[62] S. Blundell, *Magnetism in Condensed Matter*, ser. Oxford Master Series in Condensed Matter Physics. OUP Oxford, 2001. [Online]. Available: https://books.google.it/books?id=OGhGmgEACAAJ 19

[63] E. L. Hahn, "Spin echoes," *Phys. Rev.*, vol. 80, no. 4, pp. 580–594, 1950. [Online]. Available: http://dx.doi.org/10.1103/PhysRev.80.580 22, 24

[64] M. J. Biercuk, A. C. Doherty, and H. Uys, "Dynamical decoupling sequence construction as a filter-design problem," *J. of Phys. B*, vol. 44, no. 15, p. 154002, 2011. [Online]. Available: http://stacks.iop.org/0953-4075/44/i=15/a=154002 23, 51, 73, 75

[65] P. L. Stanwix, L. M. Pham, J. R. Maze, D. Le Sage, T. K. Yeung, P. Cappellaro, P. R. Hemmer, A. Yacoby, M. D. Lukin, and R. L. Walsworth, "Coherence of nitrogen-vacancy electronic spin ensembles in diamond," *Phys. Rev. B*, vol. 82, p. 201201, 2010. [Online]. Available: http://link.aps.org/doi/10.1103/PhysRevB.82.201201 25

[66] L. Viola and S. Lloyd, "Dynamical suppression of decoherence in two-state quantum systems," *Phys. Rev. A*, vol. 58, p. 2733, 1998. [Online]. Available: http://dx.doi.org/10.1103/PhysRevA.58.2733 26, 58, 74

[67] H. Y. Carr and E. M. Purcell, "Effects of diffusion on free precession in nuclear magnetic resonance experiments," *Phys. Rev.*, vol. 94, no. 3, pp. 630–638, 1954. [Online]. Available: http://dx.doi.org/10.1103/PhysRev.94.630 26, 75

[68] S. Meiboom and D. Gill, "Modified spin-echo method for measuring nuclear relaxation times," *Rev. Sc. Instr.*, vol. 29, no. 8, pp. 688–691, 1958. [Online]. Available: http://dx.doi.org/10.1063/1.1716296 26

[69] K. Khodjasteh and D. A. Lidar, "Fault-tolerant quantum dynamical decoupling," *Phys. Rev. Lett.*, vol. 95, no. 18, p. 180501, 2005. [Online]. Available: http://dx.doi.org/10.1103/PhysRevLett.95.180501 26

[70] T. Gullion, D. B. Baker, and M. S. Conradi, "New, compensated Carr-Purcell sequences," *J. Mag. Res.*, vol. 89, no. 3, pp. 479 – 484, 1990. [Online]. Available: http://www.sciencedirect.com/science/article/pii/0022236490903313 26, 76

[71] G. de Lange, Z. H. Wang, D. Riste, V. V. Dobrovitski, and R. Hanson, "Universal dynamical decoupling of a single solid-state spin from a spin bath." *Science*, vol. 330, no. 6000, pp. 60–3, Oct. 2010. [Online]. Available: http://www.sciencemag.org/content/330/6000/60.abstract 26

[72] G. S. Uhrig, "Keeping a quantum bit alive by optimized π-pulse sequences," *Phys. Rev. Lett.*, vol. 98, no. 10, p. 100504, 2007. [Online]. Available: http://dx.doi.org/10.1103/PhysRevLett.98.100504 26, 51, 73, 86

[73] J. Casanova, Z.-Y. Wang, J. F. Haase, and M. B. Plenio, "Robust dynamical decoupling sequences for individual-nuclear-spin addressing," *Phys. Rev. A*, vol. 92, p. 042304, Oct 2015. [Online]. Available: https://link.aps.org/doi/10.1103/PhysRevA.92.042304 27, 62, 86

[74] N. Zhao, J. Wrachtrup, and R.-B. Liu, "Dynamical decoupling design for identifying weakly coupled nuclear spins in a bath," *Phys. Rev. A*, vol. 90, p. 032319, Sep 2014. [Online]. Available: https://link.aps.org/doi/10.1103/PhysRevA.90.032319 27, 62, 86

[75] I. Lovchinsky, A. O. Sushkov, E. Urbach, N. P. de Leon, S. Choi, K. De Greve, R. Evans, R. Gertner, E. Bersin, C. Müller, L. McGuinness, F. Jelezko, R. L. Walsworth, H. Park, and M. D. Lukin, "Nuclear magnetic resonance detection and spectroscopy of single proteins using quantum logic," *Science*, vol. 351, no. 6275, pp. 836–841, 2016. [Online]. Available: http://science.sciencemag.org/content/351/6275/836 28, 65, 91

[76] P. Neumann, J. Beck, M. Steiner, F. Rempp, H. Fedder, P. R. Hemmer, J. Wrachtrup, and F. Jelezko, "Single-shot readout of a single nuclear spin," *Science*, vol. 5991, pp. 542–544, 2010. [Online]. Available: http://www.sciencemag.org/cgi/content/abstract/science.1189075v1 28

[77] P. C. Maurer, G. Kucsko, C. Latta, L. Jiang, N. Y. Yao, S. D. Bennett, F. Pastawski, D. Hunger, N. Chisholm, M. Markham, D. J. Twitchen, J. I. Cirac, and M. D. Lukin, "Room-temperature quantum bit memory exceeding one second," *Science*, vol. 336, no. 6086, pp. 1283–1286, 2012. [Online]. Available: http://www.sciencemag.org/content/336/6086/1283.abstract 28, 32

[78] G. Waldherr, Y. Wang, S. Zaiser, M. Jamali, T. Schulte-Herbruggen, H. Abe, T. Ohshima, J. Isoya, J. F. Du, P. Neumann, and J. Wrachtrup, "Quantum error correction in a solid-state hybrid spin register," *Nature*, vol. 506, no. 7487, pp. 204–207, Feb. 2014. [Online]. Available: http://dx.doi.org/10.1038/nature12919 28, 47

[79] J. Cramer, N. Kalb, M. A. Rol, B. Hensen, M. S. Blok, M. Markham, D. J. Twitchen, R. Hanson, and T. H. Taminiau, "Repeated quantum error correction on a continuously encoded qubit by real-time feedback," *Nature Communications*, vol. 7, p. 11526, may 2016. [Online]. Available: http://dx.doi.org/10.1038/ncomms11526 28

[80] X.-F. He, N. B. Manson, and P. T. H. Fisk, "Paramagnetic resonance of photoexcited N-V defects in diamond. I. Level anticrossing in the ^{3}A ground state," *Phys. Rev. B*, vol. 47, no. 14, pp. 8809–8815, 1993. [Online]. Available: http://dx.doi.org/10.1103/PhysRevB.47.8809 28, 44

[81] V. Jacques, P. Neumann, J. Beck, M. Markham, D. Twitchen, J. Meijer, F. Kaiser, G. Balasubramanian, F. Jelezko, and J. Wrachtrup, "Dynamic polarization of single nuclear spins by optical pumping of nitrogen-vacancy color centers in diamond at room temperature," *Phys. Rev. Lett.*, vol. 102, no. 5, p. 057403, 2009. [Online]. Available: http://link.aps.org/abstract/PRL/v102/e057403 28, 34

[82] Y. Hovav, B. Naydenov, F. Jelezko, and N. Bar-Gill, "Low-field nuclear polarization using nitrogen vacancy centers in diamonds," *Phys. Rev. Lett.*, vol. 120, p. 060405, Feb 2018. [Online]. Available: https://link.aps.org/doi/10.1103/PhysRevLett.120.060405 28

[83] F. Poggiali, P. Cappellaro, and N. Fabbri, "Measurement of the excited-state transverse hyperfine coupling in nv centers via dynamic nuclear polarization," *Phys. Rev. B*, vol. 95, p. 195308, May 2017. [Online]. Available: https://link.aps.org/doi/10.1103/PhysRevB.95.195308 28, 46, 90

[84] G. Lindblad, "On the generators of quantum dynamical semigroups," *Communications in Mathematical Physics*, vol. 48, no. 2, pp. 119–130, 1976. [Online]. Available: http://dx.doi.org/10.1007/BF01608499 29, 39

[85] M. Hirose, "Quantum control of spin systems in diamond," Ph.D. dissertation, Massachusetts Institute of Technology, 2015. [Online]. Available: https://dspace.mit.edu/handle/1721.1/103731 33

[86] R. Fischer, A. Jarmola, P. Kehayias, and D. Budker, "Optical polarization of nuclear ensembles in diamond," *Phys. Rev. B*, vol. 87, p. 125207, Mar 2013. [Online]. Available: http://link.aps.org/doi/10.1103/PhysRevB.87.125207 38

[87] F. Ticozzi and L. Viola, "Analysis and synthesis of attractive quantum Markovian dynamics," *Automatica*, vol. 45, no. 9, pp. 2002–2009, 2009. [Online]. Available: http://www.sciencedirect.com/science/article/pii/S0005109809002507 38

[88] B. Grotz, M. V. Hauf, M. Dankerl, B. Naydenov, S. Pezzagna, J. Meijer, F. Jelezko, J. Wrachtrup, M. Stutzmann, F. Reinhard, and J. A. Garrido, "Charge state manipulation of qubits in diamond," *Nature Communications*, vol. 3, pp. 729 EP –, Mar 2012, article. [Online]. Available: http://dx.doi.org/10.1038/ncomms1729 40

[89] B. J. Shields, Q. P. Unterreithmeier, N. P. de Leon, H. Park, and M. D. Lukin, "Efficient readout of a single spin state in diamond via spin-to-charge conversion," *Phys. Rev. Lett.*, vol. 114, p. 136402, Mar 2015. [Online]. Available: http://link.aps.org/doi/10.1103/PhysRevLett.114.136402 40

[90] D. A. Hopper, R. R. Grote, A. L. Exarhos, and L. C. Bassett, "Near-infrared-assisted charge control and spin readout of the nitrogen-vacancy center in diamond," *Phys. Rev. B*, vol. 94, p. 241201, Dec 2016. [Online]. Available: https://link.aps.org/doi/10.1103/PhysRevB.94.241201 40

[91] N. Aslam, G. Waldherr, P. Neumann, F. Jelezko, and J. Wrachtrup, "Photo-induced ionization dynamics of the nitrogen vacancy defect in diamond investigated by single-shot charge state detection," *New J. Phys.*, vol. 15, no. 1, p. 013064, 2013. [Online]. Available: http://stacks.iop.org/1367-2630/15/i=1/a=013064 40

[92] X.-D. Chen, C.-L. Zou, F.-W. Sun, and G.-C. Guo, "Optical manipulation of the charge state of nitrogen-vacancy center in diamond," *Applied Physics Letters*, vol. 103, no. 1, p. 013112, 2013. [Online]. Available: https://doi.org/10.1063/1.4813120 40

[93] X. Chen, C. Zou, Z. Gong, C. Dong, G. Guo, and F. Sun, "Subdiffraction optical manipulation of the charge state of nitrogen vacancy center in diamond," *Light: Science &Amp; Applications*, vol. 4, pp. e230 EP –, Jan 2015, original Article. [Online]. Available: http://dx.doi.org/10.1038/lsa.2015.3 40

[94] S. Dhomkar, J. Henshaw, H. Jayakumar, and C. A. Meriles, "Long-term data storage in diamond," *Science Advances*, vol. 2, no. 10, 2016. [Online]. Available: http://advances.sciencemag.org/content/2/10/e1600911 40

[95] J. R. Rabeau, A. Stacey, A. Rabeau, S. Prawer, F. Jelezko, I. Mirza, and J. Wrachtrup, "Single nitrogen vacancy centers in chemical vapor deposited diamond nanocrystals," *Nano Letters*,

vol. 7, no. 11, pp. 3433–3437, 2007. [Online]. Available: http://dx.doi.org/10.1021/nl0719271 44

[96] S. Felton, A. M. Edmonds, M. E. Newton, P. M. Martineau, D. Fisher, and D. J. Twitchen, "Electron paramagnetic resonance studies of the neutral nitrogen vacancy in diamond," *Phys. Rev. B*, vol. 77, p. 081201, Feb 2008. [Online]. Available: http://link.aps.org/doi/10.1103/PhysRevB.77.081201 44

[97] P. Neumann, R. Kolesov, V. Jacques, J. Beck, J. Tisler, A. Batalov, L. Rogers, N. B. Manson, G. Balasubramanian, F. Jelezko, and J. Wrachtrup, "Excited-state spectroscopy of single nv defects in diamond using optically detected magnetic resonance," *New J. Phys.*, vol. 11, no. 1, p. 013017, 2009. [Online]. Available: http://stacks.iop.org/1367-2630/11/013017 44

[98] H.-J. Wang, C. S. Shin, C. E. Avalos, S. J. Seltzer, D. Budker, A. Pines, and V. S. Bajaj, "Sensitive magnetic control of ensemble nuclear spin hyperpolarization in diamond," *Nat. Commun.*, vol. 4, pp. –, Jun. 2013. [Online]. Available: http://dx.doi.org/10.1038/ncomms2930 44

[99] N. Timoney, V. Elman, S. Glaser, C. Weiss, M. Johanning, W. Neuhauser, and C. Wunderlich, "Error-resistant single-qubit gates with trapped ions," *Phys. Rev. A*, vol. 77, no. 5, p. 052334, 2008. [Online]. Available: http://dx.doi.org/10.1103/PhysRevA.77.052334 47

[100] S. Rosi, A. Bernard, N. Fabbri, L. Fallani, C. Fort, M. Inguscio, T. Calarco, and S. Montangero, "Fast closed-loop optimal control of ultracold atoms in an optical lattice," *Phys. Rev. A*, vol. 88, no. 2, p. 021601, Aug. 2013. [Online]. Available: https://doi.org/10.1103/PhysRevA.88.021601 47

[101] M. D. Reed, L. DiCarlo, S. E. Nigg, L. Sun, L. Frunzio, S. M. Girvin, and R. J. Schoelkopf, "Realization of three-qubit quantum error correction with superconducting circuits," *Nature*, vol. 482, pp. 382–, Feb. 2012. [Online]. Available: http://dx.doi.org/10.1038/nature10786 47

[102] A. Spörl, T. Schulte-Herbrüggen, S. J. Glaser, V. Bergholm, M. J. Storcz, J. Ferber, and F. K. Wilhelm, "Optimal control of coupled Josephson qubits," *Phys. Rev. A*, vol. 75, no. 1, p. 012302, 2007.

[Online]. Available: http://dx.doi.org/10.1103/PhysRevA.75.012302 47

[103] D. Cory, R. Laflamme, E. Knill, L. Viola, T. Havel, N. Boulant, G. Boutis, E. Fortunato, S. Lloyd, R. Martinez, C. Negrevergne, M. Pravia, Y. Sharf, G. Teklemariam, Y. Weinstein, and W. Zurek, "NMR based quantum information processing: Achievements and prospects," *Fort. der Phys.*, vol. 48, no. 9-11, pp. 875–907, 2000. 47

[104] J. Zhang, D. Gangloff, O. Moussa, and R. Laflamme, "Experimental quantum error correction with high fidelity," *Phys. Rev. A*, vol. 84, no. 3, p. 034303, Sep. 2011. 47

[105] J. Wrachtrup and F. Jelezko, "Processing quantum information in diamond," *J. Phys.: Condens. Matter*, vol. 18, no. 21, pp. S807–S824, 2006. [Online]. Available: http://dx.doi.org/10.1088/0953-8984/18/21/S08 47

[106] D. D'Alessandro, *Introduction to Quantum Control and Dynamics*. Taylor & Francis Ltd, 2007. [Online]. Available: http://www.ebook.de/de/product/5971555/domenico_iowa_state_university_ames_usa_d_alessandro_introduction_to_quantum_control_and_dynamics.html 47

[107] S. J. Glaser, U. Boscain, T. Calarco, C. P. Koch, W. Koeckenberger, R. Kosloff, I. Kuprov, B. Luy, S. Schirmer, T. Schulte-Herbrueggen, D. Sugny, and F. K. Wilhelm, "Training Schrödinger's cat: quantum optimal control," *The European Physical Journal D*, vol. 69, no. 12, p. 279, 2015. [Online]. Available: https://doi.org/10.1140/epjd/e2015-60464-1 47, 91

[108] E. M. Fortunato, M. A. Pravia, N. Boulant, G. Teklemariam, T. F. Havel, and D. G. Cory, "Design of strongly modulating pulses to implement precise effective Hamiltonians for quantum information processing," *J. Chem. Phys.*, vol. 116, p. 7599, 2002. [Online]. Available: http://dx.doi.org/10.1063/1.1465412 47

[109] N. Khaneja, T. Reiss, C. Kehlet, T. Schulte-Herbuggen, and S. Glaser, "Optimal control of coupled spin dynamics: design of NMR pulse sequences by gradient ascent algorithms," *J. Mag. Res.*, vol. 172, pp. 296–305, 2005. [Online]. Available: http://dx.doi.org/10.1016/j.jmr.2004.11.004 47

[110] T. Caneva, T. Calarco, and S. Montangero, "Chopped random-basis quantum optimization," *Phys. Rev. A*, vol. 84, p. 022326, Aug 2011. [Online]. Available: http://link.aps.org/doi/10.1103/PhysRevA.84.022326 47

[111] S. Machnes, U. Sander, S. J. Glaser, P. de Fouquières, A. Gruslys, S. Schirmer, and T. Schulte-Herbrüggen, "Comparing, optimizing, and benchmarking quantum-control algorithms in a unifying programming framework," *Phys. Rev. A*, vol. 84, p. 022305, Aug 2011. [Online]. Available: http://link.aps.org/doi/10.1103/PhysRevA.84.022305 47

[112] G. Ciaramella, A. Borzì, G. Dirr, and D. Wachsmuth, "Newton methods for the optimal control of closed quantum spin systems," *SIAM Journal on Scientific Computing*, vol. 37, no. 1, pp. A319–A346, 2015. [Online]. Available: https://doi.org/10.1137/140966988 47

[113] C. A. Ryan, J. S. Hodges, and D. G. Cory, "Robust decoupling techniques to extend quantum coherence in diamond," *Phys. Rev. Lett.*, vol. 105, no. 20, p. 200402, 2010. [Online]. Available: http://dx.doi.org/10.1103/PhysRevLett.105.200402 47

[114] D. J. Tannor and S. A. Rice, "Control of selectivity of chemical reaction via control of wave packet evolution," *J. Chem. Phys.*, vol. 83, pp. 5013–5018, Nov. 1985. 47

[115] P. Brumer and M. Shapiro, "Laser control of molecular processes," *Annual Review of Physical Chemistry*, vol. 43, pp. 257–282, Oct. 1992. 47

[116] T. C. Weinacht, J. Ahn, and P. H. Bucksbaum, "Controlling the shape of a quantum wavefunction," *Nature*, vol. 397, pp. 233–, Jan. 1999. [Online]. Available: http://dx.doi.org/10.1038/16654 47

[117] S. Machnes, M. B. Plenio, B. Reznik, A. M. Steane, and A. Retzker, "Superfast laser cooling," *Phys. Rev. Lett.*, vol. 104, no. 18, p. 183001, May 2010. 47

[118] A. Rahmani, T. Kitagawa, E. Demler, and C. Chamon, "Cooling through optimal control of quantum evolution," *pra*, vol. 87, no. 4, p. 043607, Apr. 2013. 47

[119] Z. Tošner, T. Vosegaard, C. Kehlet, N. Khaneja, S. J. Glaser, and N. C. Nielsen, "Optimal control in NMR spectroscopy: Numerical implementation in simpson," *J. Mag. Res.*, vol. 197, pp. 120–134, Apr. 2009. 47

[120] P. Doria, T. Calarco, and S. Montangero, "Optimal control technique for many-body quantum dynamics," *Phys. Rev. Lett.*, vol. 106, p. 190501, May 2011. [Online]. Available: http://link.aps.org/doi/10.1103/PhysRevLett.106.190501 47

[121] S. van Frank, M. Bonneau, J. Schmiedmayer, S. Hild, C. Gross, M. Cheneau, I. Bloch, T. Pichler, A. Negretti, T. Calarco, and S. Montangero, "Optimal control of complex atomic quantum systems," *Scientific Reports*, vol. 6, p. 34187, Oct. 2016. 47

[122] F. Poggiali, P. Cappellaro, and N. Fabbri, "Optimal control for one-qubit quantum sensing," *Phys. Rev. X*, vol. 8, p. 021059, Jun 2018. [Online]. Available: https://link.aps.org/doi/10.1103/PhysRevX.8.021059 48, 90

[123] T. Häberle, D. Schmid-Lorch, K. Karrai, F. Reinhard, and J. Wrachtrup, "High-dynamic-range imaging of nanoscale magnetic fields using optimal control of a single qubit," *Phys. Rev. Lett.*, vol. 111, no. 17, p. 170801, Oct. 2013. 48

[124] T. Nöbauer, A. Angerer, B. Bartels, M. Trupke, S. Rotter, J. Schmiedmayer, F. Mintert, and J. Majer, "Smooth optimal quantum control for robust solid-state spin magnetometry," *Physical Review Letters*, vol. 115, no. 19, p. 190801, Nov. 2015. 48

[125] S. Pang and A. N. Jordan, "Optimal adaptive control for quantum metrology with time-dependent hamiltonians," *Nat. Commun.*, vol. 8, p. 14695, mar 2017. [Online]. Available: https://doi.org/10.1038/ncomms14695 48

[126] J. Wikswo, J. Barach, and J. Freeman, "Magnetic field of a nerve impulse: First measurements," *Science*, vol. 208, no. 4439, pp. 53–55, Apr. 1980. [Online]. Available: http://www.sciencemag.org/content/208/4439/53.abstract 48, 67

[127] G. Bison, N. Castagna, A. Hofer, P. Knowles, J.-L. Schenker, M. Kasprzak, H. Saudan, and A. Weis, "A room temperature 19-channel magnetic field mapping device for cardiac signals," *App. Phys. Lett*, vol. 95, no. 17, p. 173701, Oct. 2009. 48, 67

[128] K. Jensen, R. Budvytyte, R. A. Thomas, T. Wang, A. M. Fuchs, M. V. Balabas, G. Vasilakis, L. D. Mosgaard, H. C. Stærkind, J. H. Müller, T. Heimburg, S.-P. Olesen, and E. S. Polzik, "Non-invasive detection

of animal nerve impulses with an atomic magnetometer operating near quantum limited sensitivity," *Scientific Reports*, vol. 6, p. 29638, Jul. 2016. 48, 67

[129] M. Tsang, H. M. Wiseman, and C. M. Caves, "Fundamental quantum limit to waveform estimation," *Phys. Rev. Lett.*, vol. 106, p. 090401, Mar 2011. [Online]. Available: http://link.aps.org/doi/10.1103/PhysRevLett.106.090401 49

[130] A. Holevo, *Probabilistic and Statistical Aspects of Quantum Theory*. North-Holland, Amsterdam, 1982. 50, 52

[131] A. Ajoy, G. A. Álvarez, and D. Suter, "Optimal pulse spacing for dynamical decoupling in the presence of a purely dephasing spin bath," *Phys. Rev. A*, vol. 83, p. 032303, Mar 2011. [Online]. Available: http://link.aps.org/doi/10.1103/PhysRevA.83.032303 51

[132] J. Bylander, S. Gustavsson, F. Yan, F. Yoshihara, K. Harrabi, G. Fitch, D. G. Cory, and W. D. Oliver, "Noise spectroscopy through dynamical decoupling with a superconducting flux qubit," *Nat. Phys.*, vol. 7, pp. 565–570, 2011. [Online]. Available: http://dx.doi.org/10.1038/nphys1994 51, 54

[133] L. Cywinski, R. M. Lutchyn, C. P. Nave, and S. DasSarma, "How to enhance dephasing time in superconducting qubits," *Phys. Rev. B*, vol. 77, no. 17, p. 174509, May 2008. [Online]. Available: http://dx.doi.org/10.1103/PhysRevB.77.174509 51, 62, 74, 95

[134] D. Kielpinski, V. Meyer, M. A. Rowe, C. A. Sackett, W. M. Itano, C. Monroe, and D. J. Wineland, "A decoherence-free quantum memory using trapped ions," *Science*, vol. 291, no. 5506, pp. 1013–1015, 2001. [Online]. Available: http://dx.doi.org/10.1126/science.1057357 51

[135] N. Bar-Gill, L. Pham, C. Belthangady, D. Le Sage, P. Cappellaro, J. Maze, M. Lukin, A. Yacoby, and R. Walsworth, "Suppression of spin-bath dynamics for improved coherence of multi-spin-qubit systems," *Nat. Commun.*, vol. 3, p. 858, 2012. [Online]. Available: http://dx.doi.org/10.1038/ncomms1856 51, 54, 73

[136] Y. Romach, C. Müller, T. Unden, L. J. Rogers, T. Isoda, K. M. Itoh, M. Markham, A. Stacey, J. Meijer, S. Pezzagna, B. Naydenov, L. P. McGuinness, N. Bar-Gill, and F. Jelezko, "Spectroscopy of surface-induced noise using shallow spins in diamond," *Phys.*

Rev. Lett., vol. 114, p. 017601, Jan 2015. [Online]. Available: http://link.aps.org/doi/10.1103/PhysRevLett.114.017601 51, 65

[137] J. R. Petta, A. C. Johnson, J. M. Taylor, E. A. Laird, A. Yacoby, M. D. Lukin, C. M. Marcus, M. P. Hanson, and A. C. Gossard, "Coherent manipulation of coupled electron spins in semiconductor quantum dots," *Science*, vol. 309, no. 5744, pp. 2180–2184, 2005. [Online]. Available: http://dx.doi.org/10.1126/science.1116955 51

[138] G. A. Paz-Silva and L. Viola, "General transfer-function approach to noise filtering in open-loop quantum control," *Phys. Rev. Lett.*, vol. 113, p. 250501, Dec 2014. [Online]. Available: http://link.aps.org/doi/10.1103/PhysRevLett.113.250501 51

[139] S. L. Braunstein and C. M. Caves, "Statistical distance and the geometry of quantum states," *Phys. Rev. Lett.*, vol. 72, no. 22, pp. 3439–3443, 1994. [Online]. Available: http://dx.doi.org/10.1103/PhysRevLett.72.3439 52

[140] H. Cramer, *Mathematical Methods of Statistics*. Princeton University Press, Princeton, 1946. 53

[141] T. Yuge, S. Sasaki, and Y. Hirayama, "Measurement of the noise spectrum using a multiple-pulse sequence," *Phys. Rev. Lett.*, vol. 107, p. 170504, Oct 2011. [Online]. Available: http://link.aps.org/doi/10.1103/PhysRevLett.107.170504 54, 73, 74, 75, 78, 79

[142] G. A. Álvarez and D. Suter, "Measuring the spectrum of colored noise by dynamical decoupling," *Phys. Rev. Lett.*, vol. 107, p. 230501, 2011. [Online]. Available: http://link.aps.org/doi/10.1103/PhysRevLett.107.230501 54, 73, 75, 79

[143] K. C. Young and K. B. Whaley, "Qubits as spectrometers of dephasing noise," *Phys. Rev. A*, vol. 86, p. 012314, 2012. [Online]. Available: http://link.aps.org/doi/10.1103/PhysRevA.86.012314 54, 73, 74

[144] L. Faoro and L. Viola, "Dynamical suppression of 1/f noise processes in qubit systems," *Phys. Rev. Lett.*, vol. 922, p. 117905, 2004. [Online]. Available: http://dx.doi.org/10.1103/PhysRevLett.92.117905 54, 74

[145] I. Almog, Y. Sagi, G. Gordon, G. Bensky, G. Kurizki, and N. Davidson, "Direct measurement of the system-environment coupling as a tool for understanding decoherence and dynamical

decoupling," *Journal of Physics B: Atomic, Molecular and Optical Physics*, vol. 44, no. 15, p. 154006, 2011. [Online]. Available: http://stacks.iop.org/0953-4075/44/i=15/a=154006 54, 74

[146] F. Reinhard, F. Shi, N. Zhao, F. Rempp, B. Naydenov, J. Meijer, L. T. Hall, L. Hollenberg, J. Du, R.-B. Liu, and J. Wrachtrup, "Tuning a spin bath through the quantum-classical transition," *Physical Review Letters*, vol. 108, no. 20, p. 200402, May 2012. [Online]. Available: http://link.aps.org/doi/10.1103/PhysRevLett.108.200402 54, 84, 88

[147] M. Loretz, J. M. Boss, T. Rosskopf, H. J. Mamin, D. Rugar, and C. L. Degen, "Spurious harmonic response of multipulse quantum sensing sequences," *Phys. Rev. X*, vol. 5, p. 021009, Apr 2015. [Online]. Available: http://link.aps.org/doi/10.1103/PhysRevX.5.021009 54, 57

[148] L. Childress, M. V. Gurudev Dutt, J. M. Taylor, A. S. Zibrov, F. Jelezko, J. Wrachtrup, P. R. Hemmer, and M. D. Lukin, "Coherent dynamics of coupled electron and nuclear spin qubits in diamond," *Science*, vol. 314, no. 5797, pp. 281–285, 2006. [Online]. Available: http://dx.doi.org/10.1126/science.1131871 54, 76

[149] T. H. Taminiau, J. J. T. Wagenaar, T. van der Sar, F. Jelezko, V. V. Dobrovitski, and R. Hanson, "Detection and control of individual nuclear spins using a weakly coupled electron spin," *Phys. Rev. Lett.*, vol. 109, no. 13, p. 137602, Sep. 2012. [Online]. Available: http://link.aps.org/doi/10.1103/PhysRevLett.109.137602 54, 58, 81, 82

[150] S. Kolkowitz, A. C. Bleszynski Jayich, Q. P. Unterreithmeier, S. D. Bennett, P. Rabl, J. G. E. Harris, and M. D. Lukin, "Coherent sensing of a mechanical resonator with a single-spin qubit," *Science*, vol. 335, no. 6076, pp. 1603–1606, 2012. [Online]. Available: http://www.sciencemag.org/content/335/6076/1603.abstract 54, 58

[151] N. Zhao, J. Honert, B. Schmid, M. Klas, J. Isoya, M. Markham, D. Twitchen, F. Jelezko, R.-B. Liu, H. Fedder, and J. Wrachtrup, "Sensing single remote nuclear spins." *Nat. Nanotech.*, vol. 7, no. 10, pp. 657–62, Oct. 2012. [Online]. Available: http://dx.doi.org/10.1038/nnano.2012.152 58, 81

[152] F. Shi, Q. Zhang, P. Wang, H. Sun, J. Wang, X. Rong, M. Chen, C. Ju, F. Reinhard, H. Chen, J. Wrachtrup, J. Wang, and J. Du, "Single-protein spin resonance spectroscopy under ambient conditions,"

Science, vol. 347, no. 6226, pp. 1135–1138, 2015. [Online]. Available: http://science.sciencemag.org/content/347/6226/1135 58

[153] A. Ajoy, Y.-X. Liu, K. Saha, L. Marseglia, J.-C. Jaskula, U. Bissbort, and P. Cappellaro, "Quantum interpolation for high-resolution sensing," *Proc. Nat Acad. Sc.*, vol. 114, no. 9, p. 2149–2153, 2017. [Online]. Available: http://www.pnas.org/content/early/2017/02/13/1610835114.abstract 62

[154] W. Ma, F. Shi, K. Xu, P. Wang, X. Xu, X. Rong, C. Ju, C.-K. Duan, N. Zhao, and J. Du, "Resolving remote nuclear spins in a noisy bath by dynamical decoupling design," *Phys. Rev. A*, vol. 92, p. 033418, Sep 2015. [Online]. Available: https://link.aps.org/doi/10.1103/PhysRevA.92.033418 62, 86

[155] G. D. Fuchs, V. V. Dobrovitski, D. M. Toyli, F. J. Heremans, and D. D. Awschalom, "Gigahertz dynamics of a strongly driven single quantum spin," *Science*, vol. 326, no. 5959, pp. 1520–1522, 2009. [Online]. Available: http://www.sciencemag.org/cgi/content/abstract/326/5959/1520 65

[156] B. K. Ofori-Okai, S. Pezzagna, K. Chang, M. Loretz, R. Schirhagl, Y. Tao, B. A. Moores, K. Groot-Berning, J. Meijer, and C. L. Degen, "Spin properties of very shallow nitrogen vacancy defects in diamond," *Phys. Rev. B*, vol. 86, p. 081406, Aug 2012. [Online]. Available: https://link.aps.org/doi/10.1103/PhysRevB.86.081406 65

[157] L. M. Pham, S. J. DeVience, F. Casola, I. Lovchinsky, A. O. Sushkov, E. Bersin, J. Lee, E. Urbach, P. Cappellaro, H. Park, A. Yacoby, M. Lukin, and R. L. Walsworth, "NMR technique for determining the depth of shallow nitrogen-vacancy centers in diamond," *Phys. Rev. B*, vol. 93, p. 045425, Jan 2016. [Online]. Available: http://link.aps.org/doi/10.1103/PhysRevB.93.045425 65

[158] A. M. Schrand, S. A. C. Hens, and O. A. Shenderova, "Nanodiamond particles: Properties and perspectives for bioapplications," *Critical Reviews in Solid State and Materials Sciences*, vol. 34, no. 1-2, pp. 18–74, May 2009. [Online]. Available: http://www.tandfonline.com/doi/abs/10.1080/10408430902831987 67

[159] L. T. Hall, J. H. Cole, C. D. Hill, and L. C. L. Hollenberg, "Sensing of fluctuating nanoscale magnetic fields using nitrogen-vacancy centers in diamond," *Phys. Rev. Lett.*, vol. 103, p. 220802, Nov 2009. [Online].

Available: http://link.aps.org/doi/10.1103/PhysRevLett.103.220802 69

[160] L. T. Hall, C. D. Hill, J. H. Cole, B. Städler, F. Caruso, P. Mulvaney, J. Wrachtrup, and L. C. L. Hollenberg, "Monitoring ion-channel function in real time through quantum decoherence." *Proc. Nat Acad. Sc.*, vol. 107, no. 44, pp. 18 777–18 782, Nov. 2010. [Online]. Available: http://www.pnas.org/content/107/44/18777 69

[161] A. Laraoui, J. S. Hodges, and C. A. Meriles, "Nitrogen-vacancy-assisted magnetometry of paramagnetic centers in an individual diamond nanocrystal," *Nano Lett.*, vol. 12, no. 7, pp. 3477–3482, Jul. 2012. [Online]. Available: https://doi.org/10.1021/nl300964g 72

[162] N. Zhao, J.-L. Hu, S.-W. Ho, J. T. K. Wan, and R. B. Liu, "Atomic-scale magnetometry of distant nuclear spin clusters via nitrogen-vacancy spin in diamond." *Nat. Nanotech.*, vol. 6, no. 4, pp. 242–6, Apr. 2011. [Online]. Available: http://dx.doi.org/10.1038/nnano.2011.22 72, 86

[163] F. Shi, X. Kong, P. Wang, F. Kong, N. Zhao, R.-B. Liu, and J. Du, "Sensing and atomic-scale structure analysis of single nuclear-spin clusters in diamond," *Nat. Phys.*, vol. 10, pp. 21–, Nov. 2013. [Online]. Available: http://dx.doi.org/10.1038/nphys2814 72

[164] T. van der Sar, F. Casola, R. Walsworth, and A. Yacoby, "Nanometre-scale probing of spin waves using single electron spins," *Nat Commun*, vol. 6, p. 8886, Aug. 2015. [Online]. Available: http://dx.doi.org/10.1038/ncomms8886 72

[165] D. Layden and P. Cappellaro, "Spatial noise filtering through error correction for quantum sensing," *npj Quantum Information*, vol. 4, p. 30, July 2018. [Online]. Available: https://www.nature.com/articles/s41534-018-0082-2 73

[166] G. Goldstein, P. Cappellaro, J. R. Maze, J. S. Hodges, L. Jiang, A. S. Sorensen, and M. D. Lukin, "Environment assisted precision measurement," *Phys. Rev. Lett.*, vol. 106, no. 14, p. 140502, 2011. [Online]. Available: http://prl.aps.org/abstract/PRL/v106/i14/e140502 73

[167] M. H. Abobeih, J. Cramer, M. A. Bakker, N. Kalb, M. Markham, D. J. Twitchen, and T. H. Taminiau, "One-second coherence for a single

electron spin coupled to a multi-qubit nuclear-spin environment," *Nature Communications*, vol. 9, no. 2552, 2018. [Online]. Available: http://www.nature.com/articles/s41467-018-04916-z 73

[168] S. Hernández-Gómez, F. Poggiali, P. Cappellaro, and N. Fabbri, "Noise spectroscopy of a quantum-classical environment with a diamond qubit," *Phys. Rev. B*, vol. 98, p. 214307, Dec 2018. [Online]. Available: https://link.aps.org/doi/10.1103/PhysRevB.98.214307 73, 84, 86, 88, 90

[169] S. Kotler, N. Akerman, Y. Glickman, A. Keselman, and R. Ozeri, "Single-ion quantum lock-in amplifier." *Nature*, vol. 473, no. 7345, pp. 61–5, May 2011. [Online]. Available: http://dx.doi.org/10.1038/nature10010 73, 75

[170] F. Yan, S. Gustavsson, J. Bylander, X. Jin, F. Yoshihara, D. G. Cory, Y. Nakamura, T. P. Orlando, and W. D. Oliver, "Rotating-frame relaxation as a noise spectrum analyser of a superconducting qubit undergoing driven evolution," *Nat. Commun.*, vol. 4, p. 2337, 2013. [Online]. Available: http://dx.doi.org/10.1038/ncomms3337 73

[171] A. Abragam, *Principles of Nuclear Magnetism*. Oxford Univ. Press, 1961. 73

[172] A. Lazariev, S. Arroyo-Camejo, G. Rahane, V. K. Kavatamane, and G. Balasubramanian, "Dynamical sensitivity control of a single-spin quantum sensor," *Scientific Reports*, vol. 7, no. 1, p. 6586, 2017. [Online]. Available: https://doi.org/10.1038/s41598-017-05387-w 73

[173] Y. Romach, A. Lazariev, I. Avrahami, F. Kleißler, S. Arroyo-Camejo, and N. Bar-Gill, "Quantum noise spectroscopy of non-monotonous spectra," *ArXiv:1803.07390*, 2018. [Online]. Available: https://arxiv.org/abs/1803.07390 73

[174] G. A. Álvarez and D. Suter, "Localization effects induced by decoherence in superpositions of many-spin quantum states," *Phys. Rev. A*, vol. 84, p. 012320, Jul 2011. [Online]. Available: https://link.aps.org/doi/10.1103/PhysRevA.84.012320 75

[175] D. Crow and R. Joynt, "Classical simulation of quantum dephasing and depolarizing noise," *Phys. Rev. A*, vol. 89, p. 042123, Apr 2014. [Online]. Available: http://link.aps.org/doi/10.1103/PhysRevA.89.042123 75, 83

[176] L. Landau and R. Streater, "On Birkhoff's theorem for doubly stochastic completely positive maps of matrix algebras," *Linear Algebra and its Applications*, vol. 193, no. 0, pp. 107 – 127, 1993. [Online]. Available: http://www.sciencedirect.com/science/article/pii/002437959390274R 75

[177] A. Maudsley, "Modified Carr-Purcell-Meiboom-Gill sequence for NMR fourier imaging applications," *Journal of Magnetic Resonance (1969)*, vol. 69, no. 3, pp. 488–491, 10 1986. 76

[178] P. Szańkowski and L. Cywiński, "Accuracy of dynamical-decoupling-based spectroscopy of Gaussian noise," *Phys. Rev. A*, vol. 97, p. 032101, Mar 2018. [Online]. Available: https://link.aps.org/doi/10.1103/PhysRevA.97.032101 81

[179] S. Kolkowitz, Q. P. Unterreithmeier, S. D. Bennett, and M. D. Lukin, "Sensing distant nuclear spins with a single electron spin," *Phys. Rev. Lett.*, vol. 109, p. 137601, Sep 2012. [Online]. Available: http://link.aps.org/doi/10.1103/PhysRevLett.109.137601 81, 82

[180] W. Yang and R.-B. Liu, "Quantum many-body theory of qubit decoherence in a finite-size spin bath," *Phys. Rev. B*, vol. 78, p. 085315, 2008. [Online]. Available: http://link.aps.org/doi/10.1103/PhysRevB.78.085315 81

[181] A. M. Souza, G. A. Álvarez, and D. Suter, "Robust dynamical decoupling for quantum computing and quantum memory," *Phys. Rev. Lett.*, vol. 106, p. 240501, Jun 2011. [Online]. Available: https://link.aps.org/doi/10.1103/PhysRevLett.106.240501 86

[182] K. Roszak, D. Kwiatkowski, and Łukasz Cywiński, "Experimentally straightforward detection of qubit-environment entanglement generated during qubit dephasing - witnessing non-classical nature of environmental noise," *ArXiv:1810.09217*, 2018. [Online]. Available: https://arxiv.org/abs/1810.09217 91

[183] A. Cooper, E. Magesan, H. Yum, and P. Cappellaro, "Time-resolved magnetic sensing with electronic spins in diamond," *Nat. Commun.*, vol. 5, p. 3141, 2014. [Online]. Available: http://dx.doi.org/10.1038/ncomms4141 91

[184] H. M. Wiseman and G. J. Milburn, "Quantum theory of optical feedback via homodyne detection," *Phys. Rev. Lett.*,

vol. 70, pp. 548–551, Feb 1993. [Online]. Available: http://link.aps.org/doi/10.1103/PhysRevLett.70.548 91

[185] S. Lloyd, "Coherent quantum feedback," *Phys. Rev. A*, vol. 62, no. 2, p. 022108, 2000. [Online]. Available: http://dx.doi.org/10.1103/PhysRevA.62.022108 91

Ringraziamenti

Giunti a questo punto, la fine del percorso da studente, anche se non si finisce mai di studiare, è arrivato il momento di spendere due parole per ringraziare brevemente le persone che maggiormente mi hanno aiutato.

Prima di tutto, ringrazio chi mi ha dato l'opportunità di entrare nel corso di dottorato, consigliandomi il passaggio al campo di ricerca legato ai centri NV in diamante, in particolare i Prof. Inguscio e Fallani. Ringrazio quindi la Prof.ssa Paola Cappellaro, che è riuscita a starmi accanto anche se da lontano, con un oceano a separarci, con la sua notevole conoscenza della materia ed esperienza. Un grazie veramente sentito va alla mia mentore Dott.ssa Nicole Fabbri, che più di tutti mi ha supportato in questo cammino di dottorato: con la sua competenza profonda e l'esempio quotidiano ha saputo guidarmi in quelli che sono stati i miei primi passi nel mondo della ricerca. Ringraziando poi i miei compagni di studi, non posso che iniziare da Santiago, con cui ho condiviso il percorso nel mio ultimo anno di dottorato; un grazie va quindi a tutti i miei professori e colleghi che, anche lavorando in altri ambiti, sono stati fonte inesauribile di profonde e utili discussioni. In questo senso, nell'ambiente del Polo Scientifico di Sesto Fiorentino ho trovato un terreno fertile che non ha potuto che aiutare la mia crescita. Alcuni poi, più che colleghi, sono veri e propri amici, che ringrazio per la condivisione di un percorso attraverso il tempo passato insieme nella quotidianità o nel divertimento del tempo libero.

Inoltre, sono fortemente grato a tutti coloro che anche fuori dall'ambito lavorativo hanno contribuito alla mia crescita e alla mia serenità, sostenendomi in tutto il percorso, non privo di ostacoli, anche quello precedente al dottorato stesso. Perciò ringrazio tantissimo i miei numerosi amici, da quelli più vecchi e storici ai più recenti; se mi vedo quasi costretto a non mettere i nomi è solo perché posso ritenermi molto fortunato e l'elenco risulterebbe effettivamente lungo, con l'inevitabile conseguenza di una qualche dimenticanza.

Per ultima, ma non per importanza, ringrazio la mia famiglia, a partire da quella estesa, vasta e un po' pazza, fatta di nonni (anche quelli che non

ci sono più), zii e cugini a cui sono legato moltissimo. Un grazie enorme, davvero di cuore, va ai miei genitori, ai miei fratelli e alla mia ragazza: il loro supporto, la comprensione (e, diciamolo, anche la sopportazione) sono stati fondamentali per superare i momenti più difficili, così come per godersi appieno quelli migliori.

Come ultima cosa, mi preme sottolineare che ognuna delle persone che si trovano in questa mia povera pagina è stata ed è, per me, come la tessera, chi grande chi piccola, di un mosaico veramente ricco raffigurante il mio cammino. Se per caso state leggendo, sappiate che non posso che augurami di proseguire il mio percorso con voi. Grazie.